Multi-Physics Modeling of Lithium-Ion Battery Electrodes

by

Hamed Fathiannasab

A thesis
presented to the University of Waterloo
in fulfillment of the
thesis requirement for the degree of
Doctor of Philosophy
in
Chemical Engineering

Waterloo, Ontario, Canada, 2020

Examining Committee Membership

The following served on the Examining Committee for this thesis. The decision of the Examining Committee is by majority vote.

External Examiner:	Dr. Paul Shearing Professor, Department of Chemical Engineering, University College London
Supervisor:	Dr. Zhongwei Chen Professor, Department of Chemical Engineering, University of Waterloo
Internal Member:	Dr. Eric Croiset Professor, Department of Chemical Engineering, University of Waterloo
Internal Member:	Dr. Jeffrey Gostick Associate Professor, Department of Chemical Engineering, University of Waterloo
Internal-external Member:	Dr. Roydon Fraser, Professor, Department of Mechanical and Mechatronics Engineering, University of Waterloo

AUTHOR'S DECLARATION

This thesis consists of material all of which I authored or co-authored: see Statement of Contributions included in the thesis. This is a true copy of the thesis, including any required final revisions, as accepted by my examiners.

I understand that my thesis may be made electronically available to the public.

Statement of Contributions

The body of this thesis is based on a combination of published and under revision studies. Various sections are adapted from the following list of publications:

Hamed Fathiannasab, Likun Zhu, and Zhongwei Chen, "Chemo-Mechanical Modeling of Stress Evolution in All-Solid-State Lithium-Ion Batteries Using Synchrotron Transmission X-ray Microscopy Tomography", Journal of Power Sources, 2020.

> I have developed the modeling framework. Dr. Zhu performed the X-ray computed tomography imaging. I reconstruct the morphologies and prepared all the results and wrote the final manuscript. Dr. Zhu and Dr. Chen reviewed the manuscript.

Hamed Fathiannasab, Ali Ghorbani Kashkooli, Kun Feng, and Zhongwei Chen, "Universal Multiscale Modeling of Composite Gr/Si Electrode for Lithium-ion Batteries".

> I have developed the modeling framework. Dr. Feng and I performed experimental testing of batteries. Dr. Ghorbani assist with the simulation. I prepared all the results and wrote the final manuscript. Dr. Chen reviewed the manuscript.

Hamed Fathiannasab, Ali Ghorbani Kashkooli, Tianyi Li, Likun Zhu, and Zhongwei Chen, "Three-Dimensional Modeling of All-Solid-State Lithium-Ion Batteries Using Synchrotron Transmission X-ray Microscopy Tomography". Journal of the Electrochemical Society, 167, 100558, DOI: 10.1149/1945-7111/ab9380

> I have developed the modeling framework. Dr. Zhu and Mr. Li performed the X-ray computed tomography imaging. I reconstruct the morphologies and prepared all the results and wrote the final manuscript. Dr. Ghorbani assist with the simulation. Dr. Zhu and Dr. Chen reviewed the manuscript.

Hamed Fathiannasab, Zhiyu Mao, Tyler Or, Qianyi Ma, and Zhongwei Chen, "Artificial Intelligence Applications in Smart Battery Management for Electric Vehicles"

> I have conducted the literature review and wrote the final manuscript. Dr. Mao, Mr. Or, and Mr. Ma assist with the paper structure. Dr. Chen reviewed the manuscript.

Abstract

Lithium-ion batteries (LIBs) dominated the market due to their relatively high energy/power density, and long cycle life. However, a multitude of factors need to be addressed which have hindered further development of LIBs such as limited current density and safety issues. One of the effective methodologies to enhance the LIBs energy/power density is to employ alloy-based anode materials with higher theoretical capacity compared with graphite which is the common anode active material in LIBs. For instance, silicon has approximately ten times more capacity than graphite; however, intrinsic issues of silicon, such as high volume change during cycling and an unstable solid-electrolyte interphase (SEI) layer, lead to poor cyclability and cell degradation. One of the common strategies to alleviate the aforementioned silicon challenges is to use a composite graphite/silicon electrode. On one hand, experimental design and optimization of composite electrodes can be time-consuming, and in some cases, such as measuring stress evolution at the particle level of composite electrodes, unfeasible. On the other hand, incorporating multi-physics simulation can shed light on the chemo-mechanical behavior of composite electrodes and provide invaluable insights regarding lithiation-induced stress evolution and ultimately pave the path toward design and optimization of composite electrodes.

Moreover, one of the main drawbacks of LIBs is safety concerns because of flammable liquid electrolytes. All-solid-state lithium-ion batteries (ASSBs) are a safer alternative to the conventional liquid electrolyte LIBs. ASSBs are based on utilizing a solid electrolyte to eliminate safety concerns such as thermal runaway and leakage of flammable liquid electrolytes. Additionally, the solid electrolyte can facilitate using high-capacity anode active materials, such as silicon and lithium plate, by inhibiting lithium dendrite formation and suppressing silicon volume expansion during the battery operation. Despite the clear advantages of ASSBs, critical challenges hinder their widespread application, including poor solid electrolyte/solid active material interfacial contact, low ionic conductivity of solid electrolytes, and poor electrochemical stability.

Solid electrolyte/active material (SE/AM) interface adversly affects the performance of the ASSBs. Since the two solid phases are not perfectly in contact with each other, void spaces block the ion pathways at the SE/AM interface. Moreover, due to the solid/solid nature of this interface, lithiation-induced stress during the battery operation can cause stress peak points at the interface which leads to crack propagation within the solid electrolyte, loss of contact, and subsequently capacity fade and mechanical degradation. Therefore, ASSB microstructural investigation can enlighten the multi-physics behavior of ASSBs.

Using electrode imaging techniques, such as focused ion beam-scanning electron microscopy (FIB-SEM) and X-ray computed tomography (XCT), can accurately capture the microstructures of electrodes. In particular, the XCT method is non-destructive and can provide a quantitative analysis of the electrode morphology such as particle and pore size distribution, porosity, and surface area. Moreover, the XCT reconstructed morphology can be adopted as the multi-physics simulation domain. The modeling framework in this study is comprised of an electrochemical model including conservation of mass/charge and a solid mechanics model based on the thermal-mass analogy to obtain lithiation-induced stress within the electrode microstructure. The presented work aims to adopt the 3D reconstructed morphology of the electrode to study the physical, mechanical, and electrochemical properties of LIBs.

In the first study, a multiscale framework was developed and validated for a composite graphite/silicon electrode. The model is an electrochemical-solid mechanics integration used to estimate the composite electrode performance, silicon deformation, and stress evolution. The effects of silicon percentage and current on cell performance, hydrostatic stress, lithium concentration, and deformation are investigated. Considering the effect of stress on the lithium chemical potential within silicon particles in microscale modeling can shed light on the formation of a lithium concentration gradient due to the stress, and thus can enhance the composite electrode model accuracy. Moreover,

physical constraints can cause the co-existence of compressive and tensile stress, while lithiation-induced stress inside the silicon particles retard the lithiation process. In fact, lithiation retardation would form a core-shell structure that comprises a lithiated shell and an unlithiated core with an incompatible strain at the interface, causing higher von Mises stress. Physical constraints highly affect the hydrostatic stress formation in silicon particles and may impact the cell life cycle due to the anisotropic swelling of particles. The developed methodology is compatible with different composite electrodes, considers the effect of active material expansion/contraction, and can pave the path for developing physics-based battery state estimation models for composite Si-based electrodes.

In the second study, a synchrotron transmission X-ray microscopy tomography system has been utilized to reconstruct the 3D morphology of ASSB electrodes. The electrode was fabricated with a mixture of $Li(Ni_{1/3}Mn_{1/3}Co_{1/3})O_2$, $Li_{1.3}Ti_{1.7}Al_{0.3}(PO_4)_3$, and super-P. For the first time, a 3D numerical multi-physics model was developed to simulate the galvanostatic discharge performance of an ASSB, elucidating the spatial distribution of physical and electrochemical properties inside the electrode microstructure. The 3D model shows a wide distribution of electrochemical properties in the solid electrolyte and the active material which might have a negative effect on ASSB performance. The results show that at high current rates, the void space hinders the ions' movement and causes local inhomogeneity in the lithium-ion distribution. The simulation results for electrodes fabricated under two pressing pressures reveal that higher pressure decreases the void spaces, leading to a more uniform distribution of lithium-ions in the SE due to more facile lithium-ion transport. The approach in this study is a key step moving forward in the design of 3D ASSBs and sheds light on the physical and electrochemical property distribution in the solid electrolyte, active material, and their interface.

In the last study, a chemo-mechanical model was developed for the ASSBs' composite electrode using the reconstructed morphologies in the second study. This study aimed to shed light on the effects of the electrode microstructure and solid electrolyte/active material interface on the stress evolution

during the battery operation. The simulation results show that active material particles encounter compressive hydrostatic stress up to 4 GPa at the solid electrolyte/active material interface during lithiation while solid electrolyte limits their expansion. While, void spaces can partially accommodate active material volume expansion, and areas near void spaces have tensile stress within the range of 0-1 Gpa. Therefore, the electrode with the higher external pressing pressure experiences a relatively higher hydrostatic stress due to a higher solid electrolyte/active material interface and less void space volume fraction. In other words, although increasing the external pressing pressure may alleviate contact resistances and improve the ion pathways, it can intensify lithiation induced stress within the electrode microstructure and causes fracture formation, contact loss, and mechanical degradation. For instance, at the end of lithiation, the von Mises stress in the active material particles is approximately zero while at the surface, AM confronts up to 4.9 GPa stress and the average von Mises stress within the microstructure with higher pressing pressure is 2.4 GPa compared to 1.5 GPa. Thus, microstructural investigation of ASSBs is critical to find an optimal design to maximize the ion pathways and limit the stress evolution within an acceptable range.

Integrating the developed multi-physics models with data-driven methods can decrease the computational cost and leads to a holistic modeling framework for LIBs. Incorporating the self-learning feature of data-driven methods can mimic the experimental performance of batteries and predict the behavior of batteries with high fidelity.

Acknowledgments

Foremostly, I would like to express my sincere gratitude to my supervisor, Professor Zhongwei Chen. Not only this work could not happen without his continuous encouragement and support, but his guidance open doors to learn how to tackle a challenge.

I would like to thank my examining committee: Prof. Paul Shearing (University College London), Prof. Roydon Fraser, Prof. Eric Croiset, and Prof. Jeffrey Gostick for their time and effort in reading my Ph.D. thesis and for their valuable comments.

I thank my fellow lab mates and colleagues, especially Dr. Ali Ghorbani, for their great help and insightful comments.

The Natural Sciences and Engineering Research Council of Canada (NSERC), University of Waterloo, and the Department of Chemical Engineering are all acknowledged for their financial support of this project. CMC Microsystems is also acknowledged for the provision of products and services that facilitated this research, including COMSOL Multiphysics and providing computational facilities.

I'd also like to acknowledge Advanced Photon Source (APS) in Argonne National Laboratory (ANL) for using the Transmission X-ray Microscope (TXM) facility.

In the end, my special thanks go to my parents, kind sister, and lovely wife who always have supported me in the ups and downs of this path.

Dedication

To my wife, Maryam, for her continuous love, support, and encouragement!

And,

To my parents, Nazi and Mahmoud, whose support and constant love have sustained me throughout my life!

Table of Contents

List of Figures

List of Tables

Chapter 1
Introduction

1.1 Research Background and Motivation

The shortage of conventional energy resources such as fossil fuel and raising environmental concerns has led to the rapid utilization and development of renewable energy resources. Due to the intermittent nature of renewable energies, storing energy during pick hours and give it back on demand is critical. Among all types of energy storage methods, Electrochemical energy storage (EES) technology has proven to be a reliable and efficient way to incorporate intermittent energy resources into existing electrical grid infrastructures. Moreover, the electrification of the automobile industry is one of the main paths toward global decarbonization [1] and a promising solution to address oil supply shortages and environmental pollution. In 2018, the global electric vehicle (EV) fleet reached 5.1 million, which is about 2 million higher than the previous year [2]. However, the EV industry still faces critical challenges such as limited driving range, long charging time, low battery lifetime, and safety considerations, which restrict widespread adoption of EVs.

Among all types of batteries, lithium-ion batteries (LIBs) dominated the market [3]; however, a multitude of factors need to be addressed which hindered further development of LIBs such as limited current density and safety issues [4]. One way to address the limited energy density issue is to use alloy-based anode active materials such as silicon (Si) or tin (Sn), which have up to ten times the specific capacity compared to the conventional graphite (Gr) anode. However, intrinsic issues of alloy anodes, such as the high volume change during cycling and unstable solid-electrolyte interphase (SEI) layer, lead to poor cyclability and cell degradation. Many strategies have been deployed to mitigate the volume change of the electrode, such as forming Si nanostructures to buffer volume changes [5-7], employing Si/Gr composite electrode[8, 9], and the use of electrolyte additives to stabilize the SEI layer [10, 11]. Among these strategies, employing Si/Gr composite anode has garnered significant attention

due to the ease of fabrication and scalability compared to pure Si electrodes, improved stability, and the relatively higher capacity.

It is worth noting that measuring stress evolution at the particle level of composite electrodes is unfeasible, although there are some efforts to shed light on *in-situ* stress formation throughout lithiation/delithiation of Si thin film [12] or employing micro-Raman spectroscopy to measure the lithiation-induced stress in Si particles [13]. On the other hand, employing mechanical-electrochemical models can provide invaluable insights regarding stress evolution in the electrode microstructure and elucidate the effects of operating conditions on the composite electrode performance. Mathematical models have been effective in electrode design and optimization [14]. Specifically, detailed mathematical modeling can accelerate the process of optimizing composite electrodes and addressing the bottleneck challenges.

In addition to employing composite electrodes to overcome the LIBs limitation, All-solid-state lithium-ion batteries (ASSBs), which are based on solid electrolytes (SEs), are a safer alternative to the conventional liquid electrolyte LIBs. SEs can eliminate safety concerns such as thermal runaway and electrolyte leakage of flammable liquid electrolytes [15, 16]. Moreover, SEs can facilitate the future application of high capacity anode materials such as metallic lithium [17] and Si [18] by inhibiting the formation of needle-like microstructures called lithium dendrites on the surface of the lithium anode upon cycling [19] and limiting the large expansion of the Si anode during lithiation [20], thus improving their cycle lives. However, despite the clear advantages of ASSBs, critical challenges hinder their widespread application, including poor SE/solid active material (AM) interfacial contact, the low ionic conductivity of SEs, and poor electrochemical stability [15]. In terms of the SE/AM interface, it is difficult to develop a robust interface due to the limited understanding of the microstructure and reaction interface in ASSBs [21]. Since the two solid phases are not perfectly in contact with each other,

void spaces block the ion pathways at the SE/AM interface, thus negatively affecting the ASSB performance [22].

One way to investigate the physical and electrochemical behavior of batteries is to use the 3D reconstructed geometry of the ASSB electrode instead of simplified 1D or 2D geometries. In recent years, various techniques such as focused ion beam-scanning electron microscopy (FIB-SEM) [23, 24], magnetic resonance imaging (MRI) [25], and computed tomography (CT) [26-29] have become available to capture the real microstructures of LIB electrodes. Among them, the non-destructive CT imaging technique is extensively used to characterize the physical and morphological properties of the electrode including directional tortuosity, porosity, particle size distribution, and specific surface area [28, 30-32]. The reconstructed 3D morphology can shed light on physical properties and can be used as the computational geometry for multi-physics simulations. As mentioned ASSB is a promising alternative for traditional LIBs while their morphology is rarely investigated. Morphological analysis of ASSBs can provide invaluable insights regarding the microstructural design of ASSBs by providing a clear understanding of the roles of phases in a composite electrode. It is precisely these considerations that motivate the work reported herein.

1.2 Research Objective

The objective of this Ph.D. research was to develop multi-physics mathematical models to simulate the physical, mechanical, and electrochemical behavior of LIBs. The developed models shed light on mass and charge transport, lithiation induced volume change, mechanical interaction, and morphological properties during battery operation. This Ph.D. study is comprised of three principal stages: 1) Multi-scale multi-physics modeling of lithium-ion battery composite Gr/Si electrode. This framework consists of an electrochemical sub-model which implemented at a microscale level to simulate lithium diffusion within Si particles and at macroscale to obtain the discharge performance. Moreover, a solid

mechanics sub-model was incorporated at the microscale level to obtain the lithiation induced volume change of Si. The ultimate goal of this project was to develop a universal modeling framework to enlighten the behavior of composite alloy-based electrodes with considering volume changes. 2) Three-dimensional modeling of all-solid-state lithium-ion batteries using synchrotron transmission x-ray microscopy tomography. 3) Chemo-mechanical modeling of stress evolution in all-solid-state lithium-ion batteries using synchrotron transmission x-ray microscopy tomography. In stage two, the electrodes 3D microstructure was reconstructed based on TXM images. The electrochemical and physical analysis were conducted on representative volume element (RVE) to obtain the electrochemical and physical properties distribution within the microstructure at various currents and external pressing pressures to investigate the effects of morphological parameters on the electrochemical behavior of ASSBs. In the third stage, the developed electrochemical model in stage two was coupled with a solid mechanics model to simulate the chemo-mechanical behavior of ASSBs. Special attention was paid to stress evolution at the solid electrolyte/active material interface.

1.3 Research Approach

The overall structure of this thesis is shown in Figure 1-1.

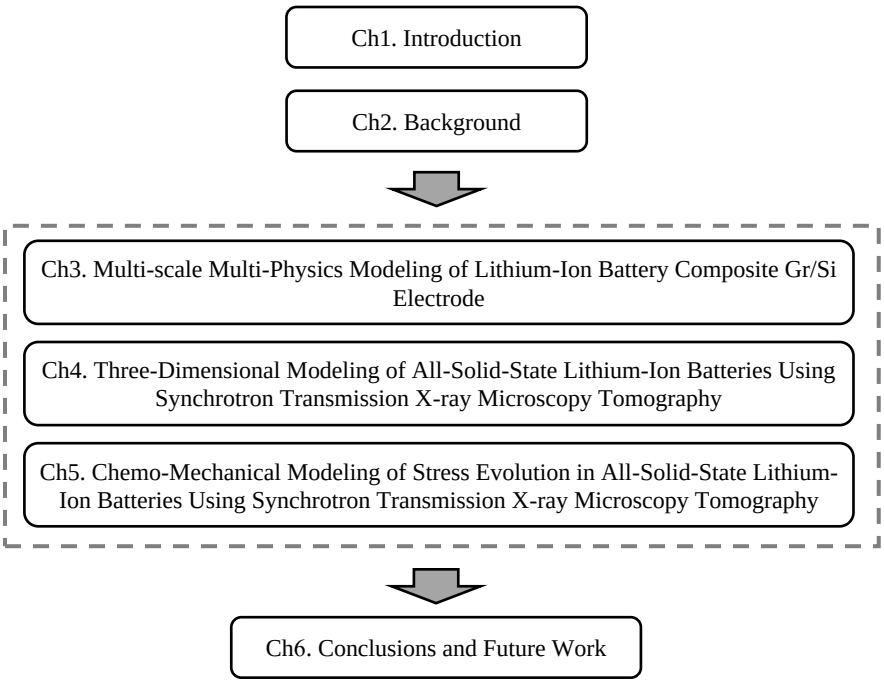

Figure 1-1 Thesis Layout

This thesis is comprised of 6 chapters wherein Chapter 1 represents the motivation and objectives of the overall studies along with the thesis layout. Chapter 2 reviews the background information including LIBs and ASSBs working principals and modeling methodologies. Moreover, the advantages of electrodes CT imaging techniques are elaborated.

In Chapter 3, a multi-scale multi-physics model is introduced to investigate the Gr/Si composite electrode performance considering the Si volume change during the battery operation. In the developed framework, the electrochemical sub-model and solid-mechanics sub-model are coupled to incorporate the effect of lithiation induced stress on the volume change in Si particles and update the lithium

concentration in Si particles based on the new volume at each time step. The lithium transport equation in Si particles and solid mechanics equations are implemented at the microscale level passing the updated lithium concentration to macroscale to simulate the composite electrode performance.

Chapter 4 introduces a three-dimensional model for ASSBs electrodes to investigate the effect of external pressing pressure on the morphological and electrochemical behavior of the composite electrode consists of the solid electrolyte, active material, and void space. To enhance the fidelity of the developed model, the 3D reconstructed microstructure of the electrodes are utilized as the geometry of the model. The SE's resistance to ion transport was quantified by estimating the SE tortuosity using a heat transport analogy. The simulation showed that higher pressing pressure causes 26.8% less void space in the electrode and consequently 11.1% less tortuosity and 36.9% higher volume-specific surface area. The developed model elucidates the spatial distribution of physical and electrochemical properties inside the electrode microstructure. The 3D model shows a wide range of electrochemical properties distribution in the solid electrolyte (SE) and the active material (AM) which might have a negative effect on ASSB performance. The results show that at high current rates, the void space hinders the ions' movement and causes local inhomogeneity in the lithium-ion distribution.

In Chapter 5, a chemo-mechanical model is presented to shed light on the effects of lithiation induced stress on the SE/AM interface. The developed model has an electrochemical sub-model including diffusion and migration in the SE, diffusion in the AM, and charge transfer kinetics at the SE/AM interface computed on a 3D reconstructed morphology. Moreover, the solid mechanics sub-model determines the diffusion induced stress/strain employing a thermal-mass diffusion analogy. The presented model highlights the stress evolution at the SE/AM interface and investigates the effect of void spaces at the interface and role of external pressing pressure. It is worth noting that the mechanical stability of the electrode highly relies on the microstructure design. The results illustrate that although increasing the external pressing pressure can alleviate the SE/AM contact resistances and enhance the

ion transport, it may exacerbate the mechanical stability of the electrode. The main reason for this adverse effect is that lithium diffusion induced volume change in AM particles can lead to a contact loss and crack formation due to the excessive stress evolution at the interface. Moreover,

Chapter 6 summarizes the main contributions of this Ph.D. dissertation and provides recommendations for future work.

Chapter 2
Background

2.1 Lithium-Ion Battery

Lithium-ion battery (LIB) consists of a positive electrode and a negative electrode which divided by a separator that prevents electron pass while allows the ions to go through. During charge, at first, lithium de-intercalates from the positive electrode then diffuses in the electrolyte and intercalates into the active material in the negative electrode. During discharge, the aforementioned steps happen in reverse (Figure 2-1). The positive and negative electrode have various material and chemistry with different performance, specification and consideration depend on the battery application.

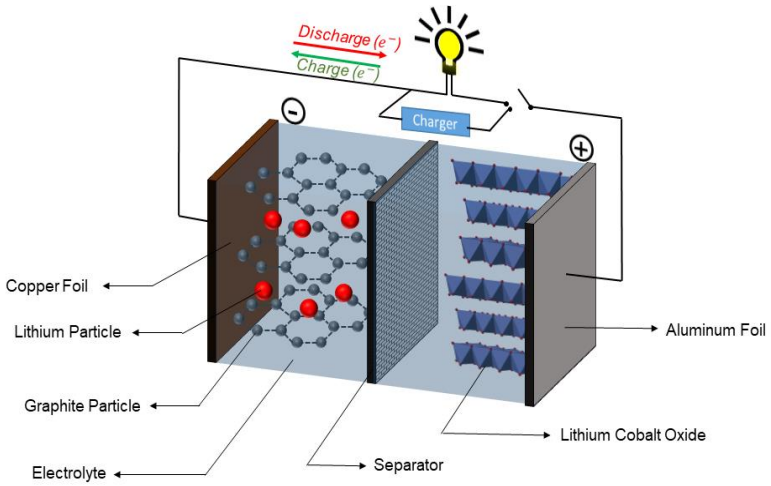

Figure 2-1 Schematic of the lithium-ion battery with the graphite anode and $LiCoO_2$ cathode.

In the negative electrode (Anode), graphite (Gr) is the most common material due to its low cost and good cycling stability. The reaction in the anode side with Gr is:

$$LiC_6 \rightleftharpoons Li_{(1-x)}C_6 + xLi^+ + xe^-, \quad (2\text{-}1)$$

and for the cathode side, there are quite a few materials that widely utilized in LIBs such as lithium manganese oxide (LiMn2O4) or LMO, Lithium cobalt oxide (LiCoO2) or LCO, lithium iron phosphate (LiFePO4) or LFP, and Lithium nickel manganese cobalt oxide (LiNiMnCo2) or NMC are the most common cathode active material. The cathode side reaction is (M stands for metal):

$$\boldsymbol{xLi^{+} + xe^{-} + MO_{y} \rightleftharpoons Li_{x}MO_{y}}. \quad (2\text{-}2)$$

Electrodes in LIBs generally have active material, a binder, and a conductive additive such as carbon black. A slurry is formed by mixing the active material, binder, and conductive additive and cast onto a metal foil. The casting steps, type, and weight percentage of materials highly depend on the application. Carbon-based structures are the most common negative electrode active materials. The first commercial LIBs utilized petroleum coke as the negative active material, whereas most commercialized LIBs employing Gr. Gr electrode advantageous are abundance, high electrical conductivity, low cost, and relatively high energy density and capacity. In the Gr structure, atoms are arranged in hexagonal arrays which form planar sheets and the intercalated lithium is located between Gr layers. The lithium insertion potential leads to a reduction of electrolyte molecules and the formation of a solid electrolyte interface (SEI) during the first cycle [33]. Although SEI layer formation and stable SEI layer are critical for electrodes, it causes the irreversible capacity loss during SEI layer formation. A stable SEI layer prevents the electrolyte from further degradation while the composition of the SEI layer completely depends on the properties of active material, electrolyte composition, and cycling parameters. The thickness of the SEI layer varies from few Å to hundreds of Å which contain organic (reduction of electrolyte solvent like Li_2CO_3) and inorganic compounds (reduction of salt anions like LiF, $LiCl$, and Li_2O) [33].

$Li_4Ti_5O_{12}$ with a theoretical capacity of 175 mAh/g is an alternative for negative electrode active material. LTO electrode has relatively low capacity and high lithium insertion potential which leads to

a low cell voltage and low energy density cell. Whereas, the insertion potential is above the reduction potential of the most common organic electrolytes which prevents ant SEI layer formation during cycling. Furthermore, there is no lithium plating even at high current rates and low temperatures, which makes LTO an ideal material for high power applications [33]. Lithium metal is another candidate for employing as an anode active material due to its valuable advantageous such as high theoretical capacity (3860 mAh/g) and low electrochemical potential (-3.05 V). However, remarkable lithium dendritic formation at the surface of the lithium plate during cycling and considerable volume change hinders the large employment of Lithium plates. In fact, volume change during lithiation/delithiation is a common challenge in alloy-type anode materials as well. For instance, despite the high theoretical capacity of Si (4200 mAh/g) it suffers poor cycling stability due to large volume expansion up to three times at the end of lithiation. One way to address this challenge is to use solid electrolytes instead of liquid electrolytes.

2.2 All-Solid-State Battery

All-solid-state battery (ASSB) is a promising alternative for LIBs due to its remarkable advantages. Traditional LIBs mostly have organic liquid electrolytes that are highly flammable and have low thermal stability. However, inorganic SEs have higher thermal, mechanical, and electrochemical stability [34]. Working principals of ASSBs are the same as LIBs while lithium-ions de-intercalate form cathode and transport through SE to anode during charging and electrons move through an external circuit. Among various type of SEs, such as lisicons [35], perovskites [36, 37], nasicons [38, 39], and garnets [40, 41], the nasicons structure, like $Li_{1.3}Al_{0.3}Ti_{1.7}(PO_4)_3$ (LATP), can be an appealing alternative for today's commercial liquid electrolytes due to their excellent stability against air and water and high ionic conductivity [42].

SE/AM interfacial contact tremendously impacts the ASSBs performance, since SE unlike the liquid electrolyte is not able to form an ideal contact with AM and physical mismatch of these two solid phases creates void spaces at the interface. In ASSBs, the composite cathode generally fabricated with mixing the SE, AM, and a conductive agent. The composite microstructure and morphological properties depend on the mixing conditions such as external pressing pressure, temperature, etc. [43] while poor interfacial contact limits the lithium-ions transport pathways. Moreover, AM particle volume changes during lithiation/delithiation can lead to local stress build up in the microstructure, fracture propagation, and capacity fading [44]. Therefore, microstructure design is highly critical in ASSBs compared to liquid electrolyte cells while liquid electrolyte penetrates the porous electrode and the interfacial contact is not a remarkable issue. Most of the common cathode AM expand during lithiation; although this volume change is negligible compared to Anode AM, it is critical in ASSBs due to the solid/solid nature of the SE/AM interface. In other words, the liquid electrolyte can accommodate the slight volume expansion of cathode AM while in SE even a minor volume changes could cause particle fracture and eventually pulverization [45]. Therefore, further investigation of ASSBs interfacial contact is crucial since continuous expansion/contraction over the cycling of a cell can exacerbate the interfacial resistance and stress evolution.

2.2.1 Solid Electrolyte

The functionality of solid electrolytes is the same as liquid electrolytes and separators while allows lithium-ions to crossover between anode and cathode and block electron transport [34]. Generally, electrolytes should have high ionic conductivity, high ionic transference number, low electronic conductivity, and wide electrochemical stability window [46]. Among all types of solid electrolytes, LISICON, and LiPON-type of solid electrolytes have low ionic conductivity, sulfide, anti-perovskite, and argyrodite-type are unstable in the ambient atmosphere, while garnet, perovskite, and NASICON-type can be a promising alternative for liquid electrolytes [34]. However, employing solid electrolytes

still has a long way to go since it suffers from low wettability compared to liquid electrolyte and high interfacial resistance.

2.3 Lithium-Ion Battery Physics-Based Models

Numerical simulation is an effective tool to shed light on the electrochemical and physical behavior of LIBs. Numerical simulation generally categorized into physics-based modeling and data-driven modeling. Physics-based modeling comprises of a wide range of electrochemical, mechanical, electrical models with different level of complexity, fidelity, and computational cost aimed to simulate complex non-linear behavior of LIBs. Physics-based models are based on solving governing partial differential equations while data-driven methods are based on implementing self-learning algorithms on large data-sets to predict the desired properties. The application of data driven methods in batteries is presented in 0.

2.3.1 Single-Particle Model

Generally, in a single particle model, electrodes substitute with a single particle without considering the porous structure of the electrodes. In other words, the lithium diffusion in particles simulated based on Fick's mass transport. Then, the Butler-Volmer equation employed to calculate the applied flux on the spherical surface. The lithium concentration within the particle obtained by:

$$\frac{\partial c_1}{\partial t} = \frac{1}{r^2}\frac{\partial}{\partial r}\left(r^2 D_1 \frac{\partial c_1}{\partial r}\right) \quad \textbf{BCs: } \left.\frac{\partial c_1}{\partial r}\right|_{r=0} = 0 \quad \textbf{and} \quad \left.\frac{\partial c_1}{\partial r}\right|_{r=R_p} = -j_n D_1 \tag{2-3}$$

Where c_1 is lithium-ion concentration inside the active material particles, R_p is particle radius, D_1 is the diffusivity of the active material, j_n is pore-wall flux. By employing Butler-Volmer equation at the particle interface:

$$j_n = \frac{I}{F} = \frac{i_0}{F}\left(exp\left(\frac{\alpha_a F}{RT}(\phi_1 - U)\right) - exp\left(-\frac{\alpha_c F}{RT}(\phi_1 - U)\right)\right), \tag{2-4}$$

$$i_0 = F k_0 (c_{2s})^{\alpha} (C_{max} - C_{1s})^{\alpha} {C_{1s}}^{\alpha}, \tag{2-5}$$

where i_0, , k_0, F, R, and T are exchange current density, the reaction rate constant, Faraday constant, the universal gas constant, and Temperature, respectively. C_{1s}, C_{2s}, C_{max}, ϕ_1, U are lithium-ion concentration at the interface of active material and electrolyte, the maximum concentration of lithium inside the solid matrix, solid-phase potential, and open circuit potential, respectively. Although the single particle model is not capable to accurately predict the performance of the battery due to neglecting the effect of electrolyte on the voltage and the lithium concentration inside the particle [47, 48], it can provide a rough estimation for on-line application with a low computational cost.

2.3.2 Homogenous Pseudo-Two-Dimensional Model

Pseudo-two-dimensional (P2D) model is a relatively accurate and detailed model compared to a single particle model. P2D models can simulate the lithium concentration in solid phases and electrolyte. P2D models are emanated from porous electrode theory which was developed by Newman in 1975 [49]. Twenty years later, Fuller and Doyle in separate researches implement the porous theory on a battery cell with a positive electrode, negative electrode, electrolyte, and separator [50, 51]. These researches are the base of many developed models in recent years [52-54].

The P2D models consider two different directions, x-direction represents the cell thickness and r direction is the particle radius. Through cell thickness, the P2D model has several BCs to satisfy continuities and conservations of fluxes. The electrode-current collector interfaces have insulation conditions for all parameters except the solid phase potential. For simulating liquid phase in the cell, the lithium concentration in the liquid phase, and the charge balance in the electrolyte can be obtained by:

$$\boldsymbol{\varepsilon}\frac{\partial \boldsymbol{c_2}}{\partial \boldsymbol{t}} = \frac{\partial}{\partial \boldsymbol{x}}\left(\boldsymbol{D_{eff}}\frac{\partial \boldsymbol{c_2}}{\partial \boldsymbol{x}}\right) + \boldsymbol{a j_n}\left(\mathbf{1} - \boldsymbol{t_+^0}\right), \quad (2\text{-}6)$$

$$\frac{\partial \boldsymbol{\phi_2}}{\partial \boldsymbol{x}} = -\frac{\boldsymbol{i_2}}{\boldsymbol{k_{eff}}} + \frac{\boldsymbol{RT}}{\boldsymbol{F}}(\mathbf{1} - \boldsymbol{t_+})\left(\mathbf{1} + \frac{\partial \boldsymbol{ln f_2}}{\partial \boldsymbol{ln c_2}}\right)\frac{\partial \boldsymbol{ln c_2}}{\partial \boldsymbol{x}}, \quad (2\text{-}7)$$

where ε is the electrode porosity, c_2 is the concentration of lithium in liquid phase, D_{eff} is effective diffusivity, t_+^0 is the transference number of the lithium-ion in the solution, and a is the specific surface area. Additionally, i_2 is current density in the liquid phase, f_2 is electrolyte molar activity coefficient, and k_{eff} is effective conductivity. The lithium concentration and charge balance in solid-phase are calculated by:

$$\boldsymbol{I - i_2 = -\sigma_{eff}\frac{\partial \phi_1}{\partial x}}, \quad (2\text{-}8)$$

$$\boldsymbol{\frac{\partial c_1}{\partial t} = \frac{1}{r^2}\frac{\partial}{\partial r}\left(r^2 D_1 \frac{\partial c_1}{\partial r}\right)}, \quad (2\text{-}9)$$

$$\boldsymbol{j_n = \frac{I}{F} = \frac{i_0}{F}\left(exp\left(\frac{\alpha_a F}{RT}(\phi_1 - \phi_2 - U)\right) - exp\left(-\frac{\alpha_c F}{RT}(\phi_1 - \phi_2 - U)\right)\right)}, \quad (2\text{-}10)$$

$$\boldsymbol{i_0 = F k_0 (c_{2s})^{\alpha}(C_{max} - C_{1s})^{\alpha} {C_{1s}}^{\alpha}}, \quad (2\text{-}11)$$

where ϕ_1 is electric charge in a solid phase, c_1 is the concentration of lithium in a solid phase, I is the applied current density, and σ_{eff} is the effective conductivity of a solid matrix.

2.3.3 Heterogeneous Microstructural resolved model

In homogenous models such as single-particle and P2D models, the electrode structure is completely assumed to be a perfectly mixed solution of solid particles and the pore electrolyte. This assumption simplifies the geometry from 3D particle structures to one geometrical domain for solid particles and pore electrolyte. Then, the effective charge and mass transfer properties can be defined based on porosity and tortuosity to consider the effects of the specific geometry and the particles. Whereas, in heterogeneous models, the solid particles and pore electrolyte are defined in separate domains. In these models, the charge and mass transfers define in their related domain based on a reconstructed morphology of the electrode; therefore, heterogeneous models have higher reliability since they consider the effect of the electrode microstructure on the performance of the battery. In this thesis, X-ray computed tomography (XCT) technology has been employed to reconstruct the 3D morphology

of electrodes. In the following section, XCT working principles and its application in LIBs briefly described.

2.4 Electrode Imaging

2.4.1 X-Ray Computed Tomography (XCT)

XCT is mostly known as a medical imaging procedure to produce cross-sectional images of a targeted area to see the inside of the object without cutting by employing x-ray measurements. Recently, XCT technology widely utilized in porous media [55], batteries [26], and fuel cell [56, 57] applications to obtain the microstructure tomography. Computed tomography refers to a computerized x-ray imaging procedure in which a narrow beam of x-rays pointed to the object and rotated around it to generate cross-sectional images (slices). The collected slices can be digitally stacked to form a three-dimensional image. The main advantage of XCT compared to other imaging techniques such as FIB-SEM [58] is the non-destructive nature of XCT. Electrodes imaging in this dissertation was performed by transmission x-ray microscopy (TXM) at the advanced photon source of the Argonne National Laboratory. Figure 2-2 shows the operation principals of XCT. Firstly, focused x-ray passing through the sample and Frensel zone plane focuses the x-rays at the detector. TXM requires a series of 2D x-ray transmission images (radiographs) around a single axis of rotation. Therefore, the sample is placed on a rotary stage to facilitate 180˚ imaging. XCT slice images has a predefined thickness which is presents by voxels. A XCT slice can be computationally reconstructed by combining a set of radiographs.

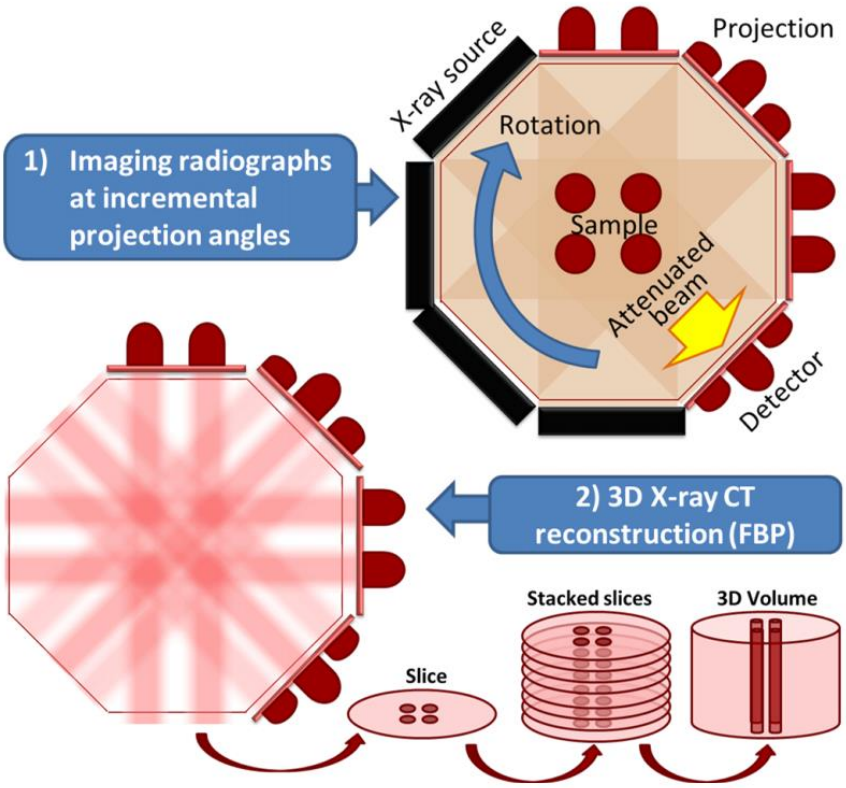

Figure 2-2 XCT Overview [59]

2.4.2 Image Segmentation

Image segmentation has a vital role in digital image processing and it refers to dividing an image into its constituent regions based on color, shape, and position [60]. Each of these regions represents a phase in the electrode, such as a solid phase or pore phase. Segmentation can be done automatically when we have decent gray level contrast or manually when the images have poor contrast. Generally, automatic segmentation is more accurate and faster than manual segmentation which is a time-consuming procedure. Among all segmentation techniques, thresholding is widely used for electrode image segmentation. The ultimate goal is to replace a grayscale image with 256 levels to an image with a fewer number of levels. The threshold value can be assigned by visual judgment based on the histogram of the image data. Moreover, there are some thresholding algorithms such as the Otsu or mean algorithm

which can be utilized to perform automatic thresholding. For instance, in the Otsu method, two phases are considered as two clusters. The grayscale values of these clusters are obtained by [61]:

$$\boldsymbol{C_1} = \sum_{\boldsymbol{i=0}}^{\boldsymbol{T}} \boldsymbol{p(i)}, \quad (2\text{-}12)$$

$$\boldsymbol{C_2} = \sum_{\boldsymbol{i=T+1}}^{\boldsymbol{255}} \boldsymbol{p(i)}. \quad (2\text{-}13)$$

The goal of this method is to maximize the variance between clusters. In the first step, the variances of the two clusters are calculated. μ_1 and μ_2 are the mean values of the clusters.

$$\boldsymbol{\sigma_1^2} = \sum_{\boldsymbol{i=0}}^{\boldsymbol{T}} \boldsymbol{(i-\mu_1)^2 p(i)}, \quad (2\text{-}14)$$

$$\boldsymbol{\sigma_2^2} = \sum_{\boldsymbol{i=T}}^{\boldsymbol{255}} \boldsymbol{(i-\mu_2)^2 p(i)}. \quad (2\text{-}15)$$

Then, the variance between the clusters is calculated. μ is the mean value of all grayscale values.

$$\boldsymbol{\sigma_{Bi}^2} = \boldsymbol{C_1(\mu_1-\mu)^2 + C_2(\mu_2-\mu)^2}, \quad (2\text{-}16)$$

$$\boldsymbol{\sigma_T^2} = \boldsymbol{C_1\sigma_1^2 + C_2\sigma_2^2}. \quad (2\text{-}17)$$

In this method, the threshold value is obtained by maximizing the ratio of $\frac{\sigma_{Bi}^3}{\sigma_T^2}$. In this study, AVIZO software was utilized to identify phases in grayscale CT images and reconstruct 3D morphology. AVIZO software has various built-in algorithms to increase contrast. For instance, a median filter is a non-linear digital filtering technique, often used to preserve edges while removing noise. Such noise reduction is a typical pre-processing step to improve the results of later processing like segmentation or edge detection. Moreover, the dilation algorithm can be implemented to smooth boundaries and remove possible false threshold segmentation gradient-induced errors at the active material particle boundaries.

Chapter 3
Multi-scale Multi-Physics Modeling of Lithium-Ion Battery Composite Gr/Si Electrode

3.1 Introduction

Employing alloy-based materials as the anode active material is a promising solution to enhance the capacity of the battery due to their higher capacity compared to common anode active materials. However, a multitude of factors needs to be addressed which prevents large scale utilization of these materials, specifically, considerable volume changes during lithiation/delithiation.

Lithiation/delithiation in the layered materials such as Gr involves an intercalation mechanism, where lithium-ions can insert/extract into/from the interlayer space of these materials. Intercalation causes relatively negligible volume change and is unlikely to affect the host material structure [62]. However, the total number of lithium insertion sites is limited, which restricts the total capacity [63]. On the other hand, some materials such as Si, Sn, etc. host lithium-ions thorough an alloying mechanism, which involves bond formation during lithiation and bond breaking during delithiation [64]. Although the specific capacity from the alloying mechanism is higher, the large number of lithium-ions reacted trigger a remarkable volume change during lithiation/delithiation. Due to this, the unstable SEI layer and high stress evolution are the major reasons for capacity degradation in LIBs with Si-based anodes.

Mathematical models have been effective in electrode design and optimization [14]. Specifically, detailed mathematical modeling can accelerate the process of optimizing composite electrodes and addressing the bottleneck challenges. Most of the developed models for composite electrodes can predict the cycling performance of fabricated cells [50, 65, 66]. Based on Newman's pseudo-2D (P2D) model [51, 67], Albertus *et al.* developed a mathematical model for the $Li_yMn_2O_4$/ $Li_yNi_{0.8}Co_{0.15}Al_{0.05}O_2$ composite cathode which accurately predicts the experimental half-cell

performance [52]. Mao *et al*. used a similar model to determine the ratio of two active materials in an unknown composite electrode. The compositions were found to be $LiMn_2O_4$ (LMO) and $LiNi_xMn_yCo_{1-x-y}O_2$ (NMC) from scanning electron microscope (SEM) and energy dispersive X-ray spectroscopy (EDX). To determine the ratios, they compared the simulated performance of composite electrodes at different ratios against the experimental data. The best curve fit of the simulation and experiment provided the LMO/NMC ratio [53].

All the studies listed above tested active materials that experience negligible volume change during cycling, whereas Si particles have considerable volume change during lithiation/delithiation. To account for the volume change, mechanical stress experienced inside the electrode during cycling should be simulated. To address this, Wang *et al.* developed a stress-strain model to calculate the large deformation of Si nano-spheres upon lithiation. The simulation results showed good agreement against the lithiation time and lithiation phase thickness growth was achieved from *in situ* transmission electron microscopy (TEM) [68]. In subsequent work, the authors developed a model to investigate the stress evolution of pure Si upon lithiation/delithiation [14, 69]. The model coupled the electrochemical kinetics, species transfers, and mechanical stress to find the effect of large deformation of the Si particles on the cell electrochemical kinetics[14]. Recently, Gao *et al.* published a modeling framework for a Si-C composite anode. They investigated the effect of Si weight percentage in the composite electrode on the cell performance and stress evolution; however, they did not consider the effect of the lithium chemical potential in Si and how it changes under stress [70]. In fact, stress causes a free energy difference between Si and Li_xSi which leads to a chemical potential change of lithium within Si [69]. Therefore, considering the chemical potential changes can enhance the accuracy of the developed models for the Si-based composite electrode. In other words, hydrostatic stress in Si particles can retard the lithiation, resulting in an unlithiated core and a large lithium concentration gradient within the Si particle, which causes capacity fade.

Overall, inadequate fundamental understanding and quantitative insights on the Si-based composite electrode is one of the main challenges that hinder further development of this electrode. A multi-scale modeling framework can provide quantitative insights about the mechanical and electrochemical behavior of the composite Gr/Si electrode. To the best of knowledge, there is no universal multi-scale model developed for Gr/Si composite electrodes that considers chemical potential changes of lithium within Si particles and are compatible with a wide compositional ratio. In the present study, a multi-scale model is developed for the Gr/Si electrode based on integrating an electrochemical and a solid mechanics model. The electrochemical sub-model includes the diffusion equation in the electrolyte and active materials, electrolyte potential, and potential of the active materials. Moreover, the solid mechanics sub-model employs a thermal-mass diffusion analogy to simulate the Si expansion/contraction during lithiation/delithiation. Incorporating the effect of stress on the lithium chemical potential within Si particles at microscale modeling can enhance the composite electrode model fidelity and shed light on the lithium concentration gradient within Si due to the stress. The developed model is then employed to investigate the effect of the Si percentage on the electrode behavior. In this way, the model is simulated for three different Si percentages, validated by the electrodes fabricated with different Gr/Si composition ratio.

This chapter is structured in the following format: first, the electrode fabrication and performance testing are discussed. Then, the modeling steps and governing equations for the electrochemical and mechanical sub-models are presented. The modeling framework was implemented in COMSOL Multiphysics 5.5. Finally, the simulation results are presented and profoundly discussed with concluding remarks.

3.2 Experiment

In this study, coin cells were fabricated to determine the electrochemical performance of the composite Gr/Si electrodes. Si nanoparticles (diameter ~100 nm) were purchased from Nanostructured & Amorphous Materials, Inc., USA. Spherical natural Gr with a diameter ranging from 10 μm to 30 μm was purchased from MTI Corporation, U.S. PVDF was used as a binder material and carbon Super-P as a conductive agent. All chemicals were used as received. The weight ratio of active materials, PVDF, and Super-P were maintained at 85:7.5:7.5 in all prepared electrodes. Four active material compositions with various ratios of Gr/Si were prepared. Gr contents were 75%, 77.5%, 80%, and 85% respectively in the fabricated electrode, and the corresponding Si contents were 10%, 7.5%, 5%, and 0% (all the percentages are in mass %). All compositions were mixed with a rotating mixer for 10 minutes, stirred on a magnetic stirrer for half an hour, and finally sonicated for half an hour. This mixing procedure was repeated three times before the slurry was cast onto a copper foil using a doctor blade.

The cast electrodes were dried, calendared, and cut before final coin cell assembly in an argon-filled glovebox (MBRAUN, Germany). The electrolyte was 1 M lithium hexafluorophosphate in ethylene carbonate/diethyl carbonate (weight ratio 3:7). lithium metal was used as the counter and reference electrode. Charge and discharge tests were performed on a battery tester from Neware, China. Two current densities of 50 mA/g and 100 mA/g were used to study the galvanostatic charge/discharge behavior of the cells. Potentiostatic electrochemical impedance spectroscopy was performed on an electrochemical workstation (Princeton Applied Research, U.S.) with a small perturbation current. The starting and ending frequencies were 1 MHz and 0.01Hz, respectively.

3.3 Modeling

To consider the effect of volume changes and measure the stress evolution during lithiation/delithiation of the composite Gr/Si anode, the developed model comprised two sub-models: 1) electrochemical sub-model: employing a pseudo-two-dimensional (P2D) model which is based on the porous electrode and

concentrated solution theories [49, 67] to consider the diffusion within the electrolyte, diffusion within active materials (i.e., Gr and Si), potential of the electrolyte and active materials, and charge transfer kinetics at the active materials/electrolyte interface; 2) mechanical sub-model: using thermal-mass analogy to simulate the Si volume expansion/contraction [68] and measure the stress evolution during lithiation/delithiation.

3.3.1 Electrochemical Sub-Model

Lithium diffusion in the active materials is generally described by Fick's mass transport law [71]:

$$\boldsymbol{J_{Li}^{n} = -D_{Li}^{n} \nabla c_{Li}^{n}},$$

(3-1)

$$\frac{\boldsymbol{\partial c_{Li}^{n}}}{\boldsymbol{\partial t}} = \boldsymbol{-\nabla . J_{Li}^{n}}, \quad (3\text{-}2)$$

where D_{Li}^{n}, J_{Li}^{n}, and c_{Li}^{n} are the diffusion coefficient of lithium, lithium flux, and lithium concentration in the active materials and n can represent either Gr or Si. To incorporate the stress effect to the chemical potential within Si, the concentration gradient is replaced by the chemical potential gradient [69]:

$$\boldsymbol{J_{Li}^{Si} = -\frac{D_{Li}^{Si}}{RT} c_{Li}^{Si} \nabla \mu_{Li}(\sigma)}, \quad (3\text{-}3)$$

and the chemical potential can be obtained by:

$$\boldsymbol{\mu_{Li}(\sigma) = \mu_{Li} + \Delta \mu_{Li}(\sigma)}, \quad (3\text{-}4)$$

where μ_{Li} represents the lithium chemical potential within Si under zero stress and $\Delta\mu_{Li}(\sigma)$ is the change in chemical potential under stress. Employing the ideal solution assumption, lithium chemical potential can be obtained by [14]:

$$\boldsymbol{\mu_{Li} = -mFU}, \quad (3\text{-}5)$$

where m is the number of lithium-ion charges (m=1), F is Faraday's constant, and U is the open-circuit voltage. Moreover, the changes in chemical potential under stress are related to hydrostatic stress σ_h:

$$\Delta\boldsymbol{\mu_{Li}(\sigma) = \alpha\Omega\sigma_h},\tag{3-6}$$

where α is the coefficient defining the effect of hydrostatic stress on the chemical potential and Ω is the partial molar volume and represents volume changes during lithiation of one mole of lithium into Si [14]. The main advantage of considering the effect of hydrostatic stress on the chemical potential is that at the microscale, hydrostatic stress can suppress the lithium diffusion within Si particle. Therefore, an unlithiated core and a large gradient of lithium concentration cause capacity loss. On the active material/electrolyte interface, the reaction is described using Butler-Volmer kinetics [28]:

$$\boldsymbol{i^n_{pos} = i^n_{0,pos}(e^{\frac{\alpha_{pos}F\eta}{RT}} - e^{-\frac{(1-\alpha_{pos})F\eta}{RT}})},\tag{3-7}$$

$$\boldsymbol{i^n_{0,pos} = Fk^n_{pos}\left(\frac{(c^n_{Li,max}-c^n_{Li})c_{Li^+}}{(c^n_{Li,max}-c^n_{Li})c_{Li^+,0}}\right)^{\alpha_{pos}}\left(\frac{c^n_{Li}-c^n_{Li,min}}{c^n_{Li,max}-c^n_{Li,max}}\right)^{1-\alpha_{pos}}},\tag{3-8}$$

where $c^n_{Li,max}$ and $c^n_{Li,min}$ are the maximum and minimum of the lithium concentration in the active materials, and i^n_{pos}, $i^n_{0,pos}$, k^n_{pos}, and α_{pos} are the current density, exchange current density, the reaction rate constant, and apparent transfer coefficient, respectively. The active material potential and the overpotential can be calculated by [26]:

$$\boldsymbol{i^n_{pos} = -\sigma^n_{pos}\nabla\varphi^n_{AM}},\tag{3-9}$$

$$\boldsymbol{\eta^n = \varphi^n_{AM} - \varphi_E - U - i^n_{pos}R_{SEI}},\tag{3-10}$$

where φ^n_{AM}, φ_E, R_{SEI} and σ^n_{pos} are the active material potential, electrolyte potential, SEI layer resistance, and conductivity of active material, respectively. It is worth noting that in all aforementioned equations, n can be either Si or Gr. Therefore, the total current can be obtained by:

$$\boldsymbol{I_t = 3M_t\sum_{n=1}^{N}\frac{\varepsilon_n i^n_{pos}}{\rho_n R_n}},\tag{3-11}$$

where $M_t, \varepsilon_n, \rho_n,$ and R_n are the total mass of active materials, the mass fraction of active materials, density of active materials, and the average particle radius of active materials, respectively. Moreover, the transport of lithium-ion inside the electrolyte can be written as:

$$\boldsymbol{\varepsilon}\frac{\partial \boldsymbol{c_E}}{\partial \boldsymbol{t}} = \boldsymbol{\nabla}.\left(\boldsymbol{D_{eff}}\boldsymbol{\nabla c_E}\right) + \frac{\boldsymbol{a^n i^n_{pos}}(\mathbf{1}-\boldsymbol{t^0_+})}{\boldsymbol{F}}, \quad (3\text{-}12)$$

where ε, a^n, and t^0_+ are electrode porosity, the specific surface area of the active materials, and transference number. Additionally, Ohm's law will be employed to calculate the electrolyte potential:

$$\boldsymbol{i_E} = -\boldsymbol{\kappa_{eff}}\boldsymbol{\nabla \Phi_E} + \frac{\boldsymbol{\kappa_{eff} RT}}{\boldsymbol{F}}\left(\mathbf{1}-\boldsymbol{t^0_+}\right)\boldsymbol{\nabla ln\, c_E}, \quad (3\text{-}13)$$

where i_E is the current density in the electrolyte and κ_{eff} is the effective conductivity. In fact, the computed lithium concentration by electrochemical sub-model passed to the mechanical sub-model to compute the Si particle deformation during lithiation/delithiation. Then, the concentration updated with the new volume of Si particles.

3.3.2 Solid Mechanics Sub-Model

The Si deformation during cycling is due to the mechanical constraints and the lithiation/de-lithiation [68]. The ratio of the new volume V to the initial volume V_0 is proportional to the lithium concentration [72]. In a Si particle under a stress-free environment, the ratio of V/V_0 is obtained by:

$$\frac{\boldsymbol{V}}{\boldsymbol{V_0}} = \mathbf{det}(\boldsymbol{F_c}) = \mathbf{1} + \boldsymbol{\Omega}\Delta\boldsymbol{C}, \quad (3\text{-}14)$$

where F_c is the lithiation induced deformation. The Si volume expansion can be obtained by a thermal-mass diffusion analogy. The thermal strain is:

$$\boldsymbol{\varepsilon_{ij}} = \boldsymbol{\beta}\Delta\boldsymbol{T}\boldsymbol{\delta_{ij}}, \quad (3\text{-}15)$$

where β is the thermal expansion coefficient and ΔT is the temperature increase, which is equivalent to the increase of the effective concentration ΔC_{eff}. The expansion coefficient can be calculated by[68]:

$$\boldsymbol{\beta} = \frac{(\sqrt[3]{\mathbf{1}+\boldsymbol{\Omega}\Delta\boldsymbol{C}})-\mathbf{1}}{\Delta \boldsymbol{C_{eff}}}. \quad (3\text{-}16)$$

To estimate the stress formation, the Cauchy stress tensor σ can be derived based on deformation F, and second Piola-Kichhoff stress S by [73]:

$$\boldsymbol{\sigma} = (\mathbf{det}(\boldsymbol{F}))^{-\mathbf{1}}\boldsymbol{FSF^T}. \quad (3\text{-}17)$$

In microscale, the lithium concentration in Si particle is calculated by employing the aforementioned electrochemical model as well as the Si particle deformation and stress evolution based on the mechanical model. Then, the averaged updated lithium concentration based on the new volume of Si particle is passed to the macroscale where the electrode electrochemical behavior is modeled with considering Gr and Si as two separate active materials of a porous electrode. Consequently, the current density is passed from the macroscale to microscale.

The Si particle size is relatively smaller than Gr and can be assumed that in a composite electrode, Si particles are constrained with Gr and binder. Therefore, in the mechanical sub-model, it is assumed that one-quarter of Si particle surface area has a fixed constraint and half a quarter of the surface area has a roller boundary condition (Figure 3-1). The other boundaries can freely expand due to the porous nature of the composite electrode. Moreover, the macroscale and microscale boundary conditions are presented in Figure 3-1.

Integrating these two aforementioned sub-models leads to a comprehensive framework for the modeling of Si-based composite electrodes. Although in this work there are only two types of anode active materials, Gr and Si, the developed model is scalable to more complex composite electrodes. Moreover, the developed model has a relatively low computational cost and can be employed for on-line estimation of Si-based battery states, such as state of charge, state of health, and state of power. The model parameters are listed in Table 3-1. To obtain the deformation of Si during cycling, the Si

mechanical properties such as its Poisson's ratio, elastic modulus, and yielding stress should be determined. The assumed Poisson's ratio is based on the Shenoy *et al.* report [74] varying from 0.28 to 0.24 depending on the state of charge; the yielding stress range is 1.6-0.6 GPa [75], and Young's modulus is 50 GPa [76]. The modeling framework is illustrated in Figure 3-1. The electrode assumed to have an isotropic microstructure and the lithium diffusivity is not concentration dependent. The effective diffusivity is calculated based on using bilk diffusion coefficient and the Bruggeman correlation. The partial molar volume of Li in Si represents the volume changes of a host Si particle after accommodating one mole of Li.

Table 3-1 List of the model parameters

parameter	Symbol	Si		Gr
Electrode thickness(m)	L		*5.5 × 10^{-5}	
Radius of type n particle (m)	R_n	*5×10^{-8}		*10^{-5}
Cathode area (m^2)	A		*1.01× 10^{-4}	
Binary diffusion coefficient of Li in type n particle (m^2s^{-1})	D_{Li}^n	3× 10^{-16} [14]		6.51× 10^{-11} [77]
apparent transfer coefficient	α_{pos}		0.5[54]	
Electrode porosity	$\boldsymbol{\varepsilon}$		.35[53]	
Initial electrolyte concentration (mol m^{-3})	c_e		*1000	
Li-ion transference number	t_+^0		0.36[54]	
Separator thickness (m)	L_{sep}		*2.5 × 10^{-5}	
Bulk diffusion coefficient in the electrolyte (m^2/s)	D_e		1.27× 10^{-11}	
Separator porosity	$\boldsymbol{\varepsilon}_{sep}$		0.55[c]	
Exchange current density on Li foil electrode (A/m^2)	i_f^0		20[54]	
Faraday constant (C/mol)	F		96478	
Gas constant (J/mol K)	R		8.314	
Temperature (K)	T		298	
Partial molar volume of Li in Si (m^3/mol)	Ω		9× 10^{-6} [78]	

*: measured, c: Celgard product data sheet

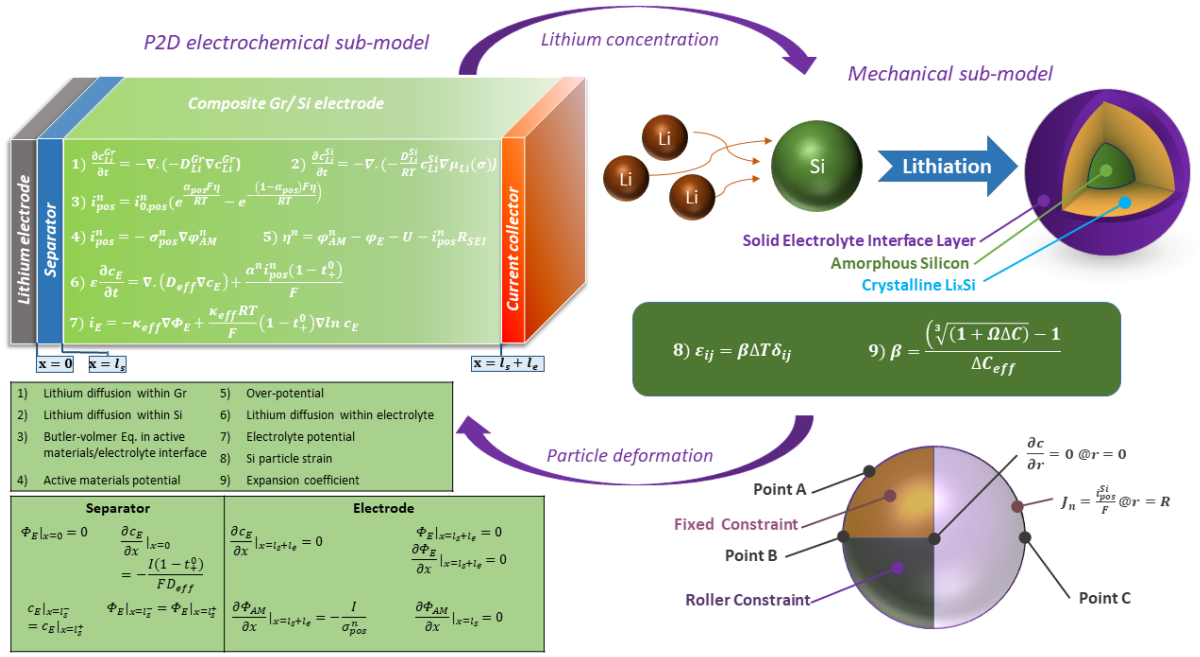

Figure 3-1 Modeling methodology

3.4 Results and Discussion

Si particle size affects the composite electrode cycle life, where smaller Si particles have a lower volume change and particle pulverization is less likely to occur. The SEM images of the composite electrodes with Si wt% of 5, 7.5, and 10% are illustrated in Figure 3-2. It is worth noting that the dispersed distribution of Si particles verifies that employing a P2D model with two active materials is a reasonable approach to model a Gr/Si composite electrode, and integrating with a solid mechanic model to incorporate the Si particles deformation throughout lithiation/delithiation. The average particle size of Gr and Si is approximated as 10 μm and 50 nm, respectively.

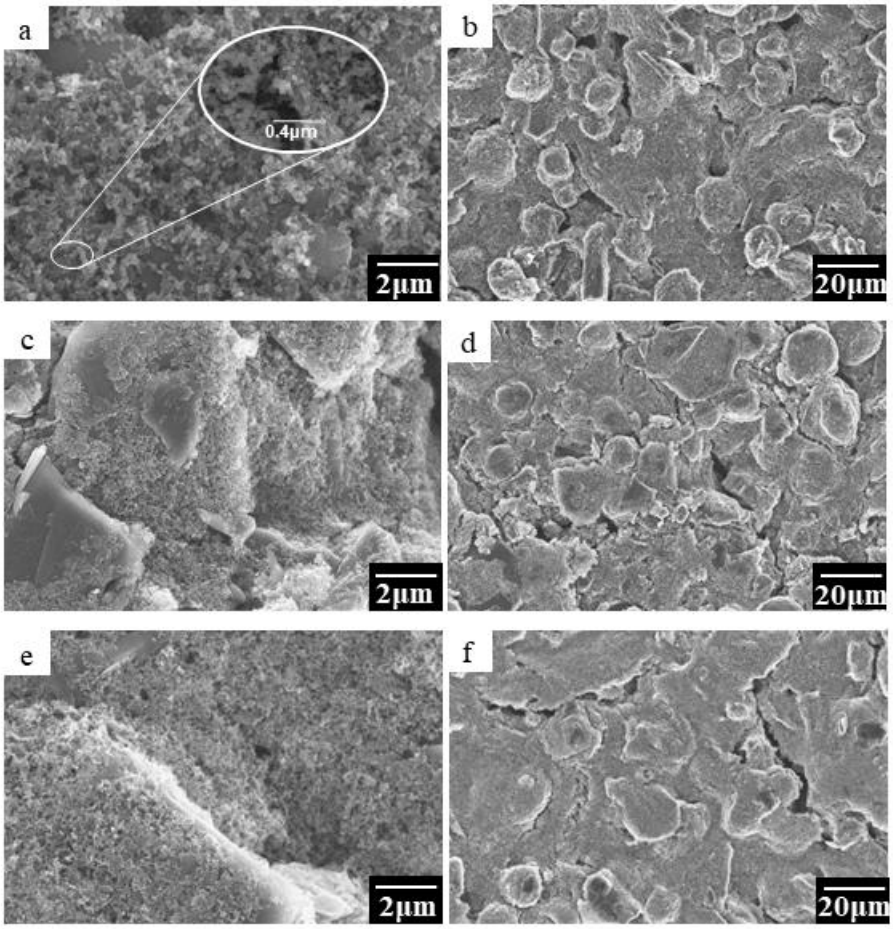

Figure 3-2 SEM images of the composite Gr/Si electrode with (a-b) 5% Si, (c-d) 7.5% Si, and (e-f) 10% Si.

3.4.1 Impedance Measurements

Electrochemical Impedance Spectroscopy (EIS) is an effective tool to investigate the impedance evolution of the composite Gr/Si electrode during the charge/discharge cycles. Typically, the EIS of the lithium-ion batteries consists of two partially overlapped semicircles and a sloping straight line at low frequency [79]. The R_b is the bulk cell resistance which depends on the electrical contact resistance in the current collectors, resistance in the outer circuit, the electric conductivity of the electrodes, electrolyte, and separator, and the ionic conductivity of the electrolyte. Furthermore, the diameter of the semicircle depends on charge transfer resistance and SEI layer parameters, such as the R_{SEI} and C_{SEI}

which are the resistance and the capacitance of the SEI layer of the electrodes, respectively. In other words, R_{SEI} accounts for the ionic diffusion resistance of the lithium-ion in the SEI layer [80]. W is the Warburg impedance which indicates the diffusion of lithium through electrode [81]. The EIS of the pure Gr electrode is compared to the composite electrode with different Si wt% after the first charge. As shown in Figure 3-3, the diameter of high-frequency semicircles of the composite electrodes is larger than that of the pure Gr electrode, which means that the composite electrodes have a higher charge transfer resistance compared to pure Gr electrode. The main reason for EIS analysis is to incorporate the SEI layer resistance into the developed model. Therefore, an equivalent circuit model was fitted to the EIS data to obtain the R_{SEI} at various Si percentages, as seen in Table 3-2. The fitted equivalent circuit model is presented in Figure 3-3b. The estimated SEI resistance was incorporated into the developed model for overpotential calculation.

Table 3-2 Composite electrode resistance parameters based on the equivalent circuit model

	0% Si				5% Si				7.5% Si			
	R_b	R_{SEI}	R_1	R_2	R_b	R_{SEI}	R_1	R_2	R_b	R_{SEI}	R_1	R_2
1st charge	3.85	9.32	22.66	15.55	12.55	13.58	28.89	19.8	5.49	54	38.1	37.3

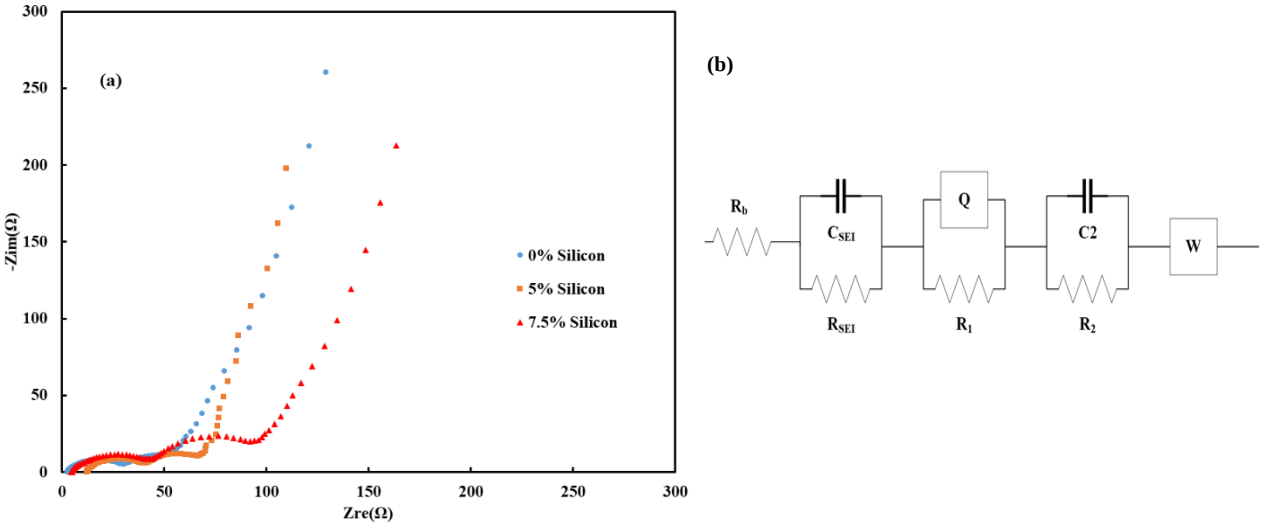

Figure 3-3 (a) EIS analysis of the composite electrode versus pure Gr electrode after the 1st cycle and (b) equivalent circuit model of the composite electrode

3.4.2 Performance prediction

The open-circuit voltage of pure Gr and Si is presented in Figure 3-4a. To obtain the open-circuit voltage profile, pure Gr and Si electrodes were fabricated and galvanostatically discharged at a very low rate of 8 mA/g. The experimental results of the galvanostatic discharge performance of composite Gr/Si electrodes at 100 mA/g after the second discharge are shown in Figure 3-4b. The composite Gr/Si electrodes have various ratios of 5%, 7.5%, and 10% Si. In fact, a higher Si percentage leads to a higher cell capacity. The total capacity of the cell with 10% Si is 600 mAh/g, which is 19% and 47% higher than the cell with 7.5% and 5% Si respectively. To validate the developed model, the simulation data obtained based on the described electrochemical-mechanical model (Modeling section) were compared with the experimental results at two currents. As illustrated in Figure 3-4c, the developed model can accurately predict the total capacity and the voltage plateau of the composite electrode at various currents and composition ratio. Indeed, the voltage plateau is a vital indicator of the on-line estimation of the battery state of charge. Therefore, the developed framework can be expanded for the on-line

estimation of the batteries' state of charge with the Si-based electrode. In fact, available electrochemical battery state estimation models cannot be accurately applied for Si-based electrodes since they do not consider the effect of Si volume changes and stress evolution.

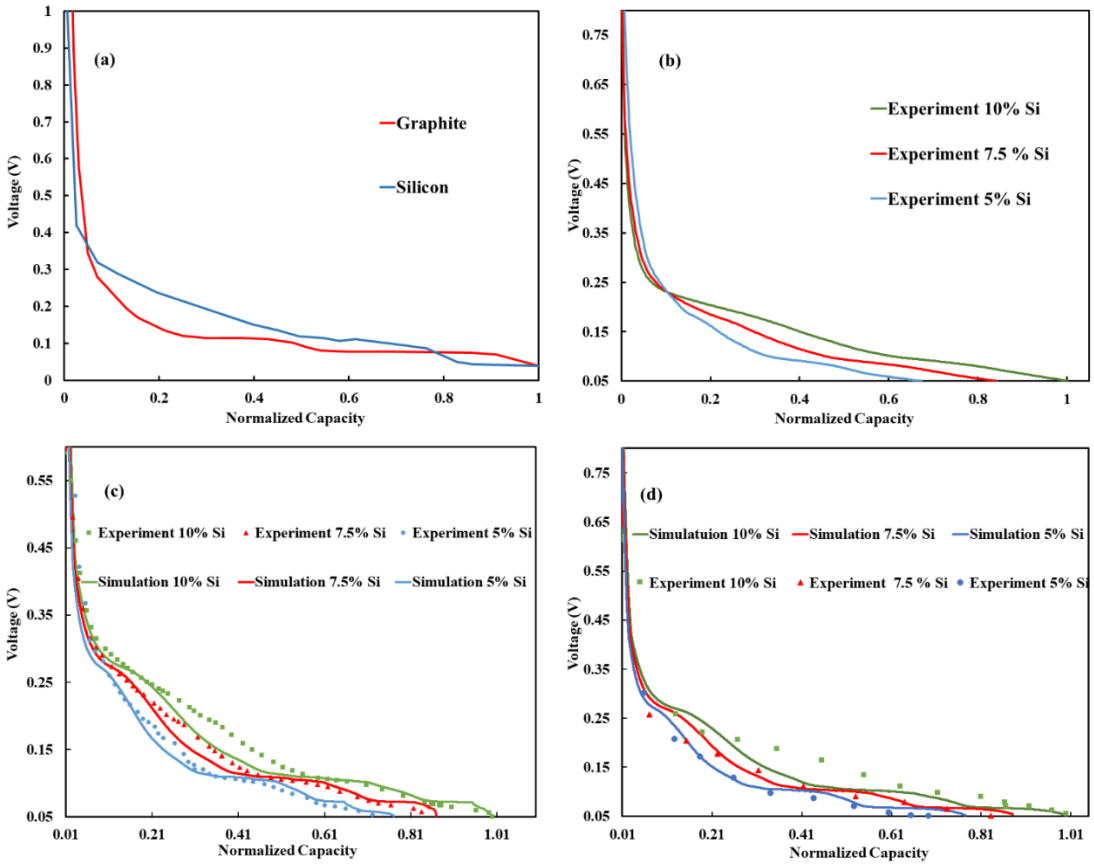

Figure 3-4 Open circuit voltage of Si and Gr (a), the discharge rate of the composite electrode with a different composition at 100 mA/g rate (b), experimental data versus simulation results at (c) 50 mA/g and (d) 100 mA/g.

3.4.3 Effects of Si percentage

Increasing the Si percentage in a Si-based composite electrode favorably enhances the cell energy density, although higher Si percentage can exacerbate the cell degradation due to the larger volume

changes and stress formation. Therefore, finding an optimal tradeoff of Si percentage and total capacity is a critical challenge in Gr/Si composite cell design and fabrication. Moreover, constraints can affect the stress evolution in Si particles. Thus, to incorporate the effect of external constraints, three points are considered on a Si particle: point A cannot expand due to the external constraints, point B is located at the interface of the fixed region and free region, and point C can freely expand. As illustrated in Figure 3-5a, point A has compressive stress during lithiation, but point C has an entirely tensile stress. Moreover, point B has compressive stress at the beginning of lithiation due to the dominant effect of external constraints and a transition to tensile stress throughout the lithiation. This transition may cause mechanical degradation and exacerbate the crack formation. Previously, this behavior was reported for stress variation in radius-direction of Si particles [69]. It is worth noting that at the end of discharge the compressive stress at point A is about threefold the tensile stress at point C. In other words, external constraint has a vital role in the stress evolution of Si particles. To address this challenge, providing free space in the composite electrode microstructure is beneficial. Additionally, with increasing the Si wt% from 5% to 10%, hydrostatic stress becomes higher. The main reason is that at higher Si percentage, the composite electrode tends to have larger volume changes, which lead to higher hydrostatic stress at the same operating condition (Figure 3-5).

As presented in Figure 3-5b, lithium concentration within Gr is much lower than Si, which is expected considering the theoretical capacities of Gr and Si. With increasing Si wt% in the Gr/Si composite electrode, the trend in lithium concentration within Gr during lithiation remains almost identical, while there is a slight decrease in lithium concentration in the Si particles. The reason for this lower concentration is that at a constant current there is a larger number of Si particles to host the lithium-ions. To extensively elaborate the effect of external constraints on the Si particles, von Mises stress evolution throughout the particle diameter during the lithiation is illustrated in Figure 3-5c and 5d for 10% and 5% Si, respectively. At the end of lithiation, the particle has the highest stress. The left

boundary represents the free point and it has relatively lower stress compared to the right boundary, which is point B located at the interface of the fixed and free regions. In other words, the von Mises stress has a remarkable value at the end of lithiation in point B due to the external physical constraint (Figure 3-5c). Moreover, the composite electrode with lower Si percentage follows the same trend; however, the estimated von Mises stress is lower due to the decreased tendency of the composite electrode toward expansion (Figure 3-5d).

With a closer look at Figure 3-5c-d, there is a local maximum of stress near the center of the Si particle (x=0.5). In fact, the lithiation induced stress inside the Si particles retard the lithiation process. Therefore, the Si particles would have a core-shell structure comprising a lithiated shell and an unlithiated core[63] (Figure 3-1). The unlithiated core results in a decreased capacity, while the incompatible strain at the interface of the core and the lithiated shell leads to a higher von Mises stress. Additionally, the local peaks have a tendency to the right side (point B), which illustrates the anisotropic swelling of Si particles due to the external constraint effect.

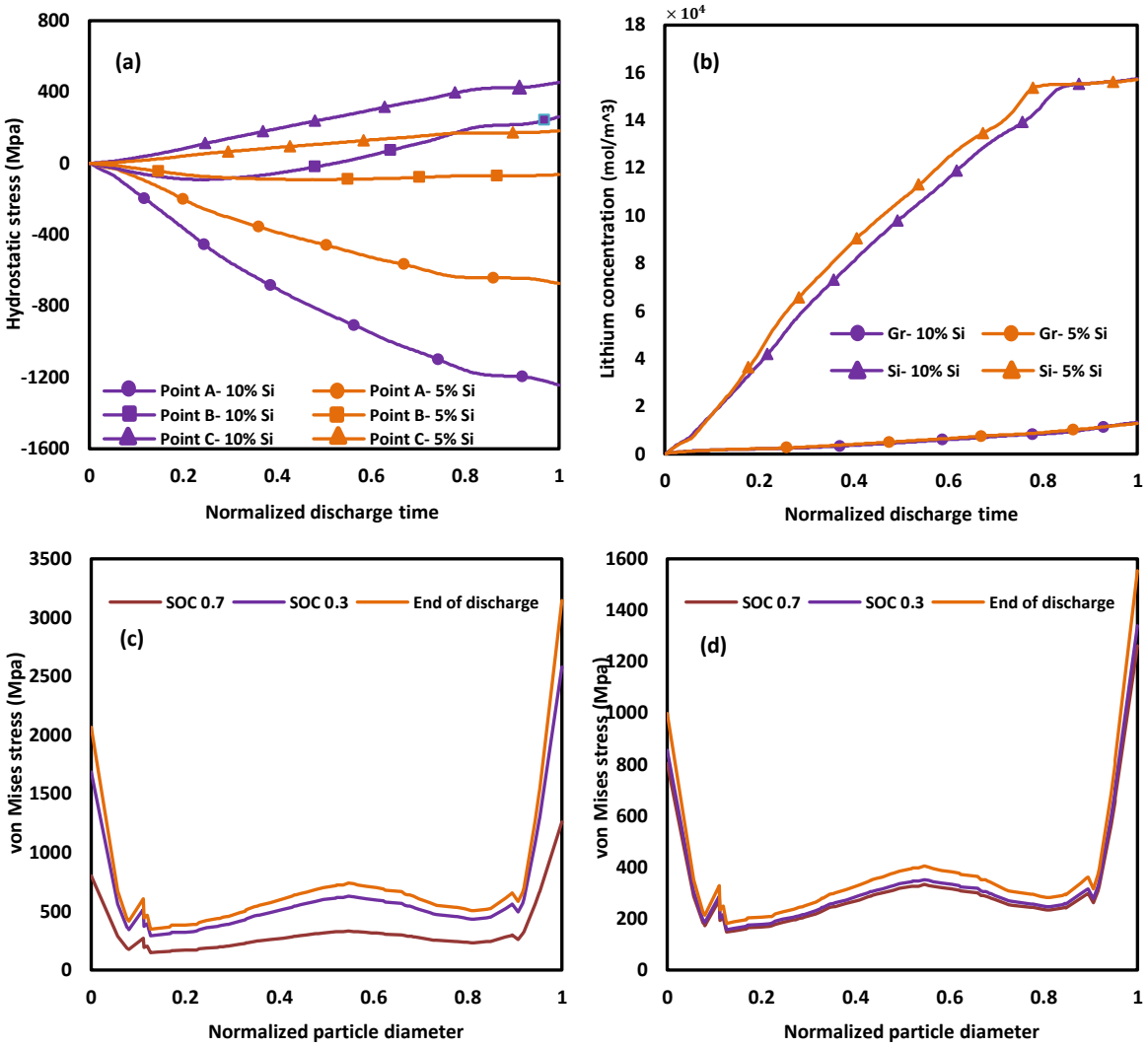

Figure 3-5 (a) Hydrostatic stress of Si particles during discharge and (b) lithium concentration in Gr and Si at two compositional ratio at 50 mA/g discharge current and von Mises stress through particle diameter at (c) 10% Si and (d) 5% Si

3.4.4 Effects of the current

Rate performance analysis can shed light on the effect of current on the composite electrode performance. The lithium concentration in the active materials, hydrostatic stress, and deformation ratio at two currents (50 and 100 mA/g) are illustrated in Figure 3-6. Increasing the current results in a lower average lithium concentration in the Si particles and a slightly lower amount in Gr particles. The main reason is that at a high current rate there is a capacity loss. During discharge, a predefined cut-off voltage will stop the current when the surface concentration reaches its maximum value. However, there is a lithium concentration gradient inside the electrode active material particles, which limits the total deliverable capacity. This concentration gradient in Si particles at high current is considerable due to the higher lithium concentration within Si particles compared to Gr (see Figure 3-6a). Moreover, at high current, the cell has higher overpotential which intensifies the capacity loss.

Although increasing the current unfavorably decreases the total capacity, it triggers less deformation and hydrostatic stress in Si particles. As plotted in Figure 3-6b, the hydrostatic stress during lithiation in all three points of A, B, and C is slightly lower at higher current. Implementing the same analogy for higher currents, it is concluded that employing composite Si-based electrodes can be a promising solution for the next generation of lithium-ion batteries with higher energy density and is compatible with fast charging, where at higher currents the Si particles encounter less stress evolution and deformation. Si particles have 12% more expansion at the end of lithiation with the lower current rate (see Figure 3-6c). Limiting the volume changes by increasing the current can be highly beneficial to restrict cell degradation and mechanical failure. Moreover, at high current, the von Mises stress is slightly lower throughout the Si particle due to the smaller stress evolution; therefore, crack formation is less likely to happen (Figure 3-6d).

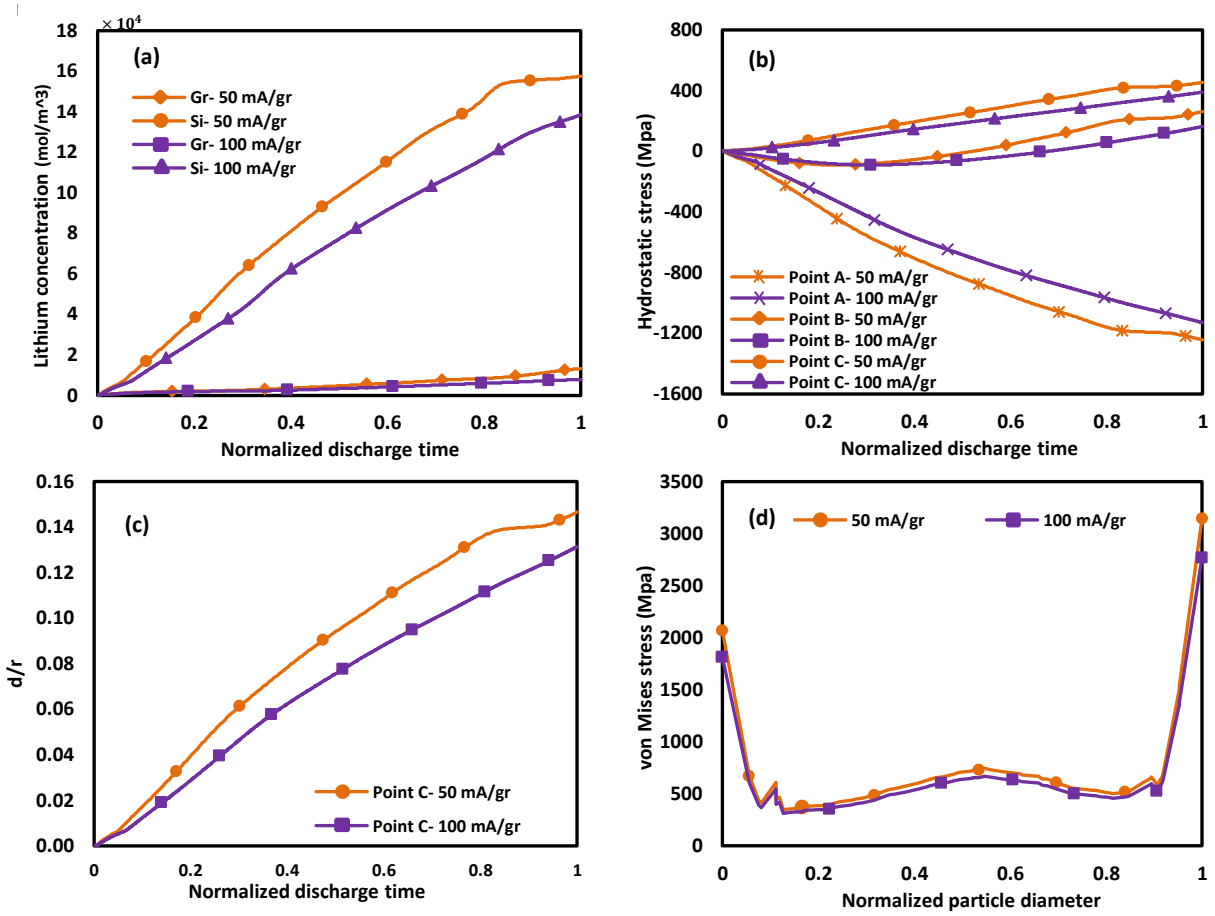

Figure 3-6 Effects of current rate on the (a) Li concentration in Gr and Si, (b) hydrostatic stress of Si particles, and (c) deformation of Si particles in a composite Gr/Si electrode with 10% Si

3.4.5 Effects of high Si percentage

As mentioned, the developed framework is applicable for a wide range of composite electrodes, considering the effect of volume changes and stress evolution throughout lithiation/delithiation. The ultimate goal is to maximize the capacity with acceptable cycle life. Therefore, in this section, the effect of increasing the Si wt% up to 20% is investigated. As illustrated in Figure 3-7a, the hydrostatic stress at the interface point (point B) dramatically increased when changing the Si percentage from 10% to 20%. At the end of lithiation, it is higher than point C which can freely expand. In other words, the impact of physical constraints becomes more critical at higher Si mass loading while the wide range of stress in point B from compressive to tensile stress could tremendously affect the cycle life. Moreover, point A stress evolution follows the expected trend while external physical constraint causes growing compressive stress during lithiation. Increasing Si mass loading can exacerbate stress formation. At the end of lithiation for the 20 wt% Si composite electrode, point A, B, and C have 62%, 565%, and 130% higher hydrostatic stress compared to the composite electrode with 10 wt% Si.

Another remarkable aspect is the deformation ratio of the Si particles during cycling. This ratio is a vital parameter in the microstructure design of Si-based composite electrodes as well as the macroscale cell design. Si volume change is inevitable due to the intrinsic behavior of Si alloying; however, a clear robust estimation of Si deformation can accelerate the Si-based composite electrode microstructure design. As presented in Figure 3-7b, the deformation ratio in the composite electrode with 20% Si is 71% higher than the electrode with 10% Si. Therefore, the composite electrode microstructure should be able to accommodate these volume changes to avoid excessive stress and crack propagation. Additionally, the von Mises stress at the surface of the Si particle, especially point B (right side of Figure 3-7c) becomes larger at higher Si percentage. For instance, for a composite electrode with 20 wt% Si compared to 10 wt% Si, the von Mises stress at point B is 98% higher.

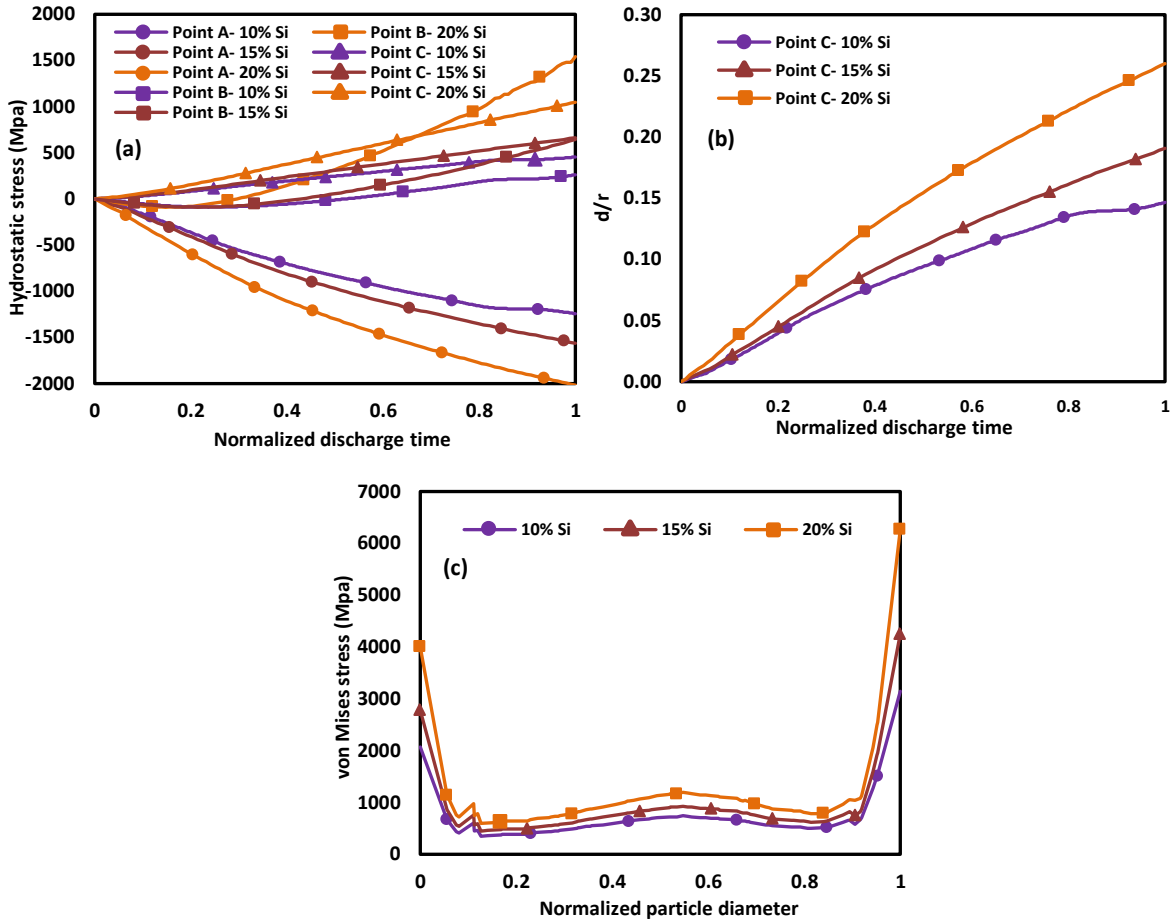

Figure 3-7 Effects of high Si percentage on the (a) hydrostatic stress, (b) deformation ratio, and (c) von Mises stress thorough particle diameter in three composite electrodes discharged with 50 mA/g current.

3.5 Conclusions

In this study, a multi-scale electrochemical-mechanical modeling framework was developed for a composite Gr/Si electrode. The experiments were conducted with the different compositional ratios of Gr and Si, and galvanostatically cycled at two currents to validate the developed model. EIS analysis was performed to estimate the SEI layer resistance based on fitting an equivalent circuit model to the experimental data. Then, the obtained resistance was incorporated into the model for overpotential to increase accuracy. The developed framework is comprised of an electrochemical sub-model developed based on a P2D model for a composite electrode with two active materials, Gr and Si, integrated with a solid mechanics' sub-model. The solid mechanics sub-model employed a thermal-mass analogy to obtain the Si deformation during cycling.

The presented model has a good agreement with the experimental data conducted in different currents and various compositional ratios of Gr and Si. Increasing the Si wt% from 5% to 10% increased the tensile and compressive stresses up to 2.5 and 1.8 times, respectively. Moreover, physical constraints have a vital effect on the Si stress evolution and deformation, while Si particles encounter compressive and tensile stresses concurrently during cycling. For instance, at the end of lithiation for a composite electrode with 10 wt% Si, a fixed point on a Si particle under external mechanical constraints experienced 1243 MPa compressive stress, whereas a free point has 454 MPa tensile stress. Furthermore, lithiation induced stress inside the Si particles retard the lithiation process, forming a core-shell structure that comprises a lithiated shell and unlithiated core. The unlithiated core results in a decreased capacity, while the incompatible strain at the interface of the unsaturated core and lithiated shell leads to a higher von Mises stress with an anisotropic swelling of particles due to the external constraint effect.

Chapter 4
Three-Dimensional Modeling of All-Solid-State Lithium-Ion Batteries Using Synchrotron Transmission X-ray Microscopy Tomography

4.1 Introduction

As mentioned, LIBs have dominated the electrochemical energy storage market for over a decade due to their high energy density, high design flexibility, and long cycle life [82, 83]; however, electric vehicles or medical instruments require LIBs with higher safety and a wider thermal stability range [15, 84]. All-solid-state lithium-ion batteries (ASSBs), which are based on solid electrolytes (SEs), are a safer alternative to the conventional liquid electrolyte LIBs. One of the main drawbacks of ASSBs is poor SE/AM contact due to the solid/solid nature of this interface. Since the two solid phases are not perfectly in contact with each other, void spaces block the ion pathways at the SE/AM interface, thus negatively affecting the ASSB performance [22].

Mathematical models have been proven to be an efficient way to shed light on the physical and electrochemical phenomena occurring in LIBs. Experimentally validated models can provide indispensable insight into their performance and limiting challenges. Mathematical models have been previously applied to simulate the charge/discharge performance of ASSBs [85-88], but most of these models are one dimensional (1D) and do not include the real microstructure of the electrode and SE in their modeling framework. For instance, Danilov *et al.* developed the first model that included 1D charge transfer kinetics at the SE/AM interface, diffusion and migration of ions in the SE, and diffusion of ions in the intercalation AM [86]. While their model could simulate the galvanostatic charge/discharge profiles at low to moderate c-rates in good agreement with experimentally measured data [86], their model failed to predict the performance at high current rates. Kazemi *et al.* addressed this issue by defining a variable AM diffusion coefficient as a function of lithium concentration instead

of an assumed constant value [85], allowing them to simulate the voltage profiles accurately at low and high current rates up to 50 C (5 mA cm^{-2}). Raijmakers *et al.* improved the accuracy of the 1D model by considering mixed ionic/electronic conductivity in the positive electrode, electrical double layers at the SE/AM interfaces, and defining the ionic/electronic diffusion coefficient as a function of lithium concentration in the AM [88]. With this improved model, they showed that overpotential in the SE is the main contributor to the overall voltage losses during discharge, while charge transfer losses are another major reason for battery performance losses in addition to electrical double layer losses at the SE/AM interface and diffusion in the positive electrode [88]. In terms of the SE, all the aforementioned models are based on a binary electrolyte assumption and electro-neutrality in the SE; Wolff *et al.* tried to elucidate fundamental differences between single-ion and binary conducting electrolytes by implementing a pseudo-two dimensional (P2D) single-ion model [89]. They demonstrated that a single-ion conduction cell produces higher capacity by exhibiting less voltage losses within the electrolyte. This makes the single-ion a better alternative to binary electrolytes specifically for high current and high energy (thick electrode) applications. In terms of the ASSB electrode design and microstructures, further investigation of the effects of electrode geometry and homogeneity is critical to identifying the optimal electrode structure [89]. Bates *et al.* developed a 2D model for ASSBs to obtain lithium concentration and voltage profiles using simplified rectangle shapes [90]. Clancy *et al.* compared the performances of ASSBs with three structures (thin film, 3D core-shell, and 3D electrodes) and showed that implementing 3D nanostructures can effectively enhance the areal energy and power density compared to a thin-film electrode [91]. Although these models can simulate the charge/discharge performance, they cannot describe in detail the physical and electrochemical behavior of the ASSB; specifically, they fail to describe the effects of electrode microstructure's heterogeneity on the lithium-ion transport within the SE and AM, as well as their interface.

One way to investigate the physical and electrochemical behavior of ASSBs is to use the 3D reconstructed geometry of the ASSB electrode instead of simplified 1D or 2D geometries. Among electrode imaging techniques, a non-destructive CT imaging technique is widely utilized to characterize the physical and morphological properties of the electrode including directional tortuosity, porosity, particle size distribution, and specific surface area [28, 30-32]. For instance, Banerjee *et al.* investigated the effects of compression on the permeability, diffusivity, and pressure drop using CT images [92]. They showed that the compression resulted in a 58% reduction in permeability and a 25% reduction in diffusion [92]. However, there are only a few studies that have been done on the 3D reconstructed microstructure of ASSBs [21, 22, 93, 94]. Li *et al.* reconstructed the real 3D geometry of an ASSB using synchrotron transmission X-ray microscopy tomography [22]. They showed that particle-based ASSBs have a critical SE/AM interfacial issue that highly influences the lithium-ion transport and intercalation reaction rate, causing low capacity, poor rate capability, and cycle life [22]. Tippens *et al.* used in-situ CT to investigate the SE/lithium metal electrode interface during cycling [93]. They demonstrated that fracture formation is the main reason for the impedance increase during cycling [93]. Choi *et al.* reconstructed an ASSB composite cathode with FIB-SEM to analyze its physical properties including volume ratio, connectivity, tortuosity, and pore formation [21]. Later, they analyzed the electrochemical lithiation/delithiation inside ASSB composite cathodes with 3D atom-probe tomography [94], showing that poor SE/AM contact triggers significant lithium-ion variation during lithiation/delithiation [94].

Overall, there is a knowledge gap in understating the SE/AM interface that hinders the further development of ASSBs [15]. 3D reconstructed microstructures can be used as the model geometry along with a multi-physics modeling framework to provide quantitative insights about the mechanical and electrochemical behavior of ASSBs. To the best of the authors' knowledge, there is no multi-physics model developed for ASSBs based on the 3D reconstructed electrode. In the presented study,

a multi-physics model is developed for ASSBs based on the reconstructed 3D morphology of electrodes for an ASSB. The model includes charge transfer kinetics at the SE/AM interface, diffusion and migration in the SE, and diffusion in the AM in the reconstructed 3D morphology of the three-phase electrode. The model is then employed to investigate the effect of compression on the ASSB behavior. In this way, the model is simulated for two different reconstructed geometries, obtained from electrodes fabricated under two different pressing pressures. This paper is structured in the following fashion: first, the electrode fabrication, synchrotron transmission X-ray microscopy (TXM) imaging techniques, and three-phase electrode reconstruction are discussed. The ASSB was processed and reconstructed by the Avizo^{TM} software package. Then, the modeling steps, morphological analysis, governing equations, and geometry selection are presented. The 3D modeling framework is implemented in Comsol Multiphysics 5.4. Finally, the simulation results are shown and discussed with concluding remarks.

4.2 Experimental

4.2.1 Material Synthesis and Electrode Fabrication

$Li_{1.3}Ti_{1.7}Al0.3(PO_4)_3$ (LTAP) was synthesized using aluminum oxide (Al_2O_3), titanium dioxide (TiO_2), lithium carbonate (Li_2CO_3), and ammonium dihydrogen phosphate ($(NH_4)_2H_2PO_4$). The solid mixture was ground and heated, then ball milled for 6 hours, reheated for 2 hours, and again ball milled for 12 hours to obtain the final LTAP powder. The all-solid-state electrode is fabricated using $Li(Ni_{1/3}Mn_{1/3}Co_{1/3})O_2$ (NMC) as the AM, Super-P carbon as the electron conductor, and LTAP as the SE with a mass ratio of 47:6:47 (wt %). Then, the electrode was pressed under two different pressing pressures (700 psi and 1300 psi) to modify the porosity and interfacial contact of the SE and AM [22, 95].

4.2.2 TXM Tomography

TXM within the Advanced Photon Source (APS) facility at Argonne National Laboratory was employed to obtain the morphological data of the three-phase electrode. A 8 keV beam was utilized to capture the images by rotating the sample for 180º with 2 s exposure time at each rotational step increment (0.25º). A total of 1000 virtual 2D slices were reconstructed. The 3D reconstructed volume was $700 \times 700 \times 1000$ voxels with $58.2 \times 58.2 \times 58.2$ nm^3 voxels resolution. The electrodes were fabricated and imaged at two pressing pressures, where external pressing pressure directly affects the physical properties of the electrode. Figure 4-1a-c shows the representative 2D slice images of the electrode fabricated under 700 psi and 1300 psi pressure, respectively. The white domain represents the AM, the gray is the SE and the black domain is the void space. Avizo™ was used for the segmentation of AM, SE, void spaces, and reconstruction of the three-phase electrode. Firstly, to reduce the noise of images, a median filter was applied. This filter is an effective way to remove impulse noises. Then, a de-blur filter was used to increase the contrast between phases. Segmentation with two thresholds, one separating the pore and SE phases and the other separating the AM and SE causes the formation of a thin layer of SE at the SE/AM interface. This very thin layer of SE is due to the grayscale gradient and is not realistic. Therefore, a dilation algorithm was used to replace the SE thin layer with the extension of the AM which has less than 5 pixels thickness and causes negligible error owing to the comparatively large size of the AM particles. The same thresholds were used for both pressing pressures. Finally, the 3D morphologies of the three-phase electrode were reconstructed after dilation. Figure 4-1e-g represents the AM phase, SE, and void space resulting from 700 psi pressure and Figure 4-1h-j represents the same phases after 1300 psi pressure. The super-P carbon volume fraction is included in the void phase. Figure 4-1 shows that as the pressing pressure increases, the volume fraction of the AM and SE is increased while the fraction of void space is decreased. Later, the effect of external

pressing pressure on the electrode physical properties and void space volume fraction will be thoroughly discussed.

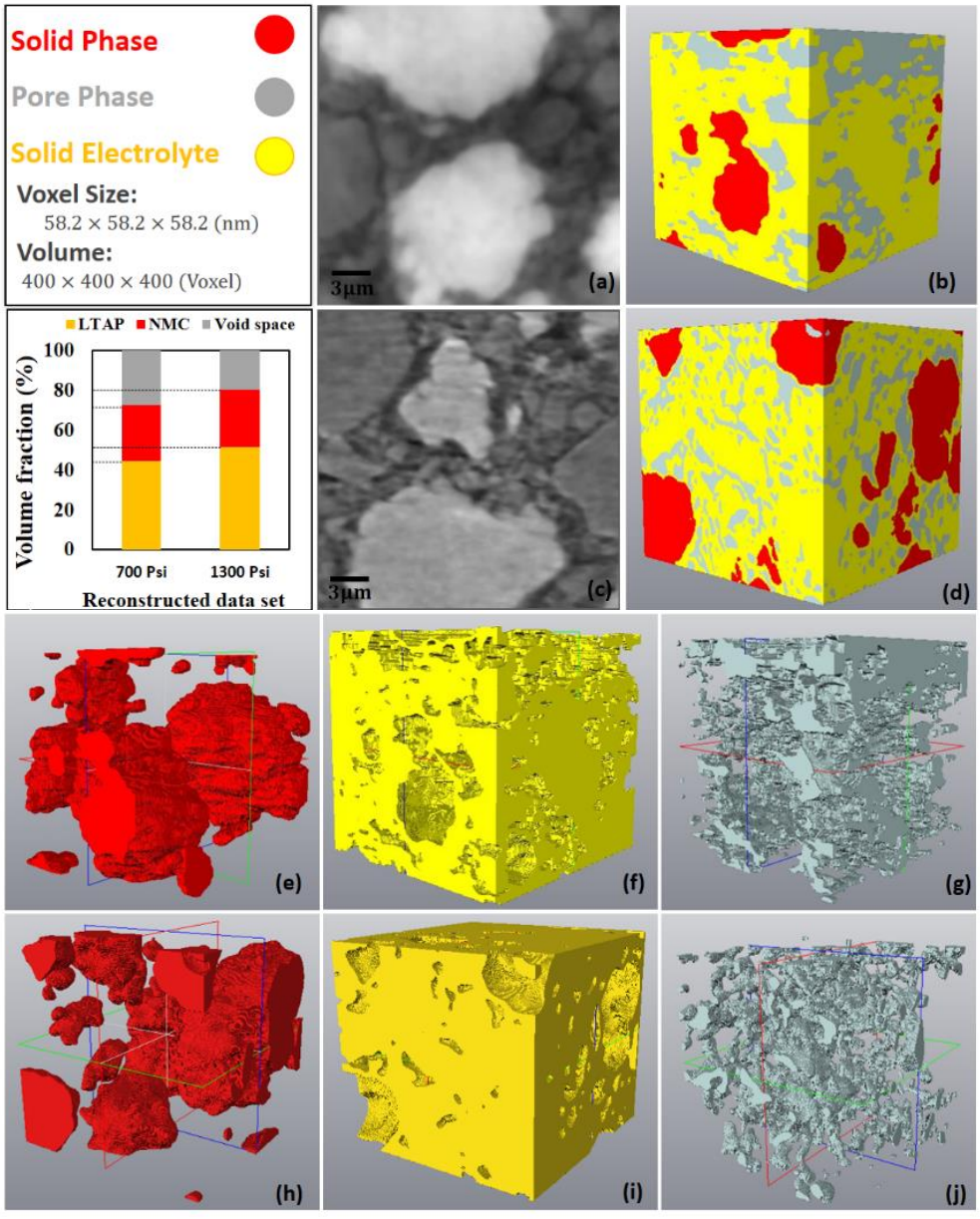

Figure 4-1 2D CT images of the electrode at two pressing pressures, (a) 700 psi, and (c) 1300 psi. 3D reconstructed morphology of the electrode at two pressing pressures, (b) 700 psi, and (d) 1300 psi. (e) AM, (f) SE, and (g) void space at 700 psi. (h) AM, (i) SE, and (j) void space at 1300 psi.

4.3 Modeling

4.3.1 Morphological and Transport Properties

Dd3D reconstructed microstructures of the three-phase electrode at two pressing pressures were analyzed to obtain its physical properties including electrode porosity, ε, volume-specific surface area, a, and directional tortuosity, τ. Tortuosity is defined as the free-space transport decrease caused by the electrode geometry and complex ion pathway. The transport problem has a direct analytical solution for simple geometries, or finite element/finite difference methods are used for complex geometries [96]. Tortuosity is defined as:

$$\boldsymbol{\tau = {\varepsilon\sigma}/{\sigma_{eff}}}, \quad (4\text{-}1)$$

where σ is the bulk ionic conductivity in the SE and σ_{eff} is the effective ionic conductivity. To obtain directional tortuosity, a FEM simulation of potential distribution, φ, using Laplace equation is performed on the SE domain:

$$\boldsymbol{\nabla.(\nabla\varphi) = 0}. \quad (4\text{-}2)$$

To obtain the directional tortuosity of the SE for electrodes fabricated under two pressures, and the potential of two parallel faces (inlet/outlet) is set to 0 and 1 and the rest of the faces are set to zero flux. Then, J, the areal flux at the inlet/outlet can be calculated based on integration over the inlet/outlet boundary (S) by:

$$\mathbf{J} = \int_S \boldsymbol{\sigma \frac{\partial \varphi}{\partial x_i} ds}, \quad (4\text{-}3)$$

and σ_{eff} is calculated by:

$$\boldsymbol{\sigma_{eff} = \frac{J}{A}\frac{L}{\Delta\varphi}}, \quad (4\text{-}4)$$

where A is the perpendicular cross-section area, L is the distance between inlet and outlet, and $\Delta\varphi$ is the potential difference, which is set to 1. If we substitute Eq. (3) and (4) into (1), the directional tortuosity can be calculated by:

$$\boldsymbol{\tau_i} = \frac{\boldsymbol{\varepsilon}\, \boldsymbol{A}}{\boldsymbol{L} \int_S \frac{\partial \boldsymbol{\varphi}}{\partial \boldsymbol{x_i}}}. \quad (4\text{-}5)$$

Eq. (5) shows that directional tortuosity is not a function of the domain ionic conductivity. The Bruggeman correlation is widely used in various fields [96] to estimate the tortuosity of porous media; it estimates τ as a function of porosity [97] by:

$$\boldsymbol{\tau} = \boldsymbol{\varepsilon}^{-\mathbf{0.5}}. \quad (4\text{-}6)$$

This correlation is based on solving the diffusive transport problem by considering either spheres or cylinders as transport obstructions. However, the accuracy of the Brugemann relation has been questioned for complex microstructures [96]. To be able to compare the directional tortuosities obtained from the reconstructed geometries by the Brugemann tortuosity, the characteristic tortuosity is suggested based on directional tortuosities by [98]:

$$\boldsymbol{\tau_c} = \mathbf{3}[\boldsymbol{\tau_x^{-1}} + \boldsymbol{\tau_y^{-1}} + \boldsymbol{\tau_z^{-1}}]^{-\mathbf{1}}, \quad (4\text{-}7)$$

where τ_x, τ_y, τ_z are directional tortuosities obtained by Eq. (5).

4.3.2 Governing Equations

The model governing equations include the charge transfer kinetics at the SE/AM interface, diffusion and migration of ions in the SE, and diffusion of ions in the AM. The equations consist of five unknown variables c_{Li}, c_{Li^+}, c_{n^-}, φ_s, and φ_{SE} which represent lithium concentration in the AM, lithium-ion concentration in the SE, negative charge concentration in the SE, AM potential, and SE potential, respectively; these are determined by solving mass and charge transport equations in the AM and SE

domains and considering the electro-neutrality condition in the SE (Figure 4-2). The equations are implemented on the three-phase reconstructed structure of the ASSB to obtain the electrochemical property distributions in the real microstructure as well as the voltage profiles. As mentioned previously, in ASSBs the SE facilitates ion conduction. The ionic conductivity of the SE is generally several orders of magnitude lower than common liquid electrolytes [99]. Therefore, it is assumed that all electrochemical reactions occur at the SE/AM interface [86]. Fick's mass transport law is used to describe the lithium diffusion in the AM domain as [100, 101]:

$$\boldsymbol{J_{Li} = -D_{Li}\nabla c_{Li}}, \quad (4\text{-}8)$$

$$\boldsymbol{\frac{\partial c_{Li}}{\partial t} = -\nabla . J_{Li}}, \quad (4\text{-}9)$$

where D_{Li}, J_{Li}, c_{Li} are the diffusion coefficient of lithium, lithium flux, and lithium concentration in AM, respectively. On the SE/AM interface, the reaction is described using Butler-Volmer kinetics:

$$\boldsymbol{i_{pos} = i_{0,pos}(e^{\frac{\alpha_{pos}F\eta}{RT}} - e^{-\frac{(1-\alpha_{pos})F\eta}{RT}})}, \quad (4\text{-}10)$$

$$\boldsymbol{i_{0,pos} = Fk_{pos}\left(\frac{(c_{Li,max}-c_{Li})c_{Li^+}}{(c_{Li,max}-c_{Li})c_{Li^+,0}}\right)^{\alpha_{pos}}\left(\frac{c_{Li}-c_{Li,min}}{c_{Li,max}-c_{Li,min}}\right)^{1-\alpha_{pos}}}, \quad (4\text{-}11)$$

where $c_{Li,max}$ and $c_{Li,min}$ are the maximum and minimum of the lithium concentration in AM, and i_{pos}, $i_{0,pos}$, k_{pos}, α_{pos}, and F are the current density, exchange current density, the reaction rate constant, apparent transfer coefficient, and Faraday's constant, respectively. The AM potential can be calculated by:

$$\boldsymbol{i_{pos} = -\sigma_{pos}\nabla\varphi_s}, \quad (4\text{-}12)$$

where E_{eq} is the open circuit potential, and φ_{SE}, φ_s, and σ_{pos} are the SE potential, AM potential, and conductivity of solid active material, respectively. In the SE, the chemical reaction is:

$$\boldsymbol{Li^0 \leftrightarrow Li^+ + n^-}, \quad (4\text{-}13)$$

where bonded lithium (Li^0) is transferred to a lithium-ion and releases a negative charge [86]. k_d is defined as the dissociation rate of this reaction and the inverse reaction rate is defined as k_r. Therefore, the overall reaction is [86]:

$$\boldsymbol{r_d = k_d c_{Li^0} - k_r c_{Li} c_{n^-}}, \quad (4\text{-}14)$$

$$\boldsymbol{c_{Li^+}^{eq} = c_{n^-}^{eq} = \delta c_0}, \quad (4\text{-}15)$$

where δ is the fraction of the total dissociated lithium at equilibrium and $c_{Li^+}^{eq}$, $c_{n^-}^{eq}$, and c_0 are the lithium-ion concentration at equilibrium, negative charge concentration at equilibrium, and total lithium concentration in the SE, respectively. Transport of lithium-ions and negative charges in the SE are modeled by the Nernst-Planck equation [88]:

$$\boldsymbol{\frac{\partial c_i}{\partial t} + \nabla . J_i = r_d}, \quad (4\text{-}16)$$

$$\boldsymbol{J_i = -D_i \nabla c_i + \frac{z_i F}{RT} D c_i \nabla \varphi_{SE}}, \quad (4\text{-}17)$$

where z_i and D_i are the species' charge and diffusivity, respectively. The electro-neutrality condition implies that, at any time in the SE, $c_{Li^+} = c_{n^-}$. Faraday's law is used to couple the flux at the interface of the SE and AM as:

$$\boldsymbol{J_n = \frac{i_{pos}}{F}}, \quad (4\text{-}18)$$

where n is the normal unit vector to the interface and J_n is the lithium mass transport flux at the SE/AM interface. At all SE cube sides, $\nabla\varphi = 0 \; and \; \nabla c = 0$. Each of the transport processes has a contribution to the total overpotential [102]. The concentration overpotential in AM is [86]:

$$\boldsymbol{\eta_c = \varphi_{pos} - \varphi_{pos}^{eq}}, \quad (4\text{-}19)$$

where φ_{pos} and φ_{pos}^{eq} are the AM potential and potential at equilibrium. Kinetic overpotential at the SE/AM and Ohmic overpotential in SE are derived by [102]:

$$\eta_k = \frac{1}{A_{interface}} \int \eta_{Butler-Volmer}\, dA_{interface}, \quad (4\text{-}20)$$

$$\eta_\tau = \Delta\varphi_{SE}, \quad (4\text{-}21)$$

where $A_{interface}$ is the SE and AM interface area and φ_{SE} is the SE potential.

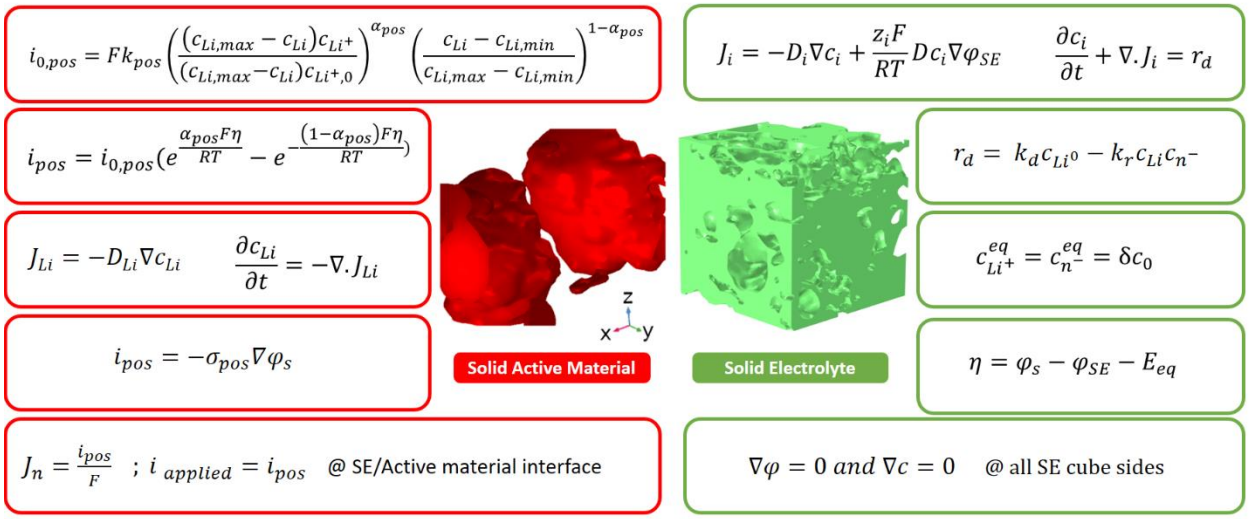

Figure 4-2 Modeling framework

4.3.3 RVE Selection

It should be noted that using the whole 3D reconstructed electrode morphology as the model geometry would be computationally expensive. One way to address this issue is to use a representative volume element (RVE) instead of the whole electrode structure. RVE is a sub-volume of the whole electrode that has the same measured property values compared to the whole electrode with negligible error [103].

The SE, AM, and pore volume fractions and volume specific surface area of the AM are calculated to figure out the size of RVE. The three-phase volume fractions for the whole domains with seven different volume sizes are presented in Table 4-1 for two pressing pressures. Table 4-1 shows that the SE, AM, and pore volume fractions for an RVE size of 7097 μm^3 and larger are similar to the whole electrode (within 2% error). Accordingly, the smallest suitable RVE size would be 7097 μm^3; however, to minimize the error of selecting a specific region of the geometry, the electrochemical performance

simulation and morphological analysis were modeled on a sub-volume geometry with the dimension of $400 \times 400 \times 400$ Voxels (12617 μm^3) (Figure 4-3), i.e., all represented 3D morphologies in the following figures have $400 \times 400 \times 400$ voxels; current density direction and current collector illustrated in Figure 4-3c. The simulations were conducted on CMC compute cad cluster with 8 nodes delivering 8.6 TFLOPS. The running time for each simulation varies from 2 to 4 hours.

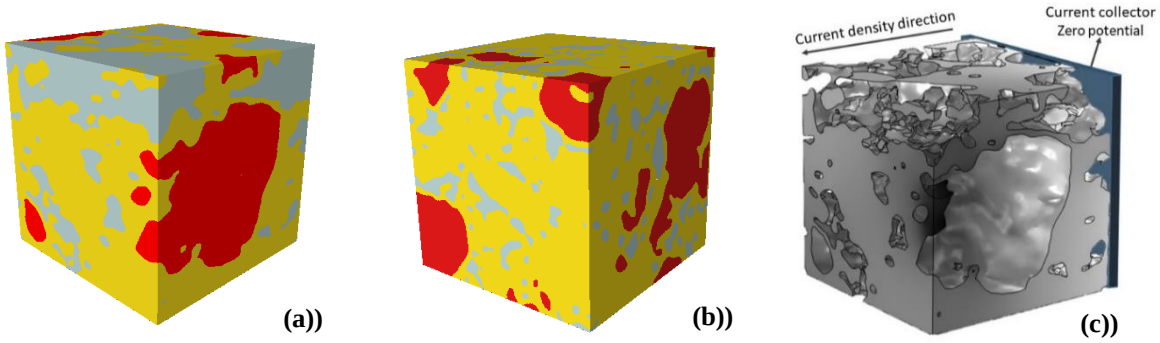

Figure 4-3 3D reconstructed RVEs of the ASSB at (a) 700 psi, and (b) 1300 psi pressing pressure; yellow, red, and grey colors represent the SE, AM, and void space, respectively, and (c) current collector and current density direction.

Table 4-1 The Volume fraction of different phases of the reconstructed 3D geometry at two pressing pressures.

Pressing pressure 700 psi

Total Volume (μm^3)	19714	15968	12617	9660	7097	4929	3154
Volume specific surface area (1/µm)	0.522	0.531	0.554	0.562	0.583	0.593	0.612
Solid Active material (%)	28.1	27.6	27.9	29.3	29.2	27.1	27.2
Solid Electrolyte (%)	44.9	45.1	44.5	43.2	43.3	57.6	60.5
Pore (%)	27.0	27.3	27.6	27.5	27.5	15.3	12.3

Pressing pressure 1300 psi

Total Volume (μm^3)	19714	15968	12617	9660	7097	4929	3154
Volume specific surface area (1/µm)	0.617	0.622	0.631	0.642	0.648	0.652	0.664
Solid Active material (%)	28.1	27.8	28.7	27.7	28.2	27.4	19.3

Pressing pressure 700 psi							
Solid Electrolyte (%)	52.6	53.2	51.5	53.8	53.1	55.1	60.6
Pore (%)	19.3	20.0	19.8	18.5	18.7	17.6	20.1

4.4 Results and Discussion

To investigate the heterogeneity and isotropy of the electrode's microstructure, tortuosities of the SE domain were estimated and compared in different directions using the method presented in the modeling section. The directional, characteristic, and Bruggeman tortuosities are presented in Table 4-2. The characteristic tortuosity, τ_c is obtained using Equation (4-7) and the Bruggeman tortuosity is calculated with Equation (4-6) where ε is equal to the SE volume fraction. The Bruggeman tortuosity, obtained based on a geometry of equally sized spheres, is slightly lower than the characteristic tortuosity due to its neglecting of the heterogeneous structure. Furthermore, lower tortuosity of the electrode with higher pressing pressure verifies that higher pressing pressure leads to less void space and consequently less ionic transport resistance through the SE; i.e., in this case, higher pressing pressure causes 26.8% less void space in the electrode and consequently 11.1% less tortuosity and 36.9% higher volume specific surface area.

Table 4-2 Directional tortuosities based on 3D reconstructed geometry and implementing heat transport analogy.

	700 psi	1300 psi
In-plane directional tortuosity, τ_x	1.53	1.52
In-plane directional tortuosity, τ_y	1.54	1.40
Through-plane directional tortuosity, τ_z	1.8	1.38
Characteristic tortuosity, τ_c	1.61	1.43
Bruggeman tortuosity, τ_B	1.50	1.39

Although 1D models [86, 87] can predict the voltage-capacity performance by considering macroscale geometry, they fail to describe the variation of physical and electrochemical properties

inside the heterogeneous electrode structure. To obtain the spatial distribution of physical and electrochemical properties inside the electrode microstructure including lithium concentration, current density, and potential, the presented model in the modeling section is simulated on the 3D reconstructed electrode structures (Figure 4-3). Moreover, to investigate the effect of the external pressing pressure on the physical and electrochemical phenomena, the electrode structures fabricated under two pressures of 700 and 1300 psi are considered.

To validate the accuracy of the developed model, the simulation results are compared against the experimental cycling performance of an ASSB with LTAP as SE and $LiMn_2O_4$ as AM for which experimental performance data was available [95]. Figure 4-4a shows the modeling performance against the experimental data for galvanostatic charging at 0.1 C current rate. The model/experiment comparison shows relatively good agreement. Table 4-3 shows the parameters used to simulate the modeling result in Figure 4-4. D_{Li} , the diffusion coefficient for lithium in the AM, D_{Li^+}, the diffusion coefficient for lithium-ions in the SE, and D_{n^-}, the diffusion coefficient for n− in the SE are considered the model adjustable parameters and determined to be $1.76 \times 10^{-13}\ m^2 s^{-1}$, $0.9 \times 10^{-13}\ m^2 s^{-1}$, and $5.1 \times 10^{-13}\ m^2 s^{-1}$, respectively, by comparing the simulation results against the experimental data. The considered diffusion coefficient values in the presented model are in the range of reported values in literature (10^{-16}-10^{-12} m^2 s^{-1}) [99, 104, 105]. Additionally, to verify the validity of the developed 3D model, the discharge performance is compared with the available 1D model [86] using the same model parameters presented in Table 4-3. In order to scale the volumetric current source term for the 1D model, $i_{1D} = \frac{a}{a_0} i_{3D}$, where a is the volume specific area obtained by reconstructed morphology (Table 4-1) and a_0 is the volume specific area for the 1D model. At various current rates, 3D and 1D models have almost identical voltage profiles; however, the 3D model predicts slightly higher ohmic resistance due to included electrode microstructure in the model geometry (Figure 4-4b).

Table 4-3 Model Parameters

Parameter	Unit	Estimated Value	Description
a_0	$mol\ m^{-3}$	6.01×10^4 [86]	Total activity of Li atoms in SE matrix
k_r	$m^3 mol^{-1} s^{-1}$	0.9×10^{-8} [86]	Lithium-ion recombination reaction rate
δ	-	0.18 [86]	Fraction of free lithium-ion in equilibrium
D_{Li^+}	$m^2 s^{-1}$	0.9×10^{-13}	Diffusion coefficient for lithium-ion in the SE (LTAP)
D_{Li}	$m^2 s^{-1}$	1.76×10^{-13}	Diffusion coefficient for lithium in AM (NMC)
D_{n^-}	$m^2 s^{-1}$	5.1×10^{-13}	Diffusion coefficient for n^- in the electrolyte
a_{pos}^{max}	$mol\ m^{-3}$	2.33×10^4 [86]	Maximum activity of the lithium in the positive electrode
α_{pos}	-	0.6 [86]	Charge transfer coefficient in the positive electrode
k_{poa}	$mol\ m^{-2} s^{-1}$	5.1×10^{-6} [86]	Rate constant charge transfer positive electrode
L	µm	14.33	Thickness of the SE (for 1D model)
M	µm	8.95	Thickness of the AM (for 1D model)

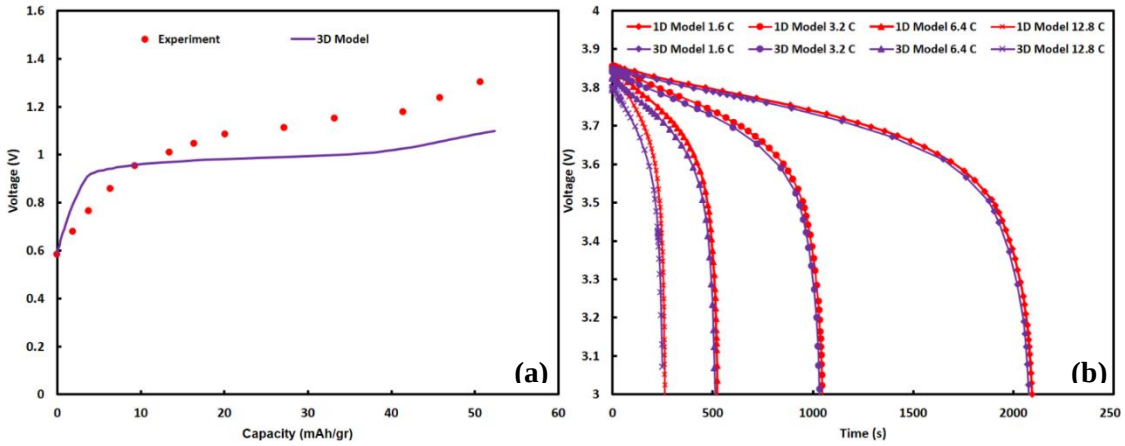

Figure 4-4 (a) Comparison of the modeling (line) and experimental data set (dots), and (b) comparison of the 3D developed model with 1D Model based on ref. [13].

After validating the developed model, the model is employed to predict the galvanostatic discharge performance of the ASSB with NMC as the active material. To demonstrate the effect of different pressing pressures during electrode fabrication on the ASSB behaviors, the simulation results are conducted on the reconstructed RVEs with two pressing pressures, (Figure 4-3). Applying external pressing pressure causes lower void space volume fraction and leads to more homogenous distribution of electrochemical properties. Although the high external pressure would increase the contact area between the SE and active materials by decreasing the void space fraction, it can damage the SE due to its brittle nature [106]. However, the capacity of the cell with different pressing pressures is almost the same at various C-rates; Figure 4-5a shows that there is a higher ohmic loss at lower pressing pressure that could be attributed to poor SE/AM contact and higher interfacial resistance. Figure 4-5b illustrates the contribution of the various overpotential components during discharging at 3.2 C and 12.8 C for the electrode with a 700 psi pressing pressure. Remarkably, concentration overpotential within the AM has the largest contribution at the end of discharge due to the steep concentration gradient of lithium. During the discharge, Ohmic overpotential in SE has a considerable contribution; whereas, imperfect SE/AM interface leads to a large kinetic overpotential at the beginning of the discharge process. On the other hand, at high discharge current rate (12.8 C), the kinetic overpotential contribution becomes larger, and ohmic overpotential contribution is less than 3.2 C discharge rate.

1D models are based on macro-sized geometries (a 1D line) and do not consider the effect of microstructure on the electrochemical property distribution [85, 86, 88]. However, these assumptions are not valid for real ASSB cells, which have an inhomogeneous microstructure with AM particles of

different sizes and shapes and random void space formations. Even though the 1D models can successfully predict the capacity performance, they fail to predict the physical and electrochemical property variations which may cause cell degradation [102, 107]. The key advantage of using reconstructed morphologies in this study is to visualize the heterogeneities inside the SE and AM which can contribute to electrode degradation. The presented study sheds light on the spatial distribution of electrochemical properties in ASSBs and specifically the effects of pressing pressure on the cell performance and physical and electrochemical behaviors of the cell.

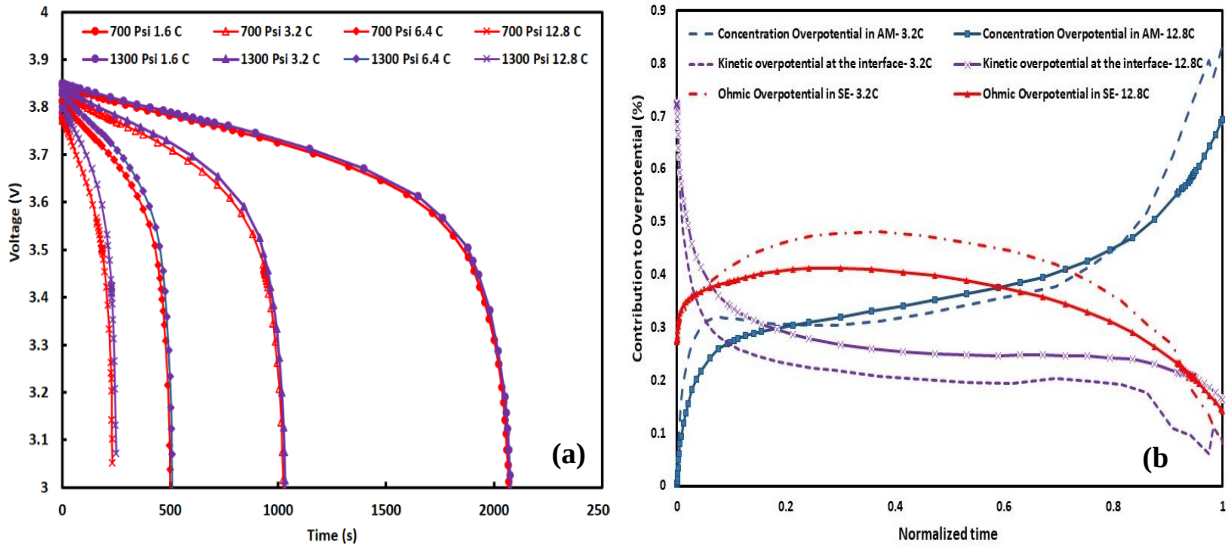

Figure 4-5 (a) Effect of external pressing pressure on the galvanostatic discharge performance of the ASSB at various current rates, and (b) overpotentials in the composite electrode under 700 psi pressing pressure at two current rates.

Figure 4-6a-c and d-f show the lithium distribution in the AM at various state of charges (SOCs) during galvanostatic discharge at 3.2 C for two pressing pressures of 700 and 1300 psi, respectively. During discharge, the average lithium concentration in the AM is higher at higher pressing pressure which verifies that increasing pressure facilitates lithium-ion transport inside the AM. Figure 4-6g-l presents lithium concentration histograms for two pressures; this demonstrates that higher pressure

leads to more uniform lithium distribution inside the AM. At 0.7 SOC for 700 psi pressing pressure, there is a wider range of lithium distribution inside the AM, with lithium concentrations in the range of 14200-16200 ($mol.m^{-3}$) at 700 psi compared to 14400-15400 ($mol.m^{-3}$) at 1300 psi (Figure 4-6g-l). In addition, Figure 4-6a-f shows that smaller particles have higher lithium concentrations due to their higher specific surface areas, comparable with previous heterogeneous study with liquid electrolyte [26, 100]. The dashed lines in Figure 4-6 histograms represent the concentration value of the homogenous Danilov 1D Model [86]. Since the homogenous model does not consider the microstructure of the electrode, it cannot predict the distribution range of lithium concentration; however, the homogenous model result is close to the average value of the lithium concentration simulated with this 3D model.

The lithium-ion distribution in the SE is presented in Figure 4-7. To show the lithium-ion gradient inside the SE, the lithium-ion distribution is illustrated on two cross-section planes. There are some specific points with higher lithium-ion concentration adjacent to the void spaces since void spaces block the lithium-ion path and cause non-uniform lithium-ion distribution (Figure 4-7a-f). A similar trend was reported in a previous ASSB microstructural study [108]. At lower pressing pressure of 700 psi, the electrode has 16% less SE and 28% more void space compared to the electrode at 1300 psi. This leads to a 56% larger range of lithium-ion distribution in the SE at 700 psi compared to 1300 psi. At 700 psi, the lithium-ions distribute in the range of 8000-15000 ($mol.m^{-3}$) compared to the range of 9500-13000 ($mol.m^{-3}$) at 1300 psi. This larger range of lithium-ion concentration at low pressing pressure may cause non-uniform expansion/contraction and consequently stress formation in the cell, which can cause cell performance degradation (Figure 4-7a-f g-l). The lithium-ion concentration based on the 1D model (dashed line) is almost constant over the discharge, while lithium-ion histograms of the 3D models illustrate the variation of lithium-ion concentration during discharge.

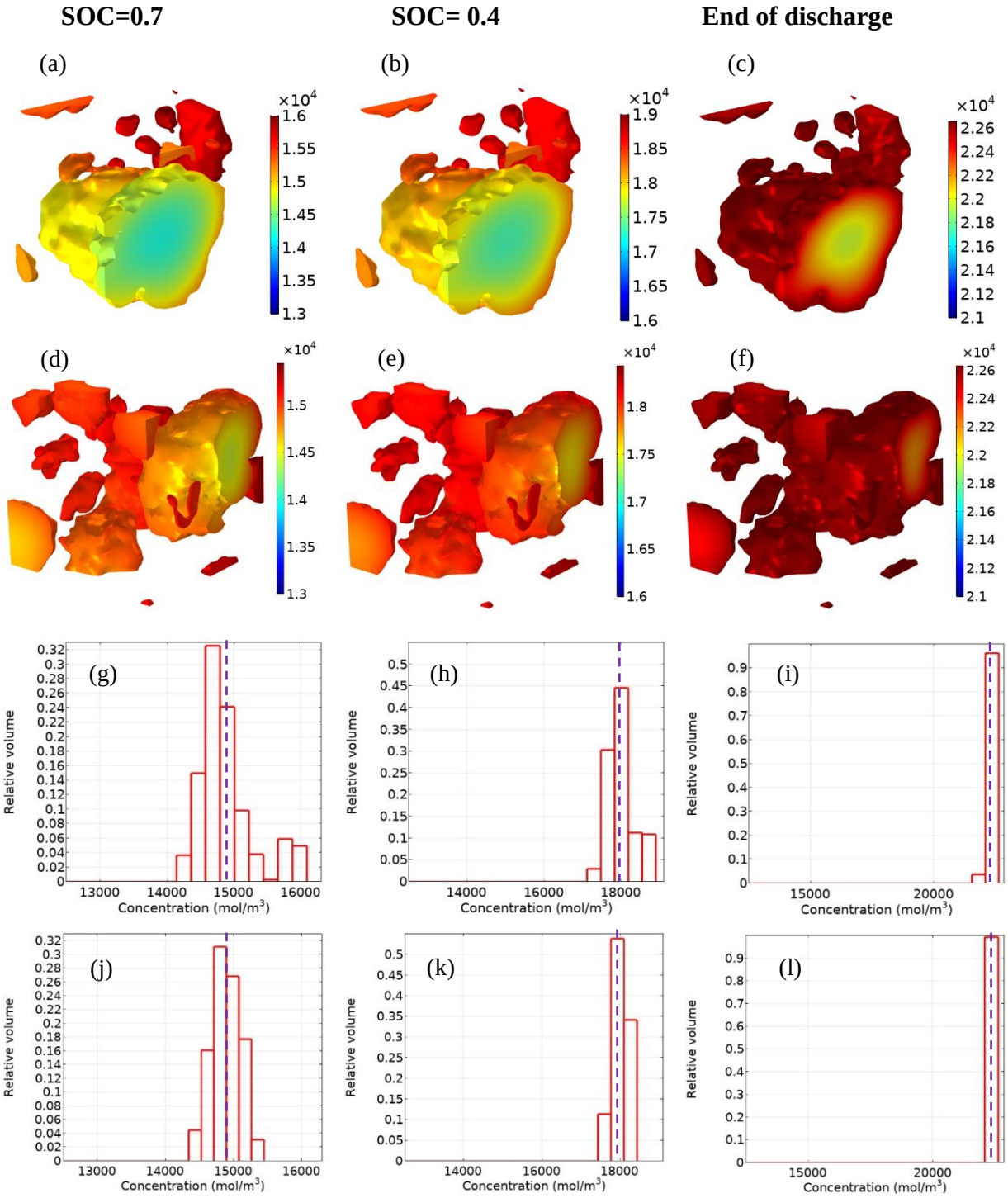

Figure 4-6 Lithium concentration in the AM phase with two pressing pressures: (a-c) 700 psi, (d-f) 1300 psi at 3.2C current rate, and various SOCs. Histogram representing the lithium concentration in the AM with two pressing pressures: (g-i) 700 psi, (j-l) 1300 psi

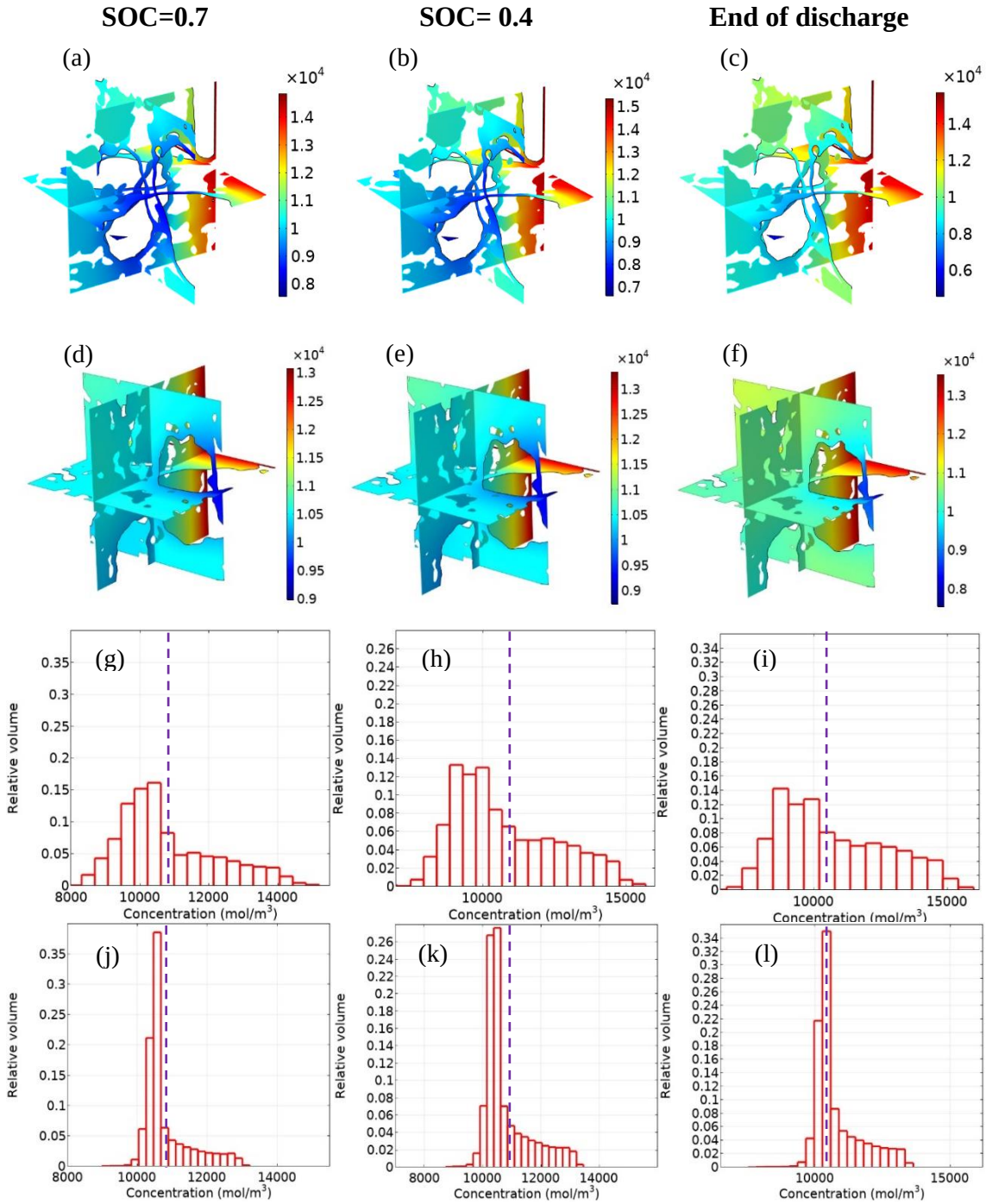

Figure 4-7 Lithium-ion concentration in the SE with two pressing pressures: (a-c) 700 psi, (d-f) 1300 psi at 3.2C current rate, and various SOCs. Histogram representing the lithium-ion concentration with SE two pressing pressures: (g-i) 700 psi, (j-l) 1300 psi during galvanostatic discharge (3.2C) at various SOCs. Dashed lines represent the 1D model

At higher current rates, structural heterogeneity has a stronger effect on the physical and electrochemical property distributions [28]. To investigate the effect of pressing pressure at high currents, the lithium concentration distribution in the AM and lithium-ion distribution in the SE at 12.8 C current rate are presented in Figures Figure 4-8 and Figure 4-9, respectively. Comparing Figure 4-6g with Figure 4-8g, it is noticeable that at the higher current rate the lithium distribution has a 240% wider range at the low pressing pressure where more void spaces and higher tortuosity cause non-uniform lithium distribution in the AM. Comparing lithium-ion distribution in the SE at 3.2 C (Figure 4-7) and 12.8 C (Figure 4-9), a lithium-ion concentration gradient is established along the lithium-ion transport direction and has a wider range at the higher current rates and lower pressing pressures. Additionally, at the high current rate, the lithium concentration range highly deviates from the 1D model results (dashed line) due to the complex microstructure of the electrode which is neglected in the 1D model.

As mentioned, interfacial resistance and specifically void spaces hinder the lithium-ion transport [108]. To further investigate this, the SE potential and current density distribution for the two electrodes fabricated under different pressures are presented in Figures Figure 4-10-13. Figure 4-10 shows that at 700 psi, the potential ranges from -40 mV to 0 mV at the end of discharge which is 2.5 times higher than the range of -16 mv to 0 mV at 1300 psi. As illustrated in Figure 4-11, with increasing current rate, the electrolyte voltage drop at the end of discharge ranges from -250 mV to 0 mV which is 6.25 times higher compared to the voltage drop at 3.2 C; however, at higher pressing pressure increasing the current rate has less effect on the SE voltage drop. In fact, the SE voltage drop is the main contribution to the ASSBs overpotential [88], and at high current rates, it has a more significant role in determining the overpotential distribution. Chemomechanical contraction of AM during delithiation leads to contact loss and higher interfacial resistance[109]. Additionally, volume changes during cycling may cause crack formation in SE which increase the tortuosity and lead to a capacity fade[110]; however, in the

presented model this effect is neglected and the aforementioned imperfect contact in the reconstructed morphologies is due to initial pore distribution in the composite electrode.

Figure 4-12 shows the distribution of current density at the SE/AM interface, where the complex microstructure of the electrode causes large current densities within ionic pathways with a small cross-sectional area perpendicular to the current direction. At high currents, the lithium-ion concentration differences in the SE and AM become larger which leads to a higher current density at the SE/AM interface. The current density has an inhomogenous distribution with a peak at the neck of a "sandglass" microstructure. Specifically, the current density has a wide range of distribution with several peak points with a high current density of 24 A m^{-2} which is almost 2 times the average current density (12.8 A m^{-2}). In the close-up view shown in Figure 4-13, all of these points are observed to be located near sandglass microstructures where there is a limitation on ion transport.

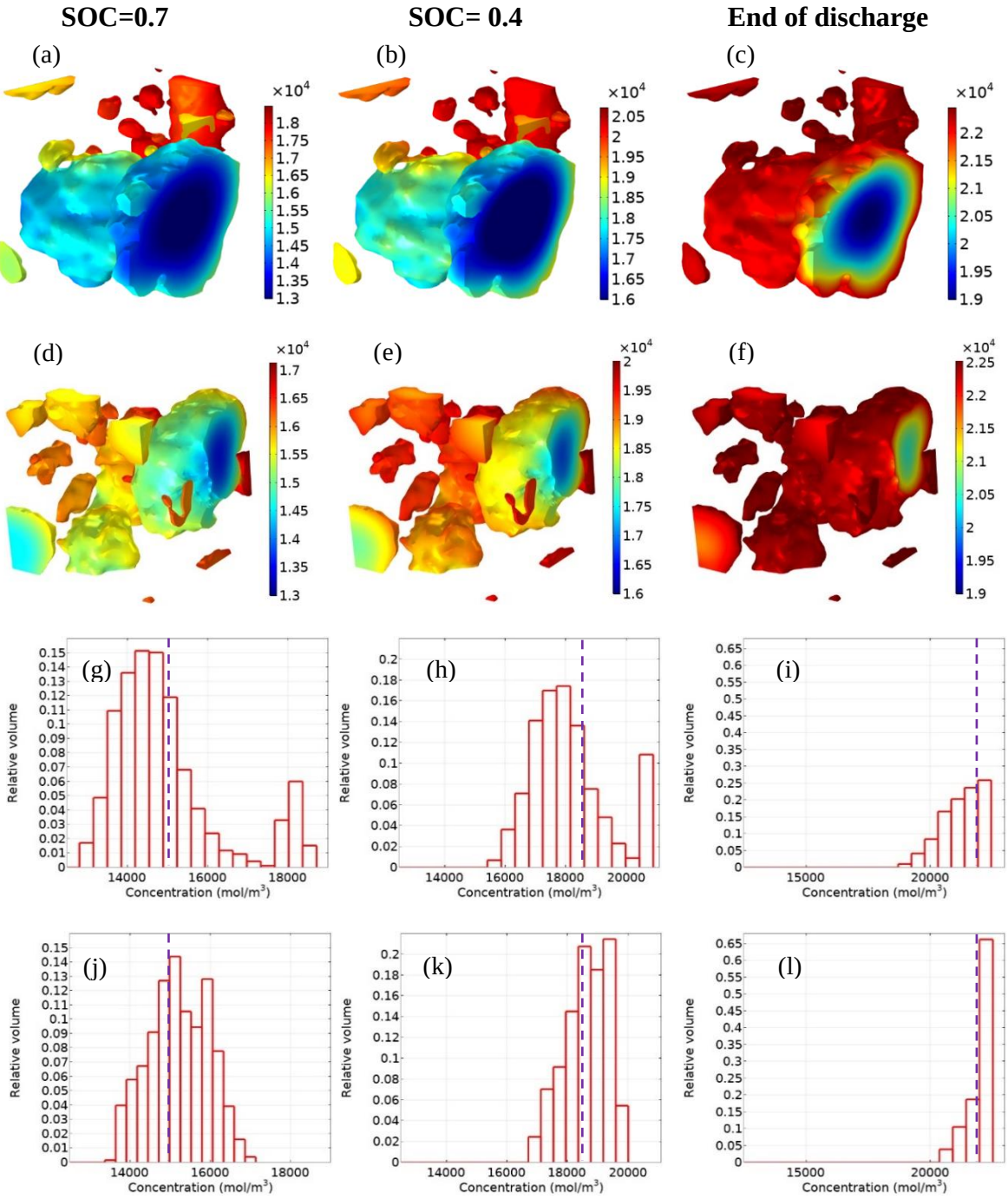

Figure 4-8 Lithium concentration in AM phase with two pressing pressures: (a-c) 700 psi, (d-f) 1300 psi at 12.8C current rate, and various SOCs. Histogram representing the lithium concentration in AM with two pressing pressures: (g-i) 700 psi, (j-l) 1300 psi during galvanostatic discharge (12.8C) at various SOCs. Dashed lines represent the 1D model values.

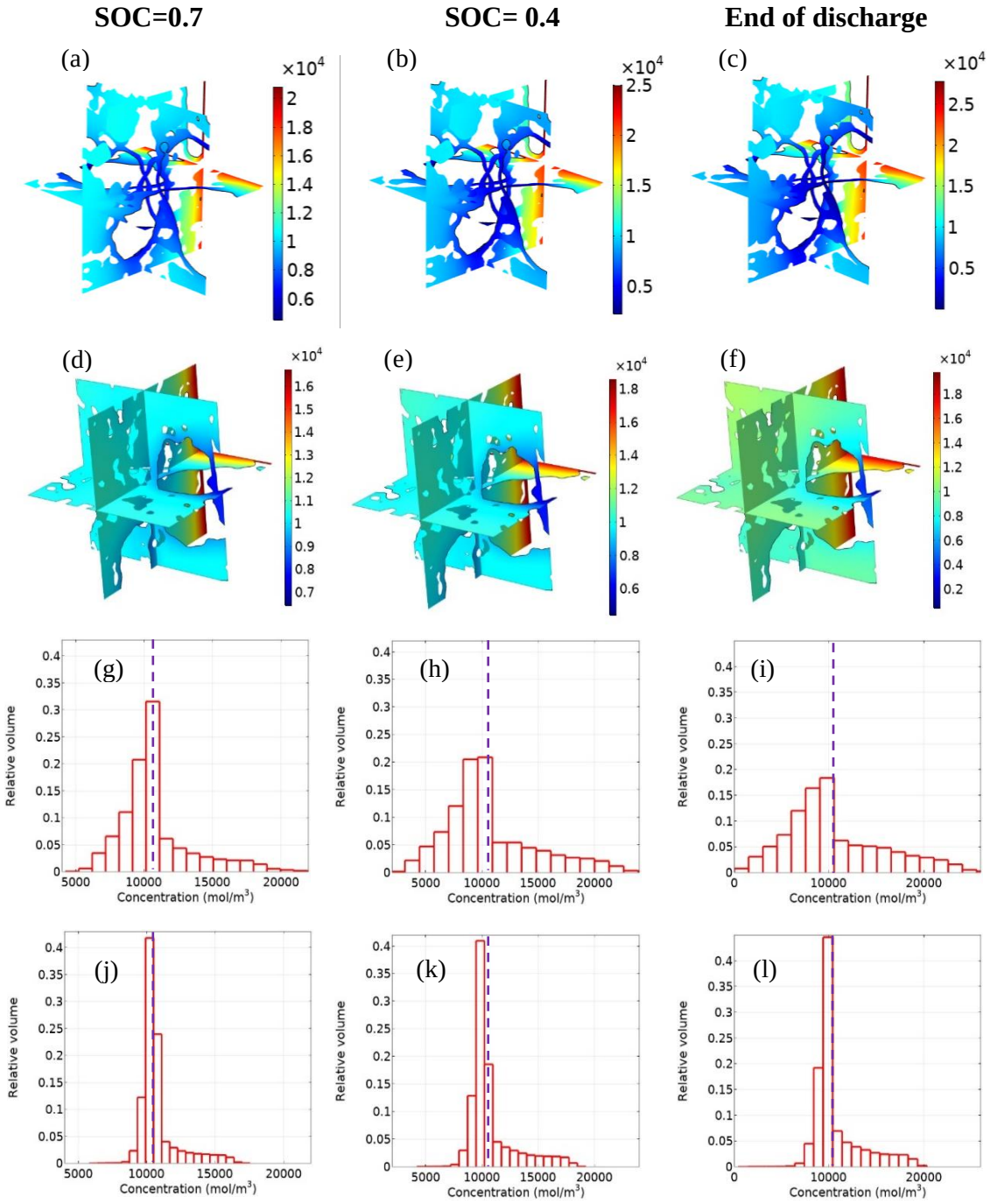

Figure 4-9 Lithium-ion concentration in SE with two pressing pressures: (a-c) 700 psi, (d-f) 1300 psi at 12.8 C current rate and various SOCs. Histogram representing the lithium-ion concentration in SE with two pressing pressures: (g-i) 700 psi, (j-l) 1300 psi during galvanostatic discharge (12.8 C) at various SOCs. Dashed lines represent the 1D model values.

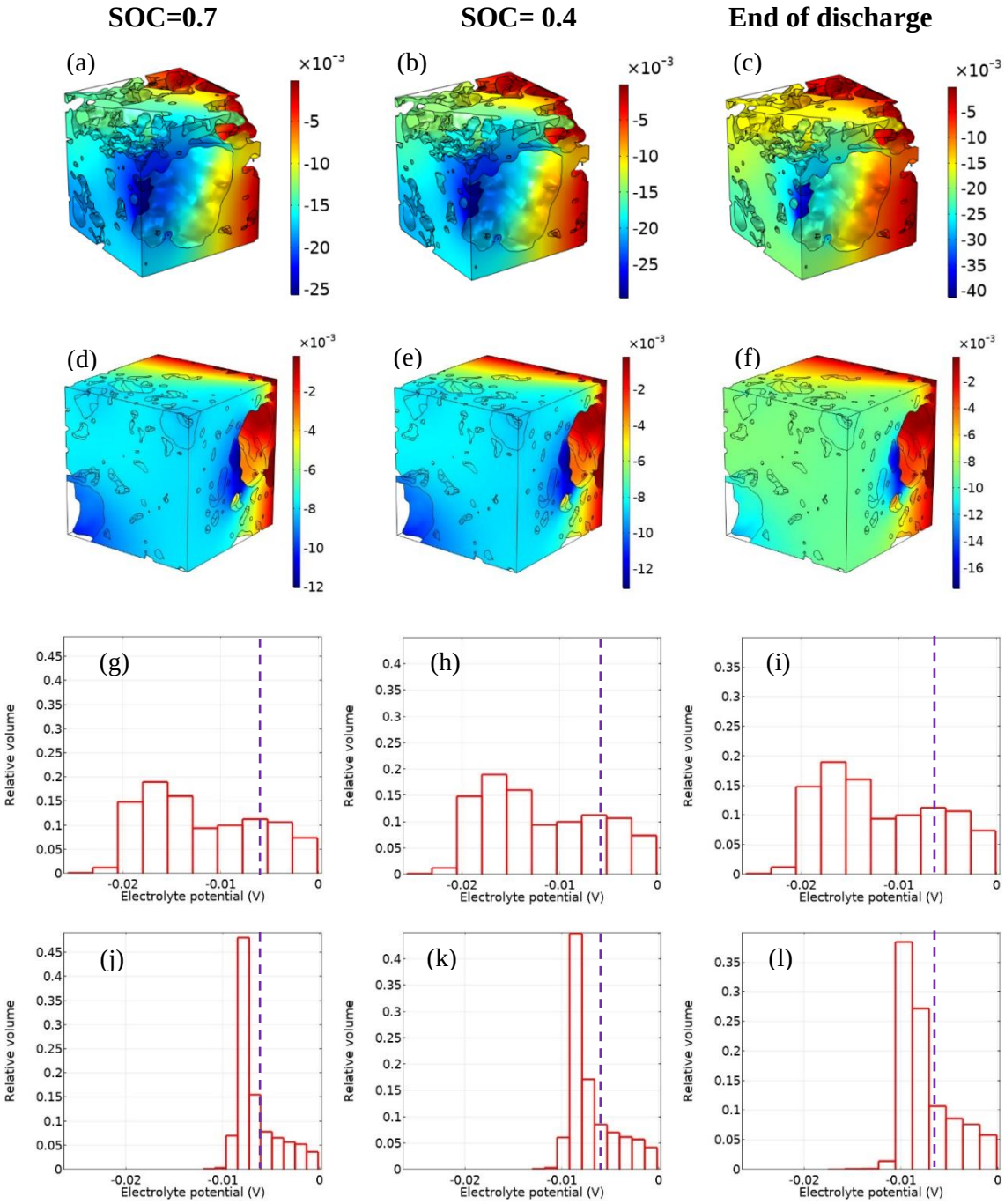

Figure 4-10 Potential in SE with two pressing pressures: (a-c) 700 psi, (d-f) 1300 psi at 3.2C current rate, and various SOCs. Histogram representing the SE potential at two pressing pressures: (g-i) 700 psi, (j-l) 1300 psi during galvanostatic discharge (3.2C) at various SOCs. Dashed lines represent the 1D model values.

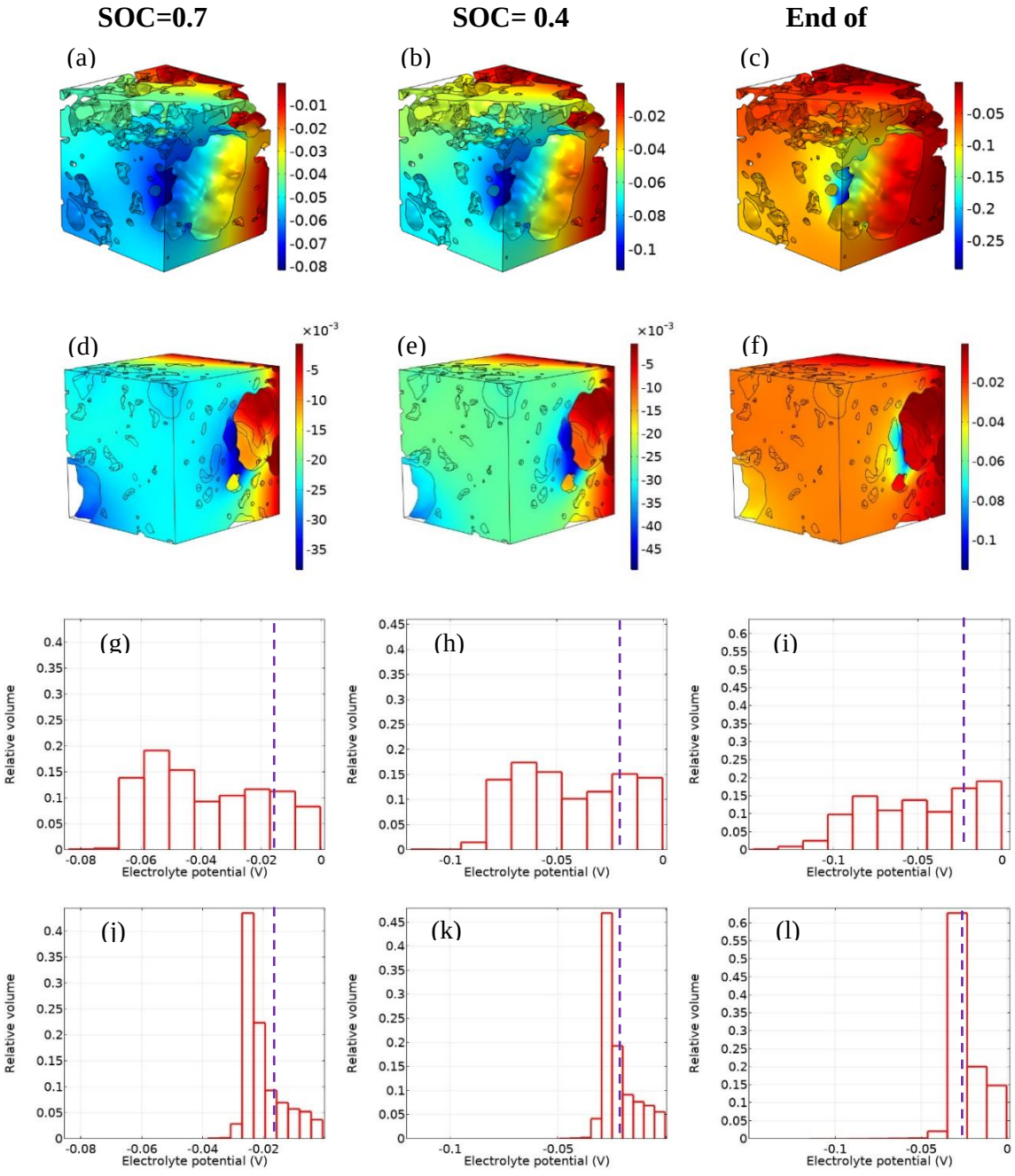

Figure 4-11 Potential in the SE with two pressing pressures: (a-c) 700 psi, (d-f) 1300 psi at 12.8 C current rate, and various SOCs. Histogram representing the SE potential at two pressing pressures: (g-i) 700 psi, (j-l) 1300 psi during galvanostatic discharge (12.8 C) at various SOCs. Dashed lines represent the 1D model values.

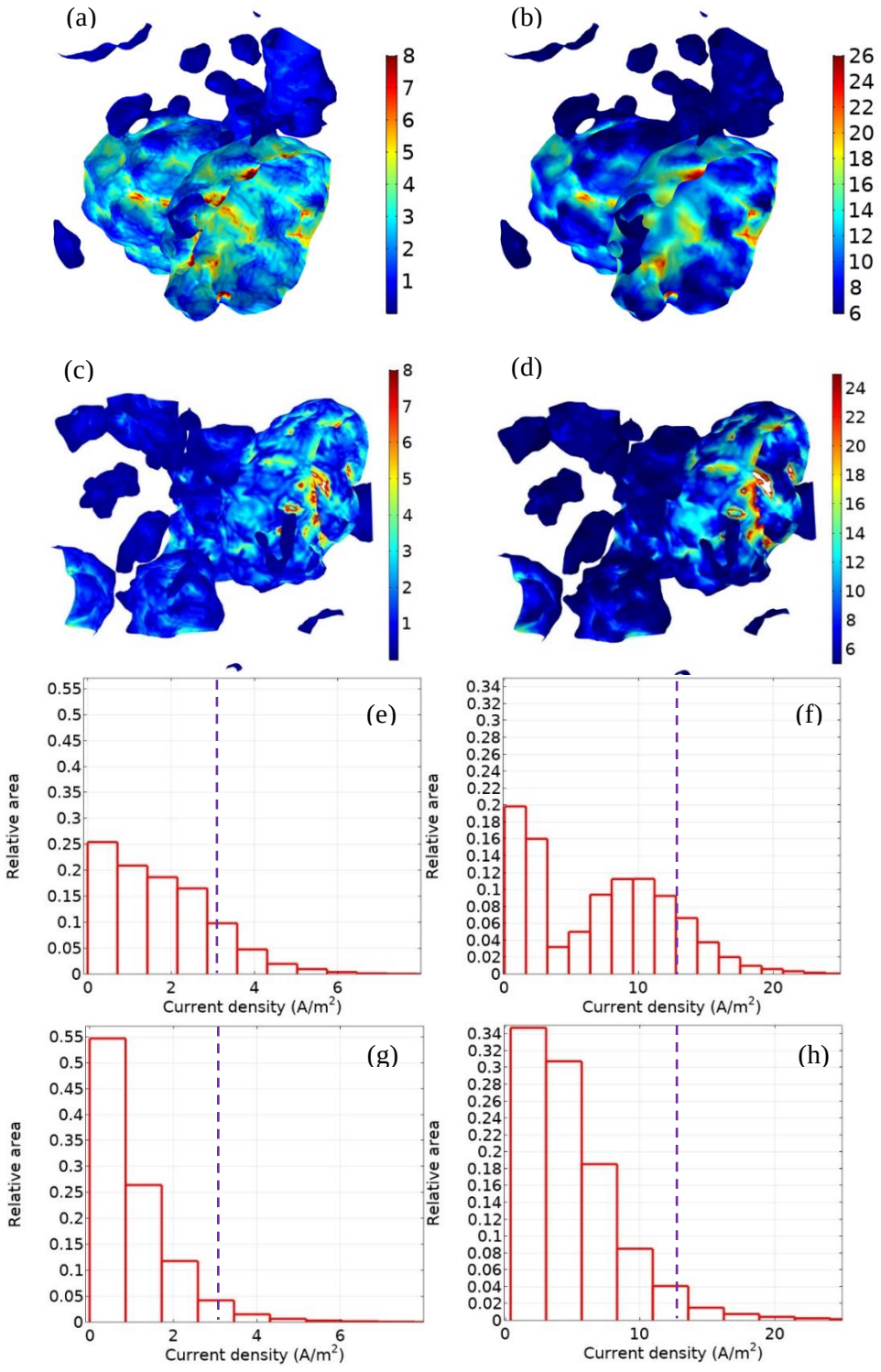

Figure 4-12 Current density at SE/AM interface at (a) 700 psi pressing pressure, and the end of discharge, at 3.2 C current rate, (b) 700 psi pressing pressure, and the end of discharge, at 12.8

C current rate, (c) 1300 psi pressing pressure, and the end of discharge, at 3.2 C current rate, (d) 1300 psi pressing pressure, and the end of discharge, at 12.8 C current rate. (e-h) Histogram representing the SE/AM interface current density at (a-d) conditions, respectively. Dashed lines represent the 1D model values.

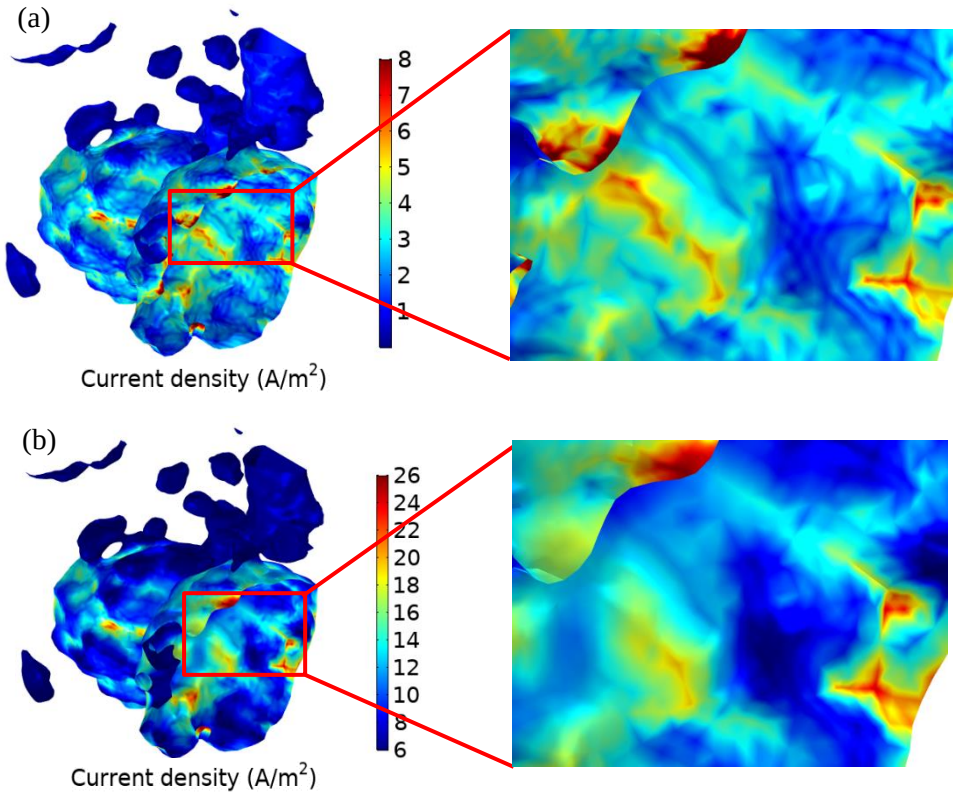

Figure 4-13 A close-up view of the current density distribution at the SE/AM interface at 700 psi pressing pressure, (a) 3.2 C current rate, and (b) 12.8 C current rate. The highest current density occurs near void spaces.

4.5 Conclusions

In this study, the first 3D multi-physics simulation of ASSBs based on reconstructed X-ray CT images was accomplished. The imaging was conducted using 58.2 nm resolution synchrotron TXM for two electrodes with different external pressing pressures to investigate the effects of compression on the physical and electrochemical property behaviors. The SE's resistance to ion transport was quantified by estimating the SE tortuosity using a heat transport analogy. The simulation showed that higher pressing pressure causes 26.8% less void space in the electrode and consequently 11.1% less tortuosity and 36.9% higher volume specific surface area. Void spaces block the lithium-ion pathways in the SE and cause resistance in the electrode, which may lead to performance loss.

The main advantage of the 3D heterogeneous model with a reconstructed microstructure compared to the homogenous models with averaged values for the physical parameters is that a better understanding of the effects of microstructure on the cell performance can be achieved, allowing for a comprehensive assessment of the performance barriers, specifically the SE/AM interface challenge. For instance, the simulation showed that the lithium-ions in the SE and AM have an inhomogenous distribution specifically at lower pressing pressures which may cause cell degradation. Comparing homogenous 1D and heterogeneous 3D model results demonstrated that, although the predicted voltage profiles are almost identical, the 3D model predicts higher ohmic losses due to the consideration of the electrode microstructure. Notably, at high current rates, the heterogeneity has a higher impact on the electrochemical property distributions where lithium-ion concentrations have a wider distribution range. The SE voltage drop distribution analysis depicted that at low pressing pressure the SE voltage drop is about twice that at high pressing pressure. It was also shown that in addition to the AM particle shape, which has a significant effect on current density distribution at the interface with the SE, the void spaces also play a critical role, i.e. current density peaks happen at the neck of sandglass microstructures and least near void spaces. Overall, the presented 3D heterogeneous model sheds light

on all aforementioned ASSBs' critical challenges and is a useful tool to address the effects of microstructural heterogeneity on cell behavior.

Chapter 5
Chemo-mechanical Modeling of Stress Evolution in All-Solid-State Lithium-Ion Batteries Using Synchrotron Transmission X-ray Microscopy Tomography

5.1 Introduction

The widespread adoption of electric vehicles (EVs) highly relies on the development of high-performance electrochemical energy storage systems. In past years, conventional lithium-ion batteries (LIBs) are commonly used to power the EVs, although these batteries still face critical challenges such as the flammability of organic liquid electrolyte, limited operating temperature and voltage range, and limited capacity. All-solid-state lithium-ion batteries (ASSBs) is a promising alternative to overcome the aforementioned drawbacks by employing an inflammable solid electrolyte (SE). They present less safety concerns and can facilitate high energy density cells by incorporating a Li metal anode. Despite the invaluable advantages of ASSBs, a multitude of factors need to be addressed. For instance, SEs, especially polymer solid-state electrolytes (SPEs), have poor ionic conductivity (10-6 $S.cm^{-1}$) and interfacial incompatibility among inorganic ASSBs at the SE/active material (AM) interface [43] also hinders large scale employment of ASSBs.

The SE/AM interfacial contact tremendously impacts the performance of ASSBs, as in contrast to liquid electrolytes, the physical mismatch between the two solid phases creates void spaces at the interface. In ASSBs, the composite cathode is generally fabricated by mixing the SE, AM, and a conductive agent. The composite microstructure and morphological properties depend on the mixing conditions, such as the external pressing pressure and temperature [43] while poor interfacial contact limits the lithium-ions transport pathways. Moreover, AM particle volume changes during lithiation/delithiation can lead to local stress build up in the microstructure, fracture propagation, and capacity fading [44]. Therefore, microstructure design is highly critical in ASSBs in comparison to

liquid electrolyte cells, where liquid electrolyte penetrates the porous electrode and the interfacial contact is not a remarkable issue. Most of the common cathode AMs expand during lithiation; although this volume change is negligible compared to that observed in alloy-based anode AMs, it is critical in ASSBs due to the solid/solid nature of the SE/AM interface. In other words, while liquid electrolyte cells can accommodate slight volume expansions of the cathode AM, for SE cells even minor volume changes could cause particle fracture and eventually pulverization [45]. Therefore, further investigation of the interfacial contact of ASSBs is crucial, since continuous expansion/contraction over the cycling of a cell can exacerbate the interfacial resistance and stress evolution.

The main sources of interfacial resistance at the SE/AM interface are the poor physical contact of the SE and AM [111], electrochemical instability of the SE/AM interface during cycling, and chemo-mechanical strain at the interface due to volume changes [112]. One of the effective approaches to improve poor contact in ASSBs is to optimize the external pressing pressure during the fabrication process [113]. The stress measurement techniques in ASSBs are generally categorized in the experimental method: employing multi-beam optical stress sensor (MOSS) which correlate the stress/strain in a thin film to its curvature during cycling [114, 115], finite element method (FEM): developing an electrochemical-mechanical model to compute the stress/strain by solving transport equations in the microstructure [116], and analytical approach, to calculate the stress evolution in ASSBs. It is worth noting that conducting *in situ* experiments on the SE/AM in ASSBs is difficult and time-consuming, whereas computational modeling can shed light on SE/AM morphological and electrochemical behavior and provide invaluable insights about ASSBs microstructural design [117].

There are a number of studies on the computational measurement of stress/strain in ASSBs available in the literature, which are mostly focused on 1D thin film[43, 118], or 2D planar geometries [116, 119, 120]. For instance, Bucci *et al.* developed the first quantitative analysis of ASSBs mechanical reliability by considering diffusion-induced volume changes. They reported that SEs with a low

stiffness are more likely to have micro-cracks due to their large deformation [116]. Moreover, Tian *et al.* developed a FEM-based electrochemical-mechanical model to evaluate stress in ASSBs. They reported that SE decomposition also causes volume change and consequently stress/strain formation in addition to diffusion-induced expansion [119]. It worth noting that they assumed an ideal physical contact at the SE/AM interface, although as discussed earlier, practical ASSBs, do not have complete interfacial contact. Recently, Yu et al. studied the deformation and stresses in the ASSB electrode by employing a virtual polycrystalline microstructure. They investigated the sintering and lithiation induced stress in the microstructure [121]. However, they assumed complete wettability of the SE while in realistic reconstructed microstructure of ASSBs, void space distribution has a remarkable effect on the electrochemical properties [117] and consequently on the lithiation induced stress.

To accurately portray the effect of morphology on the stress/strain evolution in ASSBs, the 3D reconstructed microstructure can be a prominent solution. Among various ex-*situ* imaging techniques, computed tomography (CT) is commonly used for LIBs to reconstruct 3D morphology based on 2D CT images [26, 27]. Employing CT reconstructed morphology can shed light on the spatial distribution of physical and electrochemical parameters such as lithium concentration, current density, and overpotential within the SE and AM phase [117]. Therefore, integrating a chemo-mechanical model for diffusion-induced stress modeling in ASSBs with 3D reconstructed morphology can provide invaluable insights regarding the stress/strain distribution at the SE/AM interface.

In this work, a chemo-mechanical model was implemented on 3D reconstructed ASSB morphologies fabricated under two different external pressing pressure for the first time. The primary goal is to shed light on the effect of the imperfect solid/solid interfacial contact of SE/AM on the stress/strain formation throughout charge-discharge cycling under a wide range of currents, as well as the effect of external pressing pressure on this phenomenon. The developed model has an electrochemical sub-model that includes diffusion and migration in the SE, diffusion in the AM, and charge transfer kinetics

at the SE/AM interface computed on a 3D reconstructed morphology. Moreover, the solid mechanics sub-model determines the diffusion induced stress/strain by employing a thermal-mass diffusion analogy. This chapter is structured in the following format: first, the electrochemical and solid mechanics sub-models are discussed. Then, the 3D modeling framework was implemented in Comsol Multiphysics 5.5. Finally, the simulation results are presented and discussed. The schematic of this study is presented in Figure 5-1.

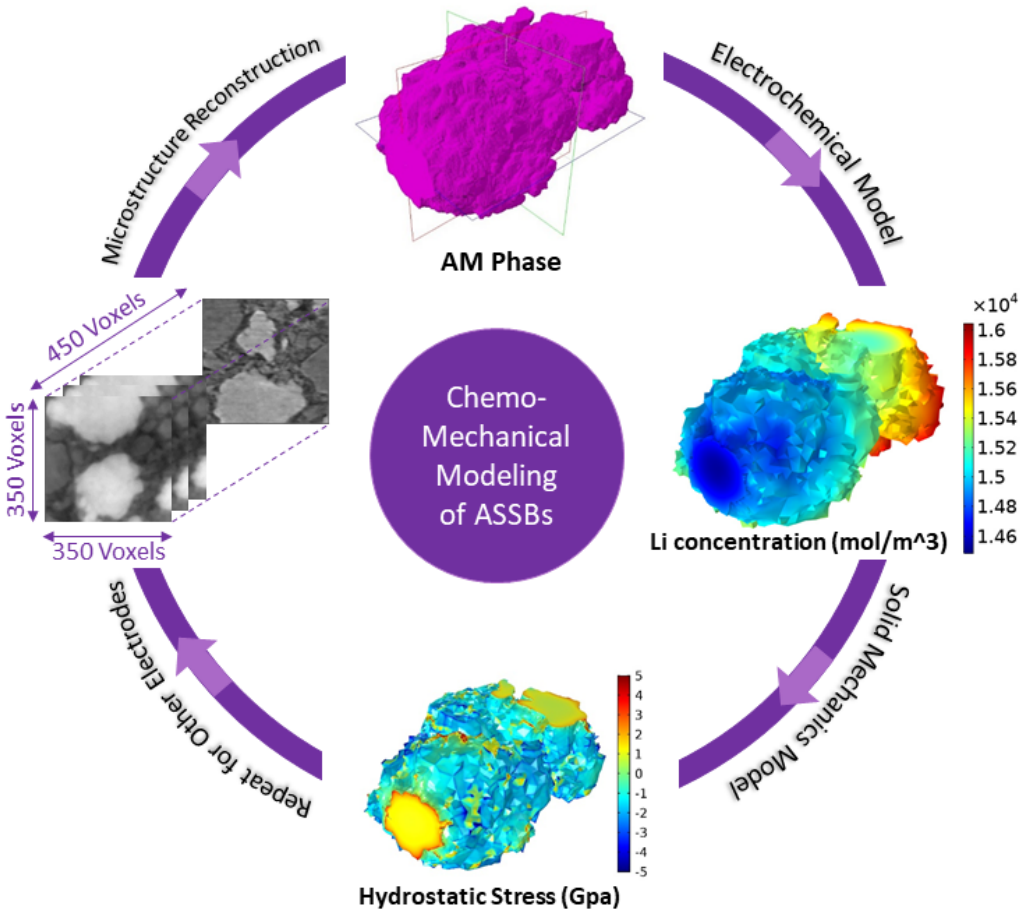

Figure 5-1 Schematic of chemo-mechanical modeling of ASSBs

5.2 Modeling

In LIBs the volume change of the cathode AM is often neglected; however, in ASSBs the AM cathode particles are surrounded by the SE where a minor volume change could cause critical issues. During cycling, the lithiation/delithiation of AM particles leads to morphological changes within AM particles to accommodate lithium-ions while SE structure changes are negligible due to its intrinsic nature [112]. The developed model consists of the electrochemical sub-model to solve charge transfer kinetics at the SE/AM interface, diffusion and migration of ions in the SE, and diffusion of ions in the AM. The equations have five unknown variables c_{Li}, c_{Li^+}, c_{n^-}, φ_s, and φ_{SE} which represent lithium concentration in the AM, lithium-ion concentration in the SE, negative charge concentration in the SE, AM potential, and SE potential, respectively. The gradient of lithium concentration within the AM is passed to the solid mechanics sub-model to determine the stress/strain evolution, which considers the SE/AM mechanical constraints in two different morphologies fabricated under different external pressing pressure.

5.2.1 Electrochemical Sub-Model

Although an inorganic SE behaves as a single-ion conductors [122]; it is widely common to simulate the SE as a binary electrolyte [85, 123, 124]. In a single ion-conducting electrolyte there is only one charged mobile species, Li^+, while in the binary electrolyte, the Li^+ and counterion are mobile. To implement a binary electrolyte methodology for SE simulation, electroneutrality condition $\sum z_k c_k = 0$ is assumed (k is either Li^+ or n^-). Therefore, at any time in the SE, $c_{Li^+} = c_{n^-}$. The overall reaction in SE is defined by:

$$\boldsymbol{r_d = k_d c_{Li^0} - k_r c_{Li^+} c_{n^-}}, \quad (5\text{-}1)$$

where k_d is the dissociation rate of $Li \rightarrow Li^+ + n^-$, and k_r is the inverse reaction rate. At the equilibrium state, the mobile lithium defined by:

$$\boldsymbol{c_{Li^+}^{eq} = c_{n^-}^{eq} = \delta c_0}, \quad (5\text{-}2)$$

where $c_{Li^+}^{eq}$, $c_{n^-}^{eq}$, c_0, and δ are the lithium-ion concentration at equilibrium, negative charge concentration at equilibrium, total lithium concentration, and fraction of mobile lithium in the SE, respectively. Nernst-Planck equation was implemented to simulate the lithium-ions transport behavior in the SE:

$$\boldsymbol{\frac{\partial c_{Li^+}}{\partial t} + \nabla . -D_{Li^+} \nabla c_{Li^+} + \frac{z_{Li^+} F}{RT} D_{Li^+} c_{Li^+} \nabla \varphi_{SE} = r_d}, \quad (5\text{-}3)$$

where z_{Li^+}, D_{Li^+}, F, φ_{SE} are the valence number, diffusion coefficient, Faraday's constant, and SE potential, respectively. Lithium diffusion within the AM phase was estimated by Fick's mass transport equation:

$$\boldsymbol{\frac{\partial c_{Li}}{\partial t} = -\nabla . (-D_{Li} \nabla c_{Li})}, \quad (5\text{-}4)$$

where c_{Li} and D_{Li} are the lithium concentration and diffusion coefficient of lithium in AM, respectively. Moreover, the rate of electrochemical reaction at the SE/AM interface is obtained by using Butler-Volmer kinetics as:

$$\boldsymbol{i_{pos} = i_{0,pos} (e^{\frac{\alpha_{pos} F \eta}{RT}} - e^{-\frac{(1-\alpha_{pos}) F \eta}{RT}})}, \quad (5\text{-}5)$$

$$\boldsymbol{i_{0,pos} = F k_{pos} \left(\frac{(c_{Li,max} - c_{Li}) c_{Li^+}}{(c_{Li,max} - c_{Li}) c_{Li^+,0}} \right)^{\alpha_{pos}} \left(\frac{c_{Li} - c_{Li,min}}{c_{Li,max} - c_{Li,min}} \right)^{1-\alpha_{pos}}}, \quad (5\text{-}6)$$

where i_{pos}, $i_{0,pos}$, k_{pos}, α_{pos}, $c_{Li,max}$ and $c_{Li,min}$ are the current density, exchange current density, apparent transfer coefficient, the reaction rate constant, and maximum and minimum of the lithium concentration in AM. The potential in the AM phase, φ_s, is described using Ohm's law in solids as follows:

$$\boldsymbol{i_{pos} = -\sigma_{pos} \nabla \varphi_s}, \quad (5\text{-}7)$$

where σ_{pos} is the conductivity of solid AM. At all SE cube sides, $\nabla\varphi = 0\ and\ \nabla c = 0$. The calculated lithium concentration in the AM and SE phases at each time step will be passed to the solid mechanics sub-model to calculate the diffusion induced stress formation.

5.2.2 Solid Mechanics Sub-Model

In ASSBs, the SE/AM interface has a vital role since only lithium-ions can transport through this interface; however, the solid rigid surfaces of the SE and AM lead to a gap formation at the interface. Therefore, ASSBs cannot form a perfect SE/AM interface. At the microscopic level, diffusion-induced stress and strain exacerbate the contact problem [43]. To quantify the stress formation in the AM, SE, and SE/AM interface during cycling, a solid mechanics model was developed and coupled with the aforementioned electrochemical model. The deformation gradient is obtained by [78]:

$$\boldsymbol{F} = (\boldsymbol{I} + \boldsymbol{\nabla u}), \tag{5-8}$$

where u is the displacement vector and I is the identity matrix. Lithium insertion leads to SE and AM volume expansion while the volume change depends on lithium concentration gradient Δc: [125]

$$\frac{\boldsymbol{V}}{\boldsymbol{V_0}} = \mathbf{det}(\boldsymbol{F_c}) = \mathbf{1} + \boldsymbol{\Omega}\Delta\boldsymbol{c}, \tag{5-9}$$

where V, V_0, and F_c are the current volume, initial volume, and lithium concentration induced deformation. The general definition of Ω is the partial molar volume change of host material after accommodating one mole of a guest atom. For lithium in NMC111, $\Omega = 3 \times 10^{-6}\ {}^{m^3}/_{mol}$ [44]. The lithiation induced deformation calculated by:

$$\boldsymbol{F_{c,ij}} = \sqrt[3]{\mathbf{1} + \boldsymbol{\Omega}\Delta\boldsymbol{c}}\boldsymbol{\delta_{ij}}, \tag{5-10}$$

where δ_{ij} is the Kronecker delta. To evaluate the stress formation, the Cauchy stress tensor σ can be derived by [73]:

$$\boldsymbol{\sigma} = (\mathbf{det}(\boldsymbol{F}))^{-\mathbf{1}}\boldsymbol{FSF^T}, \tag{5-11}$$

where S is the second Piola-Kirchhoff stress. In the electrode microstructure. To implement lithiation induced expansion, thermal-mass diffusion analogy was incorporated while temperature increment is replaced by a concentration difference. The strain is calculated by:

$$\boldsymbol{\varepsilon_{ij}^{T}} = (\sqrt[3]{\mathbf{1} + \boldsymbol{\Omega\Delta c}} - \mathbf{1})\boldsymbol{\Delta c \delta_{ij}}. \quad (5\text{-}12)$$

The boundary condition at the SE/AM interface is assumed to be a flexible attachment. The modeling methodology and all boundary conditions are illustrated in Figure 5-2 and model parameters are presented in Table 5-1. Li diffusion coefficient assumed to be concentration independent during cycling. Also, Fraction of free lithium-ion in equilibrium assumed to be 0.18.

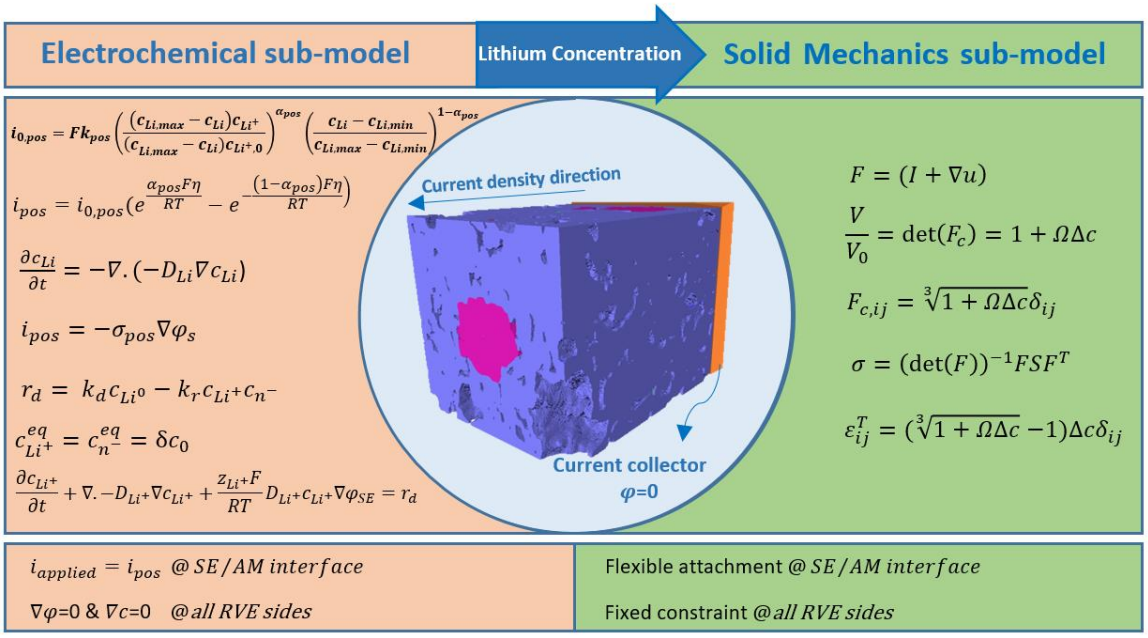

Figure 5-2 Modeling methodology including electrochemical and solid mechanics sub-models governing equations, boundary condition, current collector and current density direction.

Table 5-1 Model parameters

Parameter	Unit	Estimated Value	Description
a_0	$mol\ m^{-3}$	6.01×10^4 [86]	Total activity of Li atoms in SE matrix
k_r	$m^3 mol^{-1} s^{-1}$	0.9×10^{-8} [86]	Lithium-ion recombination reaction rate
δ	-	0.18 [86]	Fraction of free lithium-ion in equilibrium
D_{Li^+}	$m^2 s^{-1}$	0.9×10^{-13} [117]	Diffusion coefficient for lithium-ion in the SE (LTAP)
D_{Li}	$m^2 s^{-1}$	1.76×10^{-13} [117]	Diffusion coefficient for lithium in AM (NMC)
D_{n^-}	$m^2 s^{-1}$	5.1×10^{-13} [117]	Diffusion coefficient for n^- in the electrolyte
a_{pos}^{max}	$mol\ m^{-3}$	2.33×10^4 [86]	Maximum activity of the lithium in the positive electrode
α_{pos}	-	0.6 [86]	Charge transfer coefficient in the positive electrode
k_{poa}	$mol\ m^{-2} s^{-1}$	5.1×10^{-6} [86]	Rate constant charge transfer positive electrode
Ω	$m^3 mol^{-1}$	3×10^{-6} [44]	partial molar volume change of NMC-111
E_{AM}	Gpa	199 [126]	Young's modulus of NMC-111
v_{AM}	-	0.25 [126]	Poisson's ratio of NMC-111
E_{SE}	Gpa	143.7 [127]	Young's modulus of LTAP
v_{AM}	-	0.25 [127]	Poisson's ratio of LTAP

5.2.3 RVE Selection

As mentioned, the reconstructed morphology was used to compute the electrochemical and solid mechanics equations. It is worth noting that utilizing the whole electrode microstructure can be computationally expensive. Therefore, a representative volume element (RVE) was chosen instead of the whole electrode microstructure. To ensure the validity of results in RVE, the SE, AM, and pore volume fractions and volume specific surface area of the AM were measured and compared at various RVE sizes to minimize the difference with the whole electrode structure. Therefore, the electrochemical and solid mechanics simulations were modeled on a sub-volume geometry with a dimension of $350 \times 350 \times 450$ Voxels (10867 μm^3) which has similar properties compared to the whole microstructure (Table 5-2). The reconstructed morphology of the composite electrodes under 1300 psi

and 700 psi are presented in Figure 5-3. The generated mesh for 1300 psi electrode has 276543 elements (Figure 5-3g) and the 700 psi electrode has 234579 elements (Figure 5-3i). The simulations were conducted on CMC compute cad cluster with 8 nodes delivering 8.6 TFLOPS. The running time for each simulation varies from 40 to 42 hours. The meshing was conducted using AVIZO software without any mesh refinement.

Table 5-2 Volume specific surface area, AM, SE, and pore volume fractions in different RVE sizes in two composite electrodes with different external pressing pressures.

Pressing pressure 1300 psi							
Total Volume (μm^3)	19714	15968	12617	10867	7097	4929	3154
Volume specific surface area (1/μm)	0.601	0.614	0.620	0.621	0.635	0.649	0.658
Solid Active material (%)	28.5	28.2	27.9	28.8	27.5	27.1	24.3
Solid Electrolyte (%)	51.8	52.4	52.9	52.5	53.4	54.8	56.8
Pore (%)	19.7	19.4	19.2	18.7	19.1	18.1	18.9
Pressing pressure 700 psi							
Total Volume (μm^3)	19714	15968	12617	10867	7097	4929	3154
Volume specific surface area (1/μm)	0.502	0.514	0.522	0.521	0.538	0.551	0.567
Solid Active material (%)	29.3	28.7	28.3	29.9	27.4	26.1	25.4
Solid Electrolyte (%)	43.8	44.2	43.7	42.6	45.2	54.1	56.8
Pore (%)	26.9	27.1	28.0	27.5	27.4	19.8	17.8

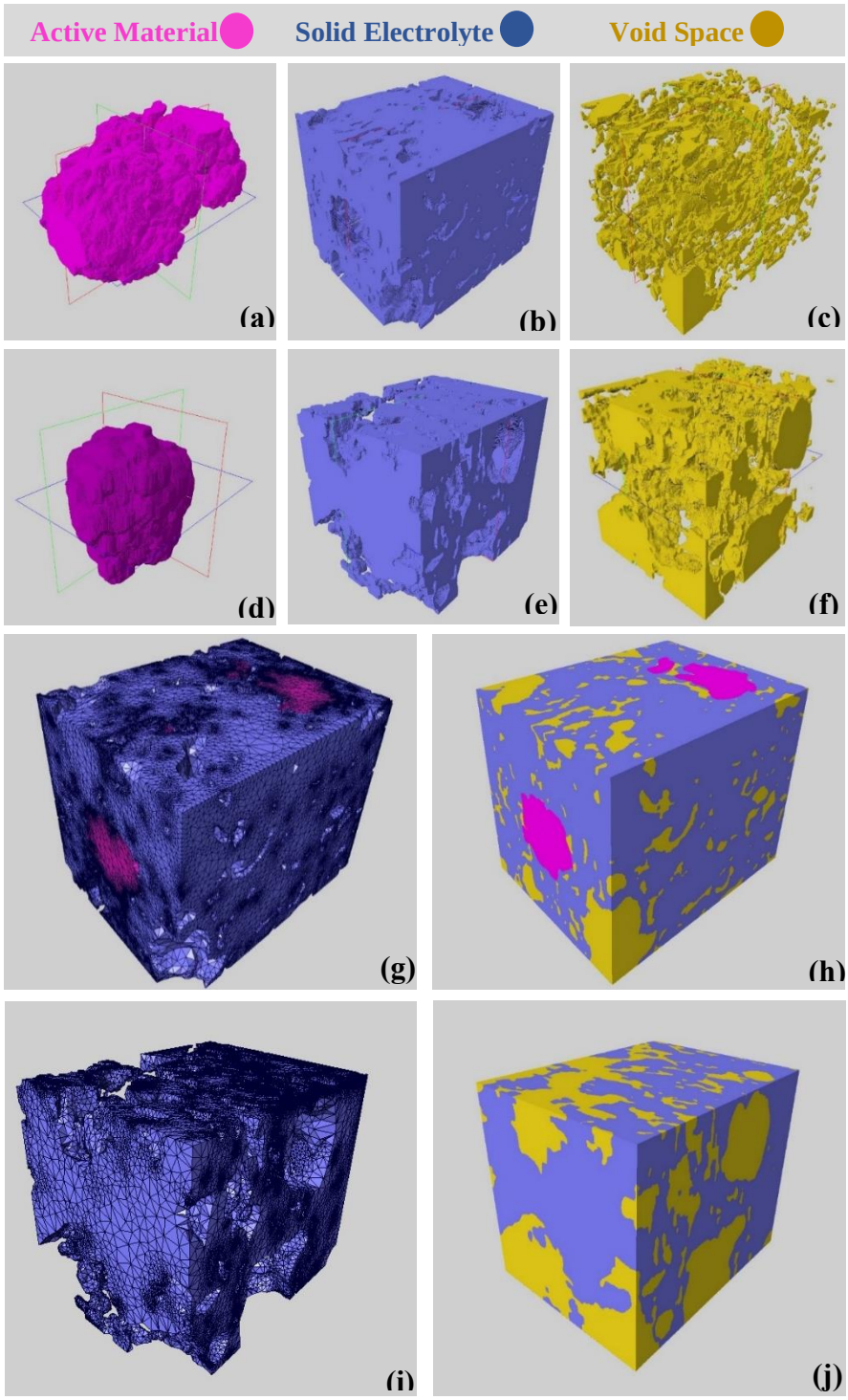

Figure 5-3 Reconstructed morphology of the electrode at two pressing pressures, (a-c) 1300 psi, (d-f) 700 Psi, (g) mesh and (h) reconstructed 3 phase electrode under 1300 psi pressing pressure, (i) mesh and (j) reconstructed 3 phase electrode under 700 psi pressing pressure.

5.3 Results and Discussion

The heterogeneous microstructure of the ASSB composite electrodes causes the in-homogenous distribution of physical and electrochemical properties within the electrodes' morphology. Additionally, the mechanical stability of the electrode highly relies on the microstructural design, and lithiation/delithiation induced expansion/contraction can cause contact loss and crack formation at the SE/AM interface [128]. To quantify the effect of the electrode morphology on the lithium distribution in the AM, the electrochemical sub-model methodology was implemented on the reconstructed microstructures fabricated under two external pressing pressures. As illustrated in Figure 5-5*a-f*, during the lithiation, there is a declining trend of lithium concentration in the AM along with the applied current density direction and a gradient in the AM particle radius direction due to lithium transport limitation. Moreover, at the surface of the AM particles, the imperfect SE/AM interface limits the lithium-ion pathways, which causes a variation in lithium concentration. Increasing the external pressing pressure can enhance the contact area and lithium transport, which can be verified by a higher average of lithium concentration in the AM particles at any state of charge (SOC) for the electrode with 1300 psi external pressing pressure applied compared with 700 psi applied, see Figure 5-5*g-l*. To ensure the fidelity of results, the developed electrochemical model was validated and compared with the experimental data [117]. To highlight the heterogeneous distribution of lithiation induced stress within the composite electrode, the results are illustrated on either two cross-section planes (yz-xz) or the yz plane. Figure 5-4 presents the morphology of the electrodes fabricated with 1300 psi and 700 psi pressing pressure.

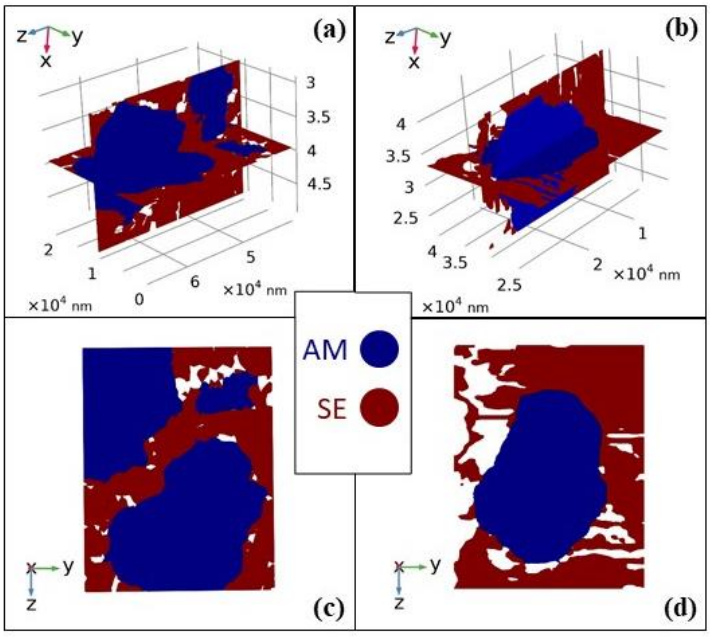

Figure 5-4 Cross-section view of the composite electrode with 1300 psi external pressing pressure in (a) two yz and xz planes, and (c) yz plane. Cross-section view of the composite electrode with 700 psi external pressing pressure in (b) two yz and xz planes, and (d) yz plane.

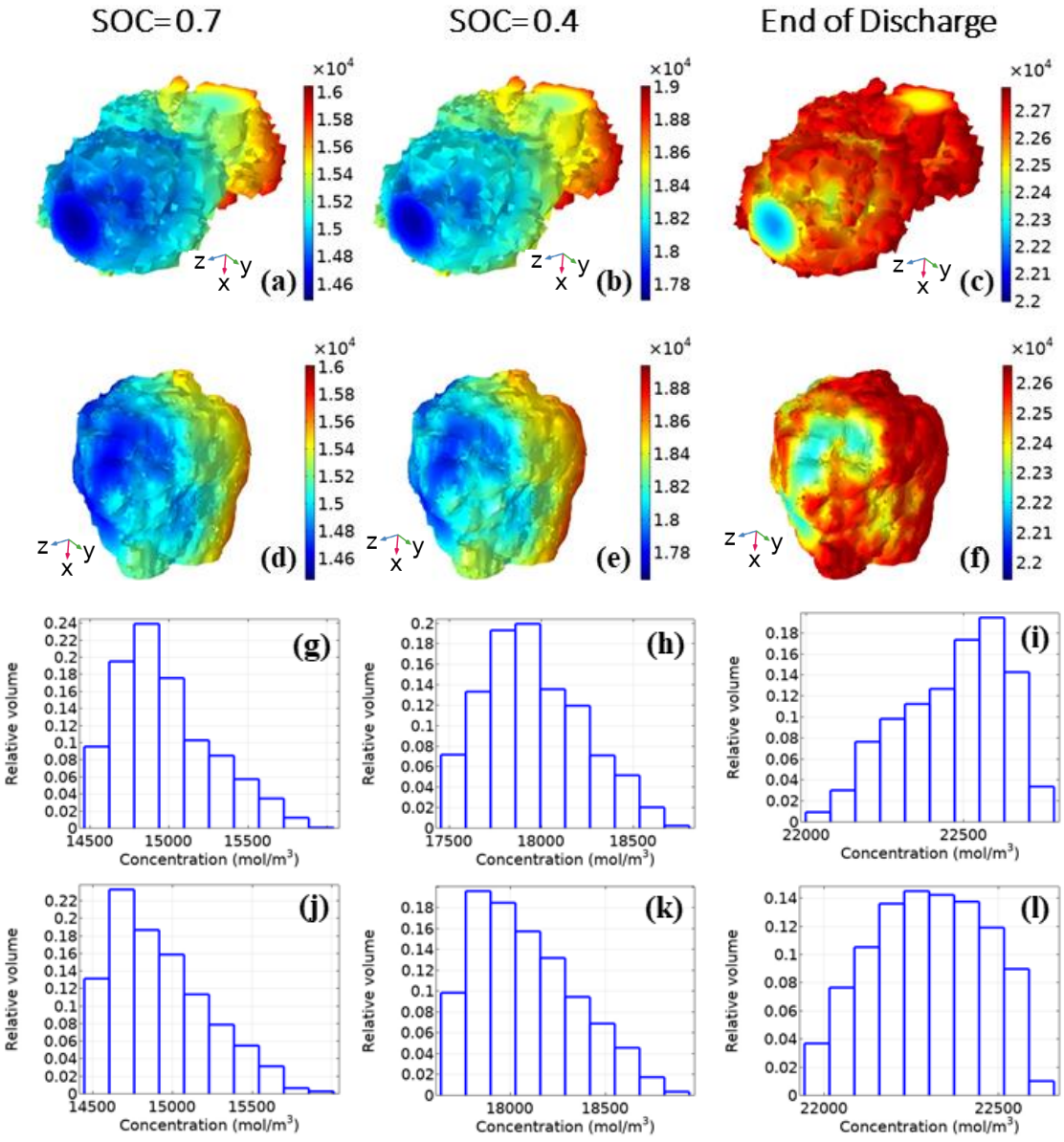

Figure 5-5 Lithium concentration in AM under two external pressing pressure (a-c) 1300 psi and (d-f) 700 psi during 3 C discharge rate. Histograms illustrate the lithium concentration in AM under two external pressing pressure (g-i) 1300 psi and (j-l) 700 psi during 3 C discharge rate.

5.4 Results and Discussion

5.4.1 Effects of external pressing pressure

It is worth noting that although increasing the external pressing pressure can alleviate the SE/AM contact resistances and enhance the ion transport, it may negatively affect the mechanical stability of the electrode. The main reason for this is that lithium diffusion induced volume change in AM particles can lead crack formation and a loss of contact due to the excessive stress evolution at the interface. The lithiation induced stress during the 1 C discharge rate in the composite electrode with 1300 psi external pressing pressure is illustrated in Figure 5-6a-c using two cross-section planes. The maximum stress is observed at the end of lithiation due to high lithium concentration. With closer examination, anisotropic stress distribution within the AM particles not only depends on their shapes, but also depends on the void space distribution at the SE/AM interface. In other words, void spaces at the SE/AM interface could partially accommodate volume changes and the AM particles undergo lower stress compared to the points with perfect contact with the SE. To clarify the effect of the SE/AM interface on the stress distribution, the stress evolution over 1 C discharge in the composite electrode with 700 psi external pressing pressure is illustrated in Figure 5-6d-f. Comparing Figure 5-6***c*** and Figure 5-6f, it can be concluded that the electrode with lower external pressing pressure encounters low hydrostatic stress under the same operating conditions due to its lower SE/AM surface area. On the z-y plane, the hydrostatic stress at the AM/pore interface is as low as 0.7 GPa (end of discharge), while the hydrostatic stress at the SE/AM is within the range of 3-4 GPa at the same SOC. Throughout lithiation, the distribution of lithiation-induced stress within the AM follows the same trend while hydrostatic stress within AM particles is mostly compressive except near void spaces (Figure 5-6*g-l*).

To further elaborate on the effects of the external pressing pressure and the composite electrode microstructure on the distribution of lithiation induced stress, the von Mises stress distribution is illustrated in Figure 5-7. The von Mises stress evolution in the composite electrode under 1300 psi

pressing pressure during 1 C lithiation is presented in Figure 5-7a-c on two cross-section planes and Figure 5-7g-i on a yz plane. Under the same conditions, the Von Mises stress evolution for the electrode fabricated with 700 psi external pressing pressure is presented in Figure 5-7j-l. The results show that von Mises stress peak points happen at the SE/AM interface. For instance, at the end of lithiation, the composite electrode encounters several peak points of 5 Gpa at SE/AM interface while the von Mises stress at AM/pore interface is below 1 Gpa. Moreover, the electrode with higher pressing pressure has a relatively higher von Mises stress specifically at the SE/AM interface which could cause fracture formation within the SE. Although higher pressing pressure can enhance ion pathways and alleviate contact resistances at the SE/AM interface [117], it causes excessive stress evolution at the SE/AM interface. Therefore, the microstructural design of ASSBs is highly critical to find an optimal tradeoff of the fabrication process such as external pressing pressure and the electrode chemo-mechanical performance.

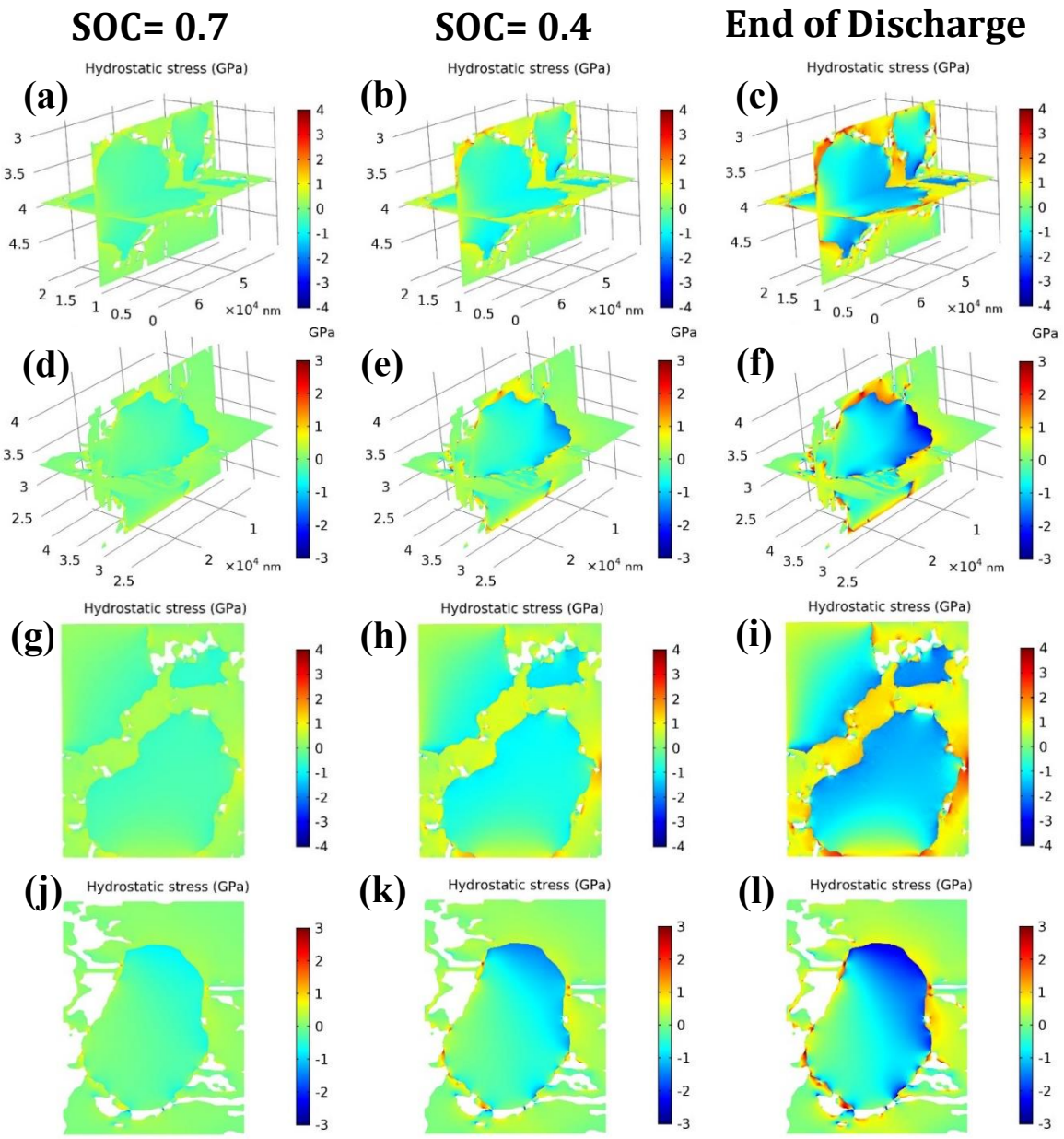

Figure 5-6 Hydrostatic stress in the composite electrode during 1C lithiation fabricated under (a-c) 1300 psi and (d-f) 700 psi illustrated in two cross-section planes (zy and xz). Hydrostatic stress in the composite electrode during 1C lithiation fabricated under (g-i) 1300 psi and (j-l) 700 Psi illustrated in yz plane.

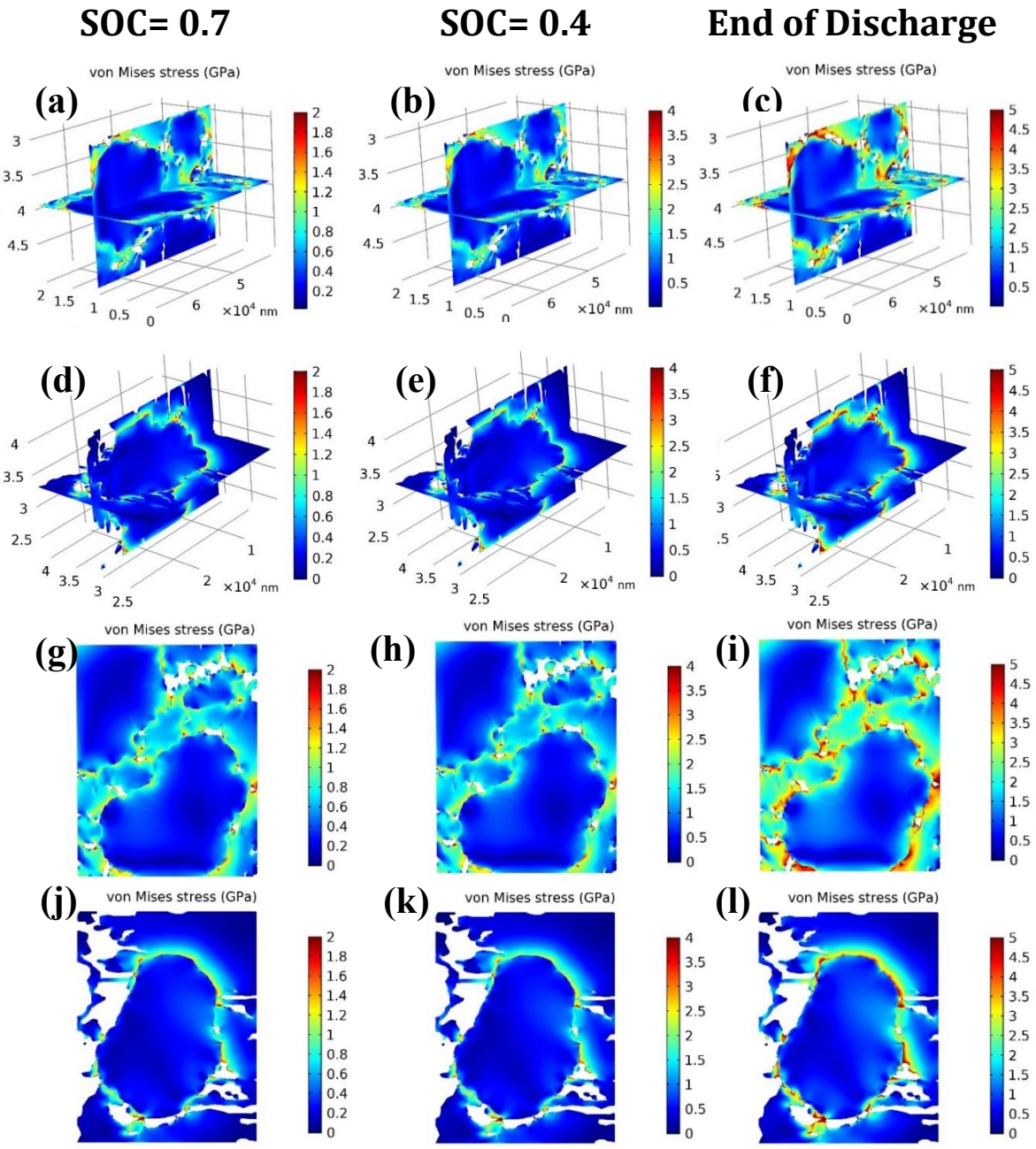

Figure 5-7 Von Mises stress in the composite electrode during 1C lithiation fabricated under (a-c) 1300 psi and (d-f) 700 psi illustrated in two cross-section planes (zy and xz). Von Mises stress in the composite electrode during 1C lithiation fabricated under

5.4.2 Effects of Current

In addition to morphological properties, applied current can affect the mechanical and electrochemical behavior of ASSBs. With increasing current, there is not enough time to fully lithiate the AMs, therefore the heterogeneous distribution of lithium concentration within the AM would have a wide range which limits the electrode capacity. The effects of current on electrochemical properties within the ASSB microstructure were previously investigated thoroughly. On the other hand, applied current can attribute to stress evolution during battery operation. The hydrostatic von Mises stress during 3 C lithiation is compared with 1 C lithiation. The hydrostatic and von Mises stress are presented in Figure 5-8a-c and Figure 5-8d-f for 3 C lithiation in two cross-section planes, respectively. Figure 5-8g-l illustrates the aforementioned stresses on a yz plane with the same order. Comparing Figure 5-8 with Figure 5-7 and Figure 5-6, it can be concluded that the hydrostatic stress and von Mises stress within the microstructure under 1C and 3C lithiation almost have an identical distribution. At high currents, lithium concentration has a relatively larger gradient within the AM particles and the lower lithium concentration at the particles' core may alleviate the stress evolution. The same observation was previously reported for other active materials such as Si [129]. However, the partial molar volume of NMC is much lower than Si. Thus, increasing current cannot significantly decrease the stress evolution within the microstructure (Figure 5-8).

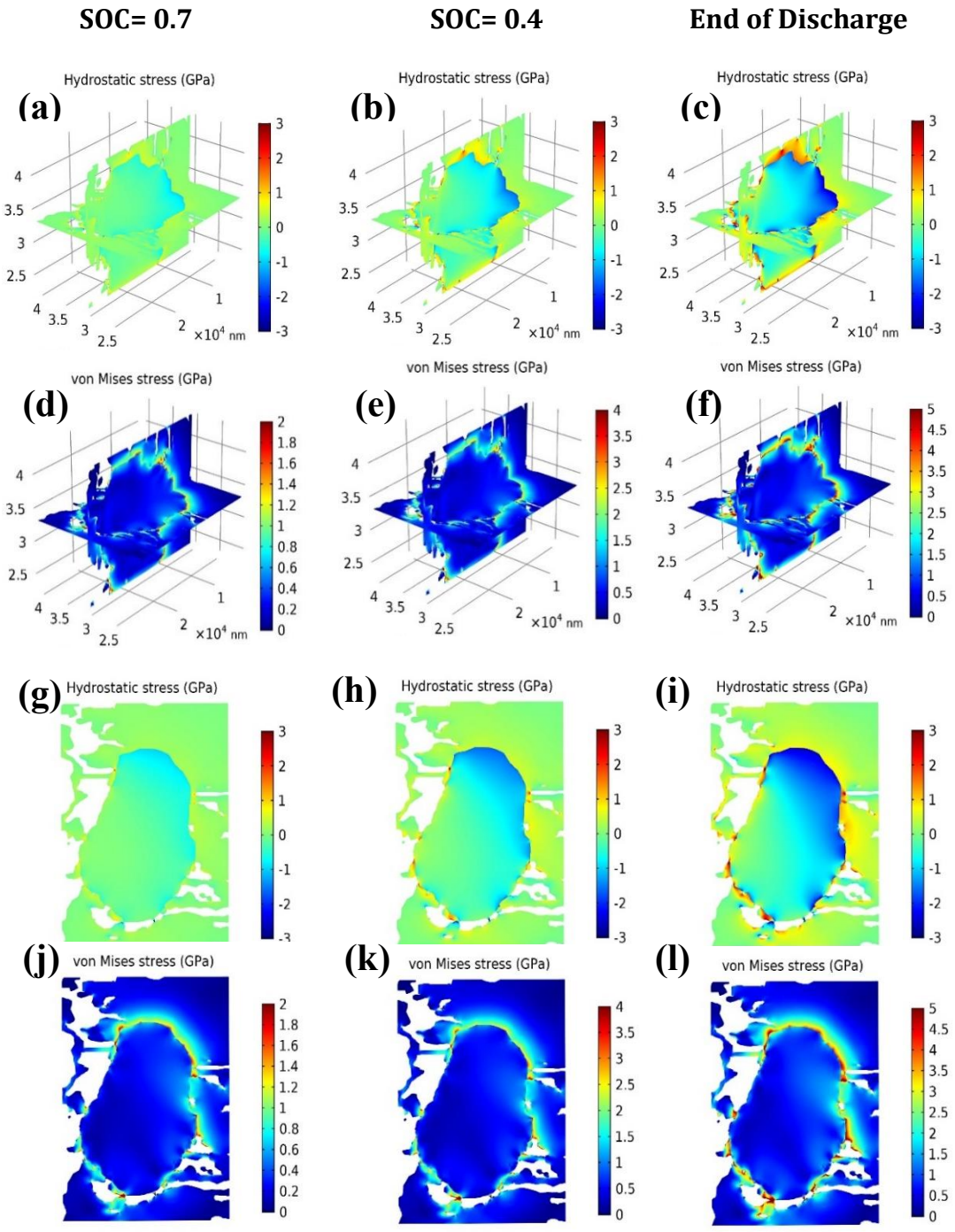

Figure 5-8 (a-c) Hydrostatic stress and (d-f) von Mises stress in the composite electrode during 3C lithiation fabricated 700 psi illustrated in two cross-section planes (zy and xz). (g-i) Hydrostatic stress and (j-i) von Mises stress in the composite electrode during 3C lithiation fabricated under 700 Psi illustrated in yz plane.

5.4.3 Effects of SE Stiffness

The mechanical properties of SEs have rarely been investigated in the literature, although optimizing the SE mechanical properties can effectively attenuate stress evolution within the composite electrode microstructure, and prevent fracture propagation and mechanical degradation. Although the Young's modulus of the SE in this study (LTAP) is 143.7 GPa, there is a wide range of available SEs with low stiffness, such as sulfide solid electrolytes that fall in the range of 14-25 GPa [116]. Overall, stiff SEs are more likely to undergo mechanical fracture and lose contact [130]. Therefore, to quantify the effect of SE stiffness, the hydrostatic and von Mises stress in the composite electrode are compared at two SE Young's modulus, 14.3 GPa, and 143 Gpa. Figure 5-9a-c and Figure 5-9d-f illustrate the hydrostatic and von Mises stress within the composite microstructure, fabricated under 700 psi external pressing pressure, at the end of 1C lithiation for the SE with 14.3 GPa SE Young's modulus, respectively. Figure 5-9g-l presents the aforementioned stresses on a yz plane with the same order. The presented results show that the SE stiffness tremendously affects the lithiation-induced stress within the ASSBs' microstructure. For instance, at the end of lithiation, the maximum hydrostatic stress and von Mises stress, in the composite electrode with the stiffer SE, are 3 GPa and 4.9 GPa, respectively; while in the other electrode (E_{SE}= 14.3 GPa), the maximum hydrostatic stress and von Mises stress are 0.6 GPa and 1 GPa, respectively. Thus, employing SE with low stiffness can be beneficial to inhibit stress evolution; however, the stiff electrolyte can suppress AM volume change. Suppressing AM expansion mostly becomes critical for alloy-based anode active materials which have relatively larger volume expansion, and to prevent dendrite formation on lithium metal anodes [131]. Therefore, optimizing the SE stiffness based on the application and AMs can balance the stress evolution and volume changes.

Figure 5-10a-c and Figure 5-10d-f illustrate the hydrostatic and von Mises stress within the composite microstructure, fabricated under 1300 psi external pressing pressure, at the end of 1C lithiation with considering 14.3 GPa SE Young's modulus, respectively. Figure 5-9g-l presents the

aforementioned stresses on a yz plane with the same order. The presented results support the aforementioned state that decreasing SE stiffness can limit the stress evolution. However, the yield strength of materials is proportional to Young's modulus; thus, crack formation at stress peak points in the SE with low stiffness is more likely to happen.

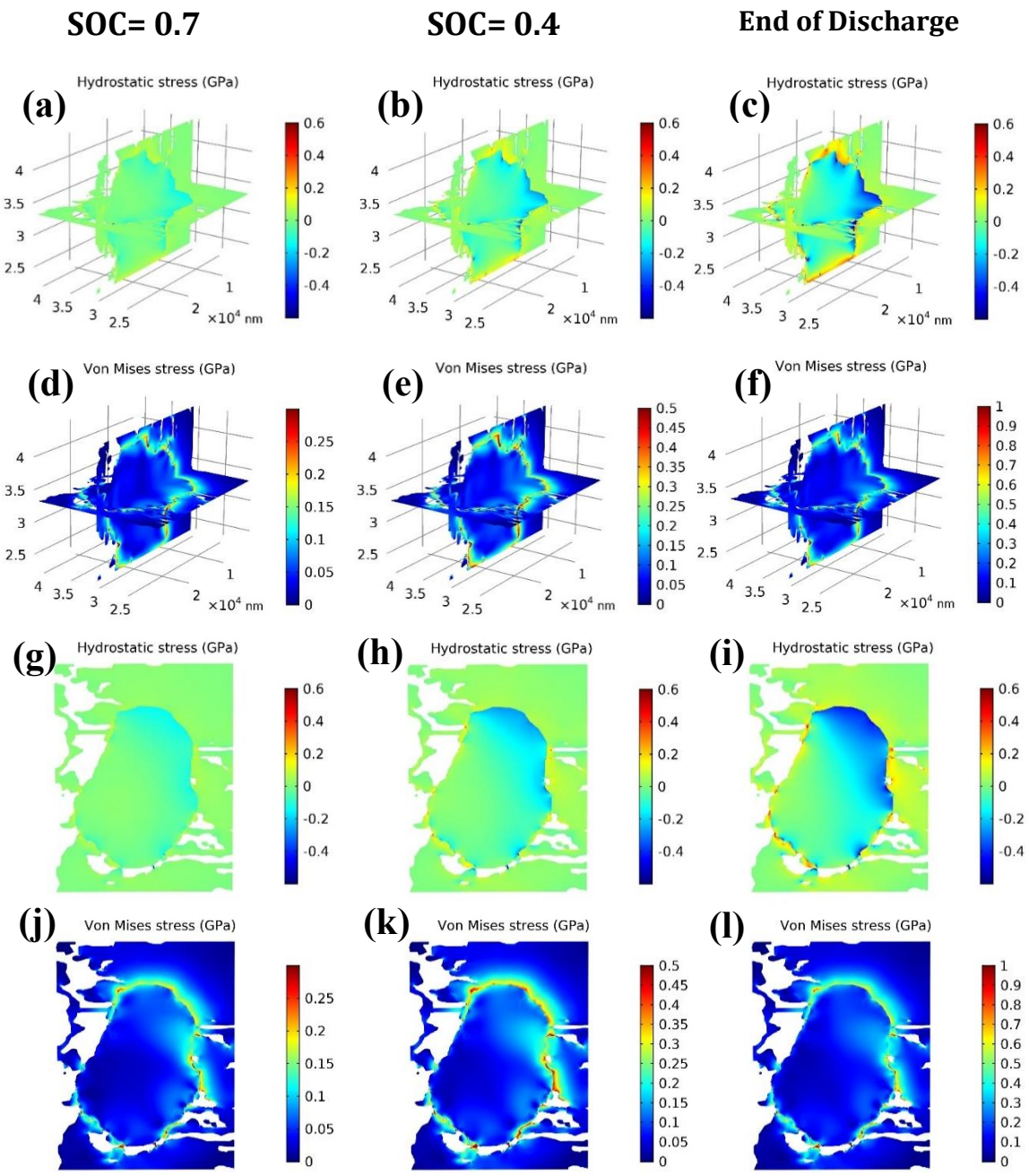

Figure 5-9 (a-c) Hydrostatic stress and (d-f) von Mises stress in the composite electrode during 1C lithiation fabricated under 700 psi external pressing pressure illustrated in two cross-section planes (zy and xz). (g-i) Hydrostatic stress and (j-i) von Mises stress in the composite electrode during 1C lithiation fabricated under 700 Psi illustrated in yz plane. SE Young's module is assumed to be 14.3 Gpa.

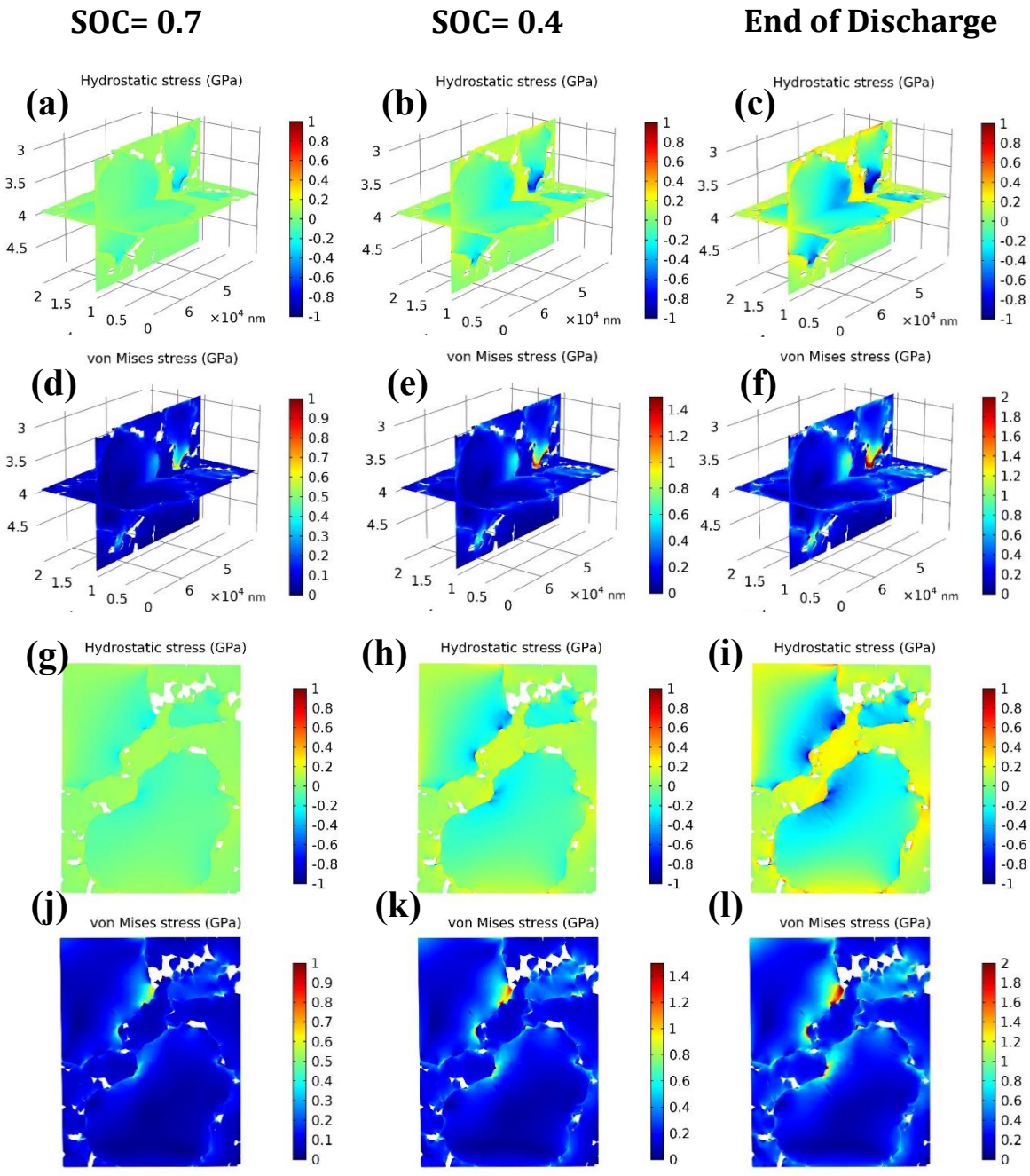

Figure 5-10 (a-c) Hydrostatic stress and (d-f) von Mises stress in the composite electrode during 1C lithiation fabricated under 1300 psi external pressing pressure illustrated in two cross-section planes (zy and xz). (g-i) Hydrostatic stress and (j-i) von Mises stress in the composite electrode during 1C lithiation fabricated under 1300 Psi illustrated in yz plane. SE Young's module is assumed to be 14.3 Gpa

5.4.4 Anisotropic Displacement

Anisotropic volume changes of AM particles leads to a change in particle shape, which may cause mechanical degradation and contact loss with SE [132]. The variation of directional displacement under 1C lithiation in the AM phase of composite electrodes with 700 psi and 1300 psi external pressing pressure is illustrated in Figure 5-11a. Displacement in the z-direction (parallel to the applied external pressing pressure) has the lowest value; while in the 700 psi electrode, the AM phase has a maximum displacement of 958 nm and 847 nm in the x- and y-directions (perpendicular to the applied external pressing pressure), respectively. With increased external pressing pressure, the displacement variation significantly decreased, where the AM phase maximum displacement becomes 439 nm and 259 nm in the x- and y-directions, respectively. The main reason is that external pressing pressure suppresses the void space and thus limits the displacement. Moreover, applying external pressing pressure can prevent anisotropic swelling of the active materials while directional displacement at lower external pressing pressure has a wider range of distribution (Figure 5-11a).

As mentioned in section 5.4.3, the current has a negligible effect on the lithiation-induced stress evolution within the electrode microstructure due to the relatively low partial molar volume expansion of the NMC. To further elaborate on this issue, the directional displacement of the AM phase under 1 C and 3 C lithiation are compared in Figure 5-11b. The directional displacements, specifically at the perpendicular directions, are somewhat lower. At high currents, a larger gradient of lithium concentration within the AM particles causes slightly lower lithiation-induced expansion at the end of lithiation because the concentration at the AM particle surface reaches the cut-off value while the lithium concentration inside the particle is lower. Additionally, the effects of SE stiffness on the anisotropic displacement of the AM phase are illustrated in Figure 5-11c. Although decreasing the SE Young's module can alleviate the stress evolution, the AM phase possesses relatively larger displacement which can intensify crack propagation within the microstructure. For instance, when

changing the SE Young's module from 143.7 GPa to 14.3 GPa, the AM maximum displacement at the end of lithiation is 2350 nm and 2300 nm in the x- and y-direction, respectively.

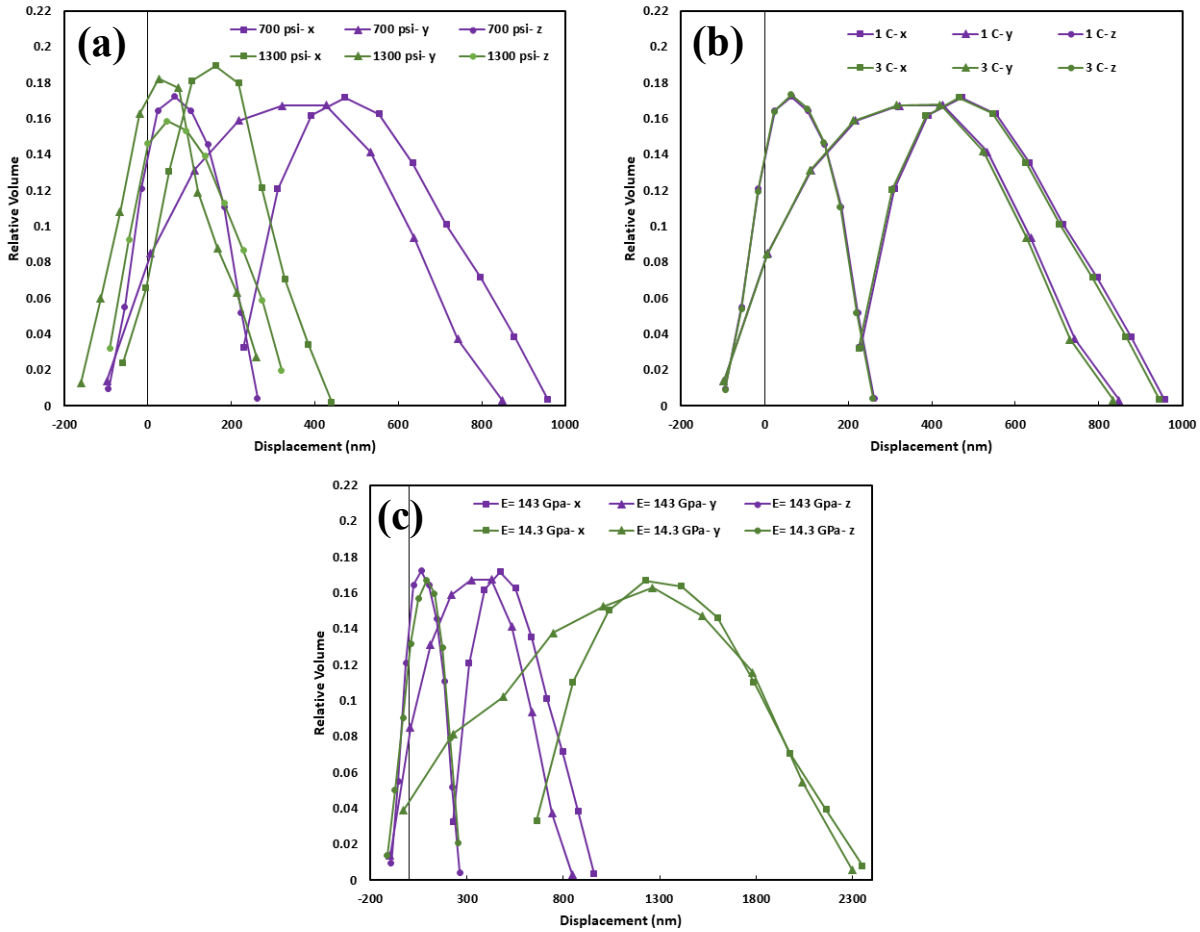

Figure 5-11 (a) Directional displacement of AM phase in composite electrodes with 700 psi and 1300 psi external pressing pressure during 1C lithiation and (b) directional displacement of AM phase phase in composite electrodes with 700 psi external pressing pressure during 1C and 3C lithiation and (c) directional displacement of AM phase in composite electrodes with 700 psi during 1C lithiation considering SE Young's modulus of 14.3 GPa and 143 GPa.

5.5 Conclusions

In this study, we developed a chemo-mechanical model for ASSBs composite electrode that incorporates a 3D reconstructed microstructure of the electrode using TXM images, fabricated under two external pressing pressures. The simulation results clarify the effects of SE/AM interface and void space distribution within the microstructure on the lithiation induced stress during the battery operation. The results show that AM particles encounter compressive hydrostatic stress up to 4 GPa at the SE/AM interface during lithiation, while the SE limits their expansion. On the other hand, void space can partially accommodate the AM expansion, where areas near void spaces have tensile stress within the range of 0-1 Gpa. The electrode with higher external pressing pressure experiences a relatively higher hydrostatic stress due to a higher SE/AM interfacial contact and the decreased amount of void space. The simulated von Mises stress confirms this behavior. At the end of lithiation, the von Mises stress in AM particles is approximately zero while at the surface, the AM confronts up to 4.9 GPa stress which could cause crack formation and mechanical degradation. The electrode with higher pressing pressure has more peak stress points and the average von Mises stress within the microstructure with higher pressing pressure is 2.4 GPa compared to 1.5 GPa. Therefore, the microstructural design of the SE/AM interface is critical to find an optimal tradeoff of maximizing ion pathways and minimizing the stress evolution. It was also shown that unlike anode AMs, which have larger volume expansion, the effects of current on the stress evolution in the composite cathode microstructure is negligible due to the relatively small partial molar volume of cathode AMs. However, SE stiffness has a significant impact on the stress evolution and anisotropic displacement in the composite electrode. Decreasing SE stiffness, by changing the SE Young's module, can adjust the maximum hydrostatic stress and von Mises stress from 3 GPa and 4.9 GPa to 0.6 GPa and 1 GPa, respectively. Conversely, the stiff SE can suppress AM swelling and attenuate anisotropic displacement of AMs which may improve the mechanical integrity of the composite electrode.

Chapter 6
Conclusions and Future Work

6.1 Summary and Conclusions

In the present thesis, multi-physics models have been successfully developed to clarify the physical, electrochemical, and mechanical behavior of LIBs. The developed models aimed to tackle LIBs' challenges and provide invaluable insights regarding cell design. Employing alloy-based anode active materials with higher theoretical capacity and solid electrolytes, instead of common flammable organic liquid electrolytes, is investigated to address the limited energy density and safety drawbacks of LIBs.

Earlier in the thesis work, a multi-scale multi-physics model was developed to study a composite Gr/Si electrode for LIBs. The model was based on macroscale P2D modeling of cycling performance based on the aforementioned electrochemical sub-model integrated with microscale single-particle modeling of Si including the lithium transport equation within the particle and solid mechanics sub-model to investigate the lithiation-induced stress evolution during the battery operation. In each time step, the lithium concentration within the Si particle updated with the new volume due to the particle expansion/contraction throughout lithiation/delithiation. The main advantage of this developed universal modeling framework is the adaptability of this methodology to a wide range of composite electrodes. It has also given remarkable insights regarding the effects of the current and Si percentage on the deformation and stress evolution considering the effect of lithium chemical potential within Si and how it changes under stress. Moreover, it can shed light on developing physics-based battery state estimation models for composite Si-based electrodes that considers the effects of Si deformation and stress evolution.

Additionally, the physical, electrochemical, and mechanical behavior of ASSBs were modeled to investigate the advantages and limitations of employing solid electrolyte instead of conventional liquid

electrolytes in LIBs. The developed model was implemented on the reconstructed 3D morphology of the composite ASSB electrodes to enhance the fidelity of the model. The main benefit of incorporating the 3D microstructure of the electrode, compared with 1D and 2D simplified geometries, is that the developed model can enlighten the heterogeneous distribution of physical and electrochemical properties within the microstructure and the effects of fabrication and operation conditions on these properties. Special attention was paid to the SE/AM interface while the imperfect contact and solid/solid nature of this interface could limit the ion pathways and intensify cell degradation and capacity fade.

To further elaborate the effect of the SE/AM interface and void spaces in the composite electrode microstructure, a chemo-mechanical model was developed based on solving an electrochemical and solid mechanics coupled model on the 3D reconstructed morphology of the composite ASSB electrodes using XCT imaging technique. The developed model highlights the vital role of the fabrication process on the cell performance while composite electrodes encounter remarkable stress which varies in the microstructure depending on the shape of the active material particles and their contact with the SE. It is worth noting that lithiation-induced stress has peak points at SE/AM interfaces due to the solid/solid nature of this interface. Maximizing SE/AM contact with increasing external pressing pressure during fabrication may enhance ion pathways and alleviate contact resistances; however, the higher contact causes larger stress evolution at the interface which may lead to crack formation and mechanical degradation. Unlike anode AMs, which have larger volume expansion, effects of current on the stress evolution in the composite cathode microstructure is negligible due to the relatively small partial molar volume of cathode AMs. However, SE stiffness has a significant impact on the stress evolution and anisotropic displacement in the composite electrode. Decreasing SE stiffness can alleviate stress evolution. Conversely, stiff SE can suppress the AM swelling and attenuate anisotropic displacement of AMs which may improve the mechanical integrity of the composite electrode.

In conclusion, integrating multi-physics modeling with XCT technology can effectively address the LIBs' challenges and provide invaluable insights to tackle these challenges and find an optimal design based on the application criteria.

6.2 Proposed Future Work

Based on the findings of this Ph.D. study, some future directions for the modeling of LIBs can be suggested:

1. Integrating multi-physics modeling with a data-driven methodology

   Multi-physics modeling is a powerful tool to investigate the behavior of batteries; however, it has some limitations such as relatively high computational. While the data-driven methodology has a self-learning intrinsic feature that can tremendously decrease computation cost and predict the behavior of LIBs with high precision. Furthermore, data-driven methods can be applied to various types of batteries without the necessary knowledge of occurring phenomena, while multi-physics model implementation requires accurate solving of governing equations. In other words, highly non-linear and complex reactions in batteries may not completely be captured by multi-physics simulation; however, data-driven methods can effectively consider all aspects of the system with training the model over the experimental data sets.

2. Incorporating machine learning algorithms in interpreting electrodes microstructure morphology

   Due to the recent improvement of imaging technology, new facilities are able to capture the electrode image with the resolution of a few nanometers. Image segmentation to differentiate phases of an electrode is a quite challenging task. Segmentation is a time-consuming process and the accuracy of the results highly depends on the threshold values, specifically for separating more than two phases in an image. Machine learning algorithms such as a convolutional neural network (CNN) are widely employed for facial recognition and analyzing documents. CNN can

effectively apply to the grayscale electrode images to recognize phases. The main benefit of using CNN would be higher accuracy and less computation cost.

3. Mechanical stress analysis in ASSBs under a real operating condition

   In the present study, the lithiation induced stress extensively elaborated under a galvanostatic discharge condition. However, real operating conditions may intensify the stress evolution. Therefore, the developed chemo-mechanical framework can be implemented using a dynamic driving cycle such as Federal Urban Driving Schedule (FUDS) or Urban Dynamometer Driving Schedule (UDDS) to investigate the stress at various operating scenarios.

4. Employing pore network modeling

   One of the effective ways to reduce the multi-physics simulation computational cost is to employ the pore network modeling method, instead of adopting 3D reconstructed morphology of the electrode. Implementing pore network methodology, specifically on a large stack of electrode images, can lead to a substantially fewer number of unknowns.

References

1. *IEA (2017), Energy Technology Perspectives*. 2017, IEA, Paris
2. *IEA (2019), Global EV Outlook* 2019, IEA, Paris
3. Lu, L., et al., *A review on the key issues for lithium-ion battery management in electric vehicles.* 2013. **226**: p. 272-288.
4. Feng, X., et al., *Thermal runaway mechanism of lithium ion battery for electric vehicles: A review.* 2018. **10**: p. 246-267.
5. Ma, H., et al., *Nest-like Silicon Nanospheres for High-Capacity Lithium Storage.* Advanced Materials, 2007. **19**(22): p. 4067-4070.
6. Lee, J.K., et al., *Silicon nanoparticles–graphene paper composites for Li ion battery anodes.* Chemical Communications, 2010. **46**(12): p. 2025-2027.
7. Li, W., et al., *Mechanics-based optimization of yolk-shell carbon-coated silicon nanoparticle as electrode materials for high-capacity lithium ion battery.* Composites Communications, 2016. **1**: p. 1-5.
8. Yook, S.-H., et al., *Graphite–silicon alloy composite anodes employing cross-linked poly (vinyl alcohol) binders for high-energy density lithium-ion batteries.* RSC Advances, 2016. **6**(86): p. 83126-83134.
9. Kannan, A.G., et al., *Silicon nanoparticles grown on a reduced graphene oxide surface as high-performance anode materials for lithium-ion batteries.* RSC Advances, 2016. **6**(30): p. 25159-25166.
10. Hochgatterer, N., et al., *Silicon/graphite composite electrodes for high-capacity anodes: influence of binder chemistry on cycling stability.* Electrochemical and solid-state letters, 2008. **11**(5): p. A76-A80.
11. Liu, W.-R., et al., *Enhanced cycle life of Si anode for Li-ion batteries by using modified elastomeric binder.* Electrochemical and Solid-State Letters, 2005. **8**(2): p. A100-A103.
12. Sethuraman, V.A., et al., *In situ measurement of biaxial modulus of Si anode for Li-ion batteries.* Electrochemistry Communications, 2010. **12**(11): p. 1614-1617.
13. Zeng, Z., et al., *In situ measurement of lithiation-induced stress in silicon nanoparticles using micro-Raman spectroscopy.* Nano Energy, 2016. **22**: p. 105-110.
14. Wang, M., X. Xiao, and X. Huang, *A multiphysics microstructure-resolved model for silicon anode lithium-ion batteries.* Journal of Power Sources, 2017. **348**: p. 66-79.
15. Lv, F., et al., *Challenges and development of composite solid-state electrolytes for high-performance lithium ion batteries.* 2019. **441**: p. 227175.
16. Miller III, T.F., et al., *Designing polymer electrolytes for safe and high capacity rechargeable lithium batteries.* 2017. **50**(3): p. 590-593.
17. Li, Q., et al., *In-situ visualization of lithium plating in all-solid-state lithium-metal battery.* 2019. **63**: p. 103895.
18. Ping, W., et al., *A Silicon Anode for Garnet-Based All-Solid-State Batteries: Interfaces and Nanomechanics.* 2019.
19. Takada, K.J.A.M., *Progress and prospective of solid-state lithium batteries.* 2013. **61**(3): p. 759-770.
20. Kim, J.G., et al., *A review of lithium and non-lithium based solid state batteries.* 2015. **282**: p. 299-322.
21. Choi, S., et al., *Quantitative Analysis of Microstructures and Reaction Interfaces on Composite Cathodes in All-Solid-State Batteries Using a Three-Dimensional Reconstruction Technique.* 2018. **10**(28): p. 23740-23747.

22. Li, T., et al., *Three-Dimensional Reconstruction and Analysis of All-Solid Li-Ion Battery Electrode Using Synchrotron Transmission X-ray Microscopy Tomography*. 2018.
23. Biton, M., et al., *Enhanced imaging of lithium ion battery electrode materials.* 2017. **164**(1): p. A6032-A6038.
24. Hutzenlaub, T., et al., *Three-dimensional electrochemical Li-ion battery modelling featuring a focused ion-beam/scanning electron microscopy based three-phase reconstruction of a LiCoO2 cathode*. 2014. **115**: p. 131-139.
25. Ilott, A.J., et al., *Real-time 3D imaging of microstructure growth in battery cells using indirect MRI*. 2016. **113**(39): p. 10779-10784.
26. Kashkooli, A.G., et al., *Multiscale modeling of lithium-ion battery electrodes based on nano-scale X-ray computed tomography*. 2016. **307**: p. 496-509.
27. Kashkooli, A.G., et al., *Synchrotron X-ray nano computed tomography based simulation of stress evolution in LiMn2O4 electrodes.* 2017. **247**: p. 1103-1116.
28. Kashkooli, A.G., et al., *Morphological and electrochemical characterization of nanostructured Li4Ti5O12 electrodes using multiple imaging mode synchrotron X-ray computed tomography*. 2017. **164**(12): p. A2861-A2871.
29. Ghorbani Kashkooli, A., *Nanoscale X-ray Computed Tomography Based Modeling of Lithium-ion Battery Electrodes*. 2018, UWSpace.
30. Lee, S., et al., *Multi-scale morphological characterization of Ni foams with directional pores.* 2019: p. 109939.
31. Taiwo, O.O., et al., *Comparison of three-dimensional analysis and stereological techniques for quantifying lithium-ion battery electrode microstructures.* Journal of microscopy, 2016. **263**(3): p. 280-292.
32. Tariq, F., et al., *Three-dimensional high resolution X-ray imaging and quantification of lithium ion battery mesocarbon microbead anodes.* Journal of Power Sources, 2014. **248**: p. 1014-1020.
33. Pohjalainen, E., *Negative Electrode Materials for Lithium Ion Batteries.* 2016.
34. Zheng, F., et al., *Review on solid electrolytes for all-solid-state lithium-ion batteries.* 2018. **389**: p. 198-213.
35. Bruce, P.G. and A.R. West, *The A-C Conductivity of Polycrystalline LISICON, Li2+2xZn1-xGeO4, and a Model for Intergranular Constriction Resistances.* Journal of the Electrochemical Society, 1983. **130**(3): p. 662-669.
36. Inaguma, Y., et al., *Candidate compounds with perovskite structure for high lithium ionic conductivity.* Solid State Ionics, 1994. **70-71**(PART 1): p. 196-202.
37. Li, Y., et al., *A stable perovskite electrolyte in moist air for Li-ion batteries.* 2018.
38. El-Shinawi, H., et al., *NASICON LiM2(PO4)3 electrolyte (M = Zr) and electrode (M = Ti) materials for all solid-state Li-ion batteries with high total conductivity and low interfacial resistance.* Journal of Materials Chemistry A, 2018. **6**(13): p. 5296-5303.
39. Xiong, L., et al., *LiF assisted synthesis of LiTi2(PO4)3 solid electrolyte with enhanced ionic conductivity.* Solid State Ionics, 2017. **309**: p. 22-26.
40. Alexander, G.V., et al., *Electrochemical performance of a garnet solid electrolyte based lithium metal battery with interface modification.* 2018. **6**(42): p. 21018-21028.
41. Din, M.M.U. and R.J.E.C. Murugan, *Garnet structured solid fast Li+ conductor as polysulfide shuttle inhibitor in Li-S battery.* 2018. **93**: p. 109-113.
42. Zhao, E., et al., *High ionic conductivity Y doped Li1.3Al0.3Ti1.7(PO4)3 solid electrolyte.* Journal of Alloys and Compounds, 2019: p. 384-391.
43. Wang, P., et al., *Electro–Chemo–Mechanical Issues at the Interfaces in Solid-State Lithium Metal Batteries.* 2019. **29**(27): p. 1900950.

44. Koerver, R., et al., *Chemo-mechanical expansion of lithium electrode materials–on the route to mechanically optimized all-solid-state batteries.* 2018. **11**(8): p. 2142-2158.
45. Zhang, Y., C. Zhao, and Z.J.I.J.o.M.S. Guo, *Simulation of crack behavior of secondary particles in Li-ion battery electrodes during lithiation/de-lithiation cycles.* 2019. **155**: p. 178-186.
46. Chen, C., et al., *Stable lithium-ion conducting perovskite lithium–strontium–tantalum–zirconium–oxide system.* 2004. **167**(3-4): p. 263-272.
47. Ramadesigan, V., et al., *Modeling and simulation of lithium-ion batteries from a systems engineering perspective.* Journal of The Electrochemical Society, 2012. **159**(3): p. R31-R45.
48. Santhanagopalan, S., et al., *Review of models for predicting the cycling performance of lithium ion batteries.* Journal of Power Sources, 2006. **156**(2): p. 620-628.
49. Newman, J. and W. Tiedemann, *Porous-electrode theory with battery applications.* AIChE Journal, 1975. **21**(1): p. 25-41.
50. Doyle, M. and J. Newman, *The use of mathematical modeling in the design of lithium/polymer battery systems.* Electrochimica Acta, 1995. **40**(13-14): p. 2191-2196.
51. Fuller, T.F., M. Doyle, and J. Newman, *Simulation and optimization of the dual lithium ion insertion cell.* Journal of the Electrochemical Society, 1994. **141**(1): p. 1-10.
52. Albertus, P., J. Christensen, and J. Newman, *Experiments on and modeling of positive electrodes with multiple active materials for lithium-ion batteries.* Journal of the Electrochemical Society, 2009. **156**(7): p. A606-A618.
53. Mao, Z., et al., *Model-based prediction of composition of an unknown blended lithium-ion battery cathode.* Journal of The Electrochemical Society, 2015. **162**(4): p. A716-A721.
54. Mao, Z., et al., *Charge/Discharge Asymmetry in Blended Lithium-Ion Electrodes.* Journal of The Electrochemical Society, 2017. **164**(2): p. A39-A47.
55. Kok, M.D., et al., *Mass transfer in fibrous media with varying anisotropy for flow battery electrodes: Direct numerical simulations with 3D X-ray computed tomography.* 2019. **196**: p. 104-115.
56. Heenan, T.M., et al., *Three-phase segmentation of solid oxide fuel cell anode materials using lab based X-ray nano-computed tomography.* 2017. **17**(1): p. 75-82.
57. Epting, W.K., J. Gelb, and S.J.A.F.M. Litster, *Resolving the Three-Dimensional Microstructure of Polymer Electrolyte Fuel Cell Electrodes using Nanometer-Scale X-ray Computed Tomography.* 2012. **22**(3): p. 555-560.
58. Miller, D.J., et al., *Exploring Heterogeneity in Li Battery Electrodes using FIB-SEM Integrated with Raman and TOF-SIMS.* 2019. **25**(S2): p. 862-863.
59. Kumar, A.S., *Computational Methods for Nanoscale X-ray Computed Tomography Image Analysis of Fuel Cell and Battery Materials*. 2016, Carnegie Mellon University.
60. Samantaa, S., et al., *Multilevel threshold based gray scale image segmentation using cuckoo search.* 2013.
61. Joos, J., et al., *Reconstruction of porous electrodes by FIB/SEM for detailed microstructure modeling.* Journal of Power Sources, 2011. **196**(17): p. 7302-7307.
62. Liu, X.H., et al., *In situ transmission electron microscopy of electrochemical lithiation, delithiation and deformation of individual graphene nanoribbons.* Carbon, 2012. **50**(10): p. 3836-3844.
63. Zhang, S., *Chemomechanical modeling of lithiation-induced failure in high-volume-change electrode materials for lithium ion batteries.* npj Computational Materials, 2017. **3**(1): p. 1-11.
64. Zhang, W.-J., *A review of the electrochemical performance of alloy anodes for lithium-ion batteries.* Journal of Power Sources, 2011. **196**(1): p. 13-24.

65. Newman, J., *Optimization of porosity and thickness of a battery electrode by means of a reaction-zone model.* Journal of the Electrochemical Society, 1995. **142**(1): p. 97-101.
66. Delacourt, C. and M. Safari, *Life simulation of a graphite/LiFePO4 cell under cycling and storage.* Journal of The Electrochemical Society, 2012. **159**(8): p. A1283-A1291.
67. Doyle, M., T.F. Fuller, and J. Newman, *Modeling of galvanostatic charge and discharge of the lithium/polymer/insertion cell.* Journal of the Electrochemical Society, 1993. **140**(6): p. 1526-1533.
68. Wang, M., X. Xiao, and X. Huang, *Study of lithium diffusivity in amorphous silicon via finite element analysis.* Journal of Power Sources, 2016. **307**: p. 77-85.
69. Wang, M. and X. Xiao, *Investigation of the chemo-mechanical coupling in lithiation/delithiation of amorphous Si through simulations of Si thin films and Si nanospheres.* Journal of Power Sources, 2016. **326**: p. 365-376.
70. Gao, X., W. Lu, and J. Xu, *Modeling framework for multiphysics-multiscale behavior of Si–C composite anode.* Journal of Power Sources, 2020. **449**: p. 227501.
71. Hamed, F., et al., *Three-Dimensional Modeling of All-Solid-State Lithium-Ion Batteries Using Synchrotron Transmission X-ray Microscopy Tomography.* Journal of the Electrochemical Society, 2020.
72. Chakraborty, J., et al., *Combining mechanical and chemical effects in the deformation and failure of a cylindrical electrode particle in a Li-ion battery.* International Journal of Solids and Structures, 2015. **54**: p. 66-81.
73. Wang, M., X. Xiao, and X.J.J.o.P.S. Huang, *Study of lithium diffusivity in amorphous silicon via finite element analysis.* 2016. **307**: p. 77-85.
74. Shenoy, V.B., P. Johari, and Y. Qi, *Elastic softening of amorphous and crystalline Li–Si Phases with increasing Li concentration: A first-principles study.* Journal of Power Sources, 2010. **195**(19): p. 6825-6830.
75. Sethuraman, V.A., et al., *In situ measurements of stress evolution in silicon thin films during electrochemical lithiation and delithiation.* Journal of Power Sources, 2010. **195**(15): p. 5062-5066.
76. Zhao, K., et al., *Lithium-assisted plastic deformation of silicon electrodes in lithium-ion batteries: a first-principles theoretical study.* Nano letters, 2011. **11**(7): p. 2962-2967.
77. Yu, P., et al., *Determination of the lithium ion diffusion coefficient in graphite.* Journal of The Electrochemical Society, 1999. **146**(1): p. 8-14.
78. Wang, M. and X.J.J.o.P.S. Xiao, *Investigation of the chemo-mechanical coupling in lithiation/delithiation of amorphous Si through simulations of Si thin films and Si nanospheres.* 2016. **326**: p. 365-376.
79. Guo, J., et al., *Cyclability study of silicon–carbon composite anodes for lithium-ion batteries using electrochemical impedance spectroscopy.* Electrochimica Acta, 2011. **56**(11): p. 3981-3987.
80. Feng, K., et al., *Implementing an in-situ carbon network in Si/reduced graphene oxide for high performance lithium-ion battery anodes.* Nano Energy, 2016. **19**: p. 187-197.
81. Ren, Y., et al., *Preparation and characterization of silicon monoxide/graphite/carbon nanotubes composite as anode for lithium-ion batteries.* Journal of Solid State Electrochemistry, 2012. **16**(4): p. 1453-1460.
82. Zubi, G., et al., *The lithium-ion battery: State of the art and future perspectives.* 2018. **89**: p. 292-308.
83. Foreman, E., et al., *A Review of Inactive Materials and Components of Flexible Lithium-Ion Batteries.* 2017. **1**(11): p. 1700061.

84. Notten, P.H., et al., *3-D integrated all-solid-state rechargeable batteries.* Advanced Materials, 2007. **19**(24): p. 4564-4567.
85. Kazemi, N., et al., *Modeling of all-solid-state thin-film Li-ion batteries: Accuracy improvement.* 2019. **334**: p. 111-116.
86. Danilov, D., R. Niessen, and P.J.J.o.t.E.S. Notten, *Modeling all-solid-state Li-ion batteries.* 2011. **158**(3): p. A215-A222.
87. Fabre, S.D., et al., *Charge/discharge simulation of an all-solid-state thin-film battery using a one-dimensional model.* 2011. **159**(2): p. A104-A115.
88. Raijmakers, L., et al., *An advanced all-solid-state Li-ion battery model.* 2019: p. 135147.
89. Wolff, N., F. Röder, and U.J.E.A. Krewer, *Model Based Assessment of Performance of Lithium-Ion Batteries Using Single Ion Conducting Electrolytes.* 2018. **284**: p. 639-646.
90. Bates, A., et al., *Modeling and simulation of 2D lithium-ion solid state battery.* 2015. **39**(11): p. 1505-1518.
91. Clancy, T.M. and J.F.J.J.o.E.S. Rohan, *Simulations of 3D nanoscale architectures and electrolyte characteristics for Li-ion microbatteries.* 2019. **23**: p. 1-8.
92. Banerjee, R., et al., *Carbon felt electrodes for redox flow battery: Impact of compression on transport properties.* 2019. **26**: p. 100997.
93. Tippens, J., et al., *Visualizing Chemo-Mechanical Degradation of a Solid-State Battery Electrolyte.* 2019.
94. Choi, S., et al., *Tomographical analysis of electrochemical lithiation and delithiation of LiNi0. 6Co0. 2Mn0. 2O2 cathodes in all-solid-state batteries.* 2019. **165**: p. 10-14.
95. Asl, N.M., et al., *Inorganic solid/organic liquid hybrid electrolyte for use in Li-ion battery.* 2012. **79**: p. 8-16.
96. Tjaden, B., et al., *On the origin and application of the Bruggeman correlation for analysing transport phenomena in electrochemical systems.* Current Opinion in Chemical Engineering, 2016. **12**: p. 44-51.
97. Bruggeman, V.D., *Berechnung verschiedener physikalischer Konstanten von heterogenen Substanzen. I. Dielektrizitätskonstanten und Leitfähigkeiten der Mischkörper aus isotropen Substanzen.* Annalen der physik, 1935. **416**(7): p. 636-664.
98. Cooper, S., et al., *Image based modelling of microstructural heterogeneity in LiFePO4 electrodes for Li-ion batteries.* 2014. **247**: p. 1033-1039.
99. Pang, M.-C., et al., *Experimental and numerical analysis to identify the performance limiting mechanisms in solid-state lithium cells under pulse operating conditions.* 2019. **21**(41): p. 22740-22755.
100. Kashkooli, A.G., et al., *Morphological and Electrochemical Characterization of Nanostructured Li4Ti5O12 Electrodes Using Multiple Imaging Mode Synchrotron X-ray Computed Tomography.* Journal of The Electrochemical Society, 2017. **164**(12): p. A2861-A2871.
101. Ghorbani Kashkooli, A., et al., *Synchrotron X-ray nano computed tomography based simulation of stress evolution in LiMn2O4 electrodes.* Electrochimica Acta, 2017. **247**(Supplement C): p. 1103-1116.
102. Mistry, A.N., K. Smith, and P.P. Mukherjee, *Secondary-phase stochastics in lithium-ion battery electrodes.* ACS applied materials & interfaces, 2018. **10**(7): p. 6317-6326.
103. Kashkooli, A.G., et al., *Representative volume element model of lithium-ion battery electrodes based on X-ray nano-tomography.* Journal of Applied Electrochemistry, 2017. **47**(3): p. 281-293.
104. Wu, S.-L., et al., *High rate capability of Li (Ni1/3Mn1/3Co1/3) O2 electrode for Li-ion batteries.* Journal of The Electrochemical Society, 2012. **159**(4): p. A438-A444.

105. Knauth, P., *Inorganic solid Li ion conductors: An overview.* Solid State Ionics, 2009. **180**(14-16): p. 911-916.
106. Zhao, Y., et al., *A review on modeling of electro-chemo-mechanics in lithium-ion batteries.* 2019. **413**: p. 259-283.
107. Trembacki, B.L., et al., *Mesoscale analysis of conductive binder domain morphology in lithium-ion battery electrodes.* Journal of The Electrochemical Society, 2018. **165**(13): p. E725-E736.
108. Hlushkou, D., et al., *The influence of void space on ion transport in a composite cathode for all-solid-state batteries.* 2018. **396**: p. 363-370.
109. Koerver, R., et al., *Capacity fade in solid-state batteries: interphase formation and chemomechanical processes in nickel-rich layered oxide cathodes and lithium thiophosphate solid electrolytes.* Chemistry of Materials, 2017. **29**(13): p. 5574-5582.
110. Bucci, G., et al., *Modeling of internal mechanical failure of all-solid-state batteries during electrochemical cycling, and implications for battery design.* Journal of Materials Chemistry A, 2017. **5**(36): p. 19422-19430.
111. Bucci, G., et al., *Mechanical instability of electrode-electrolyte interfaces in solid-state batteries.* 2018. **2**(10): p. 105407.
112. He, Y., et al., *Interfacial Incompatibility and Internal Stresses in All-Solid-State Lithium Ion Batteries.* 2019. **9**(36): p. 1901810.
113. Li, T., et al., *Three-Dimensional Reconstruction and Analysis of All-Solid Li-Ion Battery Electrode Using Synchrotron Transmission X-ray Microscopy Tomography.* 2018. **10**(20): p. 16927-16931.
114. Sethuraman, V.A., et al., *In situ measurements of stress evolution in silicon thin films during electrochemical lithiation and delithiation.* 2010. **195**(15): p. 5062-5066.
115. Pharr, M., Z. Suo, and J.J.J.N.l. Vlassak, *Measurements of the fracture energy of lithiated silicon electrodes of Li-ion batteries.* 2013. **13**(11): p. 5570-5577.
116. Bucci, G., et al., *Modeling of internal mechanical failure of all-solid-state batteries during electrochemical cycling, and implications for battery design.* 2017. **5**(36): p. 19422-19430.
117. Fathiannasab, H., et al., *Three-Dimensional Modeling of All-Solid-State Lithium-Ion Batteries Using Synchrotron Transmission X-ray Microscopy Tomography.* 2020.
118. Nolan, A.M., et al., *Computation-accelerated design of materials and interfaces for all-solid-state lithium-ion batteries.* 2018. **2**(10): p. 2016-2046.
119. Tian, H.-K., et al., *Evaluation of The Electrochemo-Mechanically Induced Stress in All-Solid-State Li-Ion Batteries.* 2020. **167**(9): p. 090541.
120. Song, X., et al., *A coupled electro-chemo-mechanical model for all-solid-state thin film Li-ion batteries: The effects of bending on battery performances.* 2020. **452**: p. 227803.
121. Yu, H.-C., et al., *Deformation and stresses in solid-state composite battery cathodes.* 2019. **440**: p. 227116.
122. Wolff, N., F. Roeder, and U.J.E.A. Krewer, *Model based assessment of performance of lithium-ion batteries using single ion conducting electrolytes.* 2018. **284**: p. 639-646.
123. Raijmakers, L., et al., *An advanced all-solid-state Li-ion battery model.* 2020. **330**: p. 135147.
124. Danilov, D., R. Niessen, and P.J.J.o.t.E.S. Notten, *Modeling all-solid-state Li-ion batteries.* 2010. **158**(3): p. A215.
125. Wang, M., X. Xiao, and X.J.J.o.P.S. Huang, *A multiphysics microstructure-resolved model for silicon anode lithium-ion batteries.* 2017. **348**: p. 66-79.
126. Cheng, E.J., et al., *Mechanical and physical properties of LiNi0. 33Mn0. 33Co0. 33O2 (NMC).* 2017. **37**(9): p. 3213-3217.

127. Deng, Z., et al., *Elastic properties of alkali superionic conductor electrolytes from first principles calculations.* 2015. **163**(2): p. A67.
128. Koerver, R., et al., *Capacity fade in solid-state batteries: interphase formation and chemomechanical processes in nickel-rich layered oxide cathodes and lithium thiophosphate solid electrolytes.* 2017. **29**(13): p. 5574-5582.
129. Gao, X., W. Lu, and J.J.J.o.P.S. Xu, *Modeling framework for multiphysics-multiscale behavior of Si–C composite anode.* 2020. **449**: p. 227501.
130. Pervez, S.A., et al., *Interface in solid-state lithium battery: challenges, progress, and outlook.* 2019. **11**(25): p. 22029-22050.
131. Zhang, F., et al., *A review of mechanics-related material damages in all-solid-state batteries: Mechanisms, performance impacts and mitigation strategies.* 2020. **70**: p. 104545.
132. Wu, X., et al., *Operando Visualization of Morphological Dynamics in All-Solid-State Batteries.* 2019. **9**(34): p. 1901547.
133. Kashkooli, A.G., et al., *Application of Artificial Intelligence to State-of-Charge and State-of-Health Estimation of Calendar-Aged Lithium-Ion Pouch Cells.* Journal of The Electrochemical Society, 2019. **166**(4): p. A605-A615.
134. Xiong, R., et al., *Critical review on the battery state of charge estimation methods for electric vehicles.* Ieee Access, 2017. **6**: p. 1832-1843.
135. Hu, X., et al., *State estimation for advanced battery management: Key challenges and future trends.* Renewable and Sustainable Energy Reviews, 2019. **114**: p. 109334.
136. Hu, X., S.E. Li, and Y. Yang, *Advanced machine learning approach for lithium-ion battery state estimation in electric vehicles.* IEEE Transactions on Transportation electrification, 2015. **2**(2): p. 140-149.
137. Song, Y., et al., *A hybrid statistical data-driven method for on-line joint state estimation of lithium-ion batteries.* Applied Energy, 2020. **261**: p. 114408.
138. Kilic, A., et al., *Assessment of Critical Materials and Cell Design Factors for High Performance Lithium-Sulfur Batteries using Machine Learning.* Chemical Engineering Journal, 2020: p. 124117.
139. Attia, P.M., et al., *Closed-loop optimization of fast-charging protocols for batteries with machine learning.* Nature, 2020. **578**(7795): p. 397-402.
140. Spingler, F.B., et al., *Optimum fast charging of lithium-ion pouch cells based on local volume expansion criteria.* Journal of Power Sources, 2018. **393**: p. 152-160.
141. Howell, D. *US DOE Electric Vehicle Battery R&D Progress and Plans*. in *Meeting Abstracts*. 2016. The Electrochemical Society.
142. Mathieu, R., et al. *Comparative Ageing Study of CC-CV Fast Charging for Commercial 18650 Li-Ion Cells: Impact of Environmental Temperature*. in *2019 IEEE Vehicle Power and Propulsion Conference (VPPC)*. 2019. IEEE.
143. Liu, J., G. Li, and H.K. Fathy, *A computationally efficient approach for optimizing lithium-ion battery charging.* Journal of Dynamic Systems, Measurement, and Control, 2016. **138**(2).
144. Liu, K., et al., *Multi-objective optimization of charging patterns for lithium-ion battery management.* Energy Conversion and Management, 2018. **159**: p. 151-162.
145. Xu, M., et al., *Fast charging optimization for lithium-ion batteries based on dynamic programming algorithm and electrochemical-thermal-capacity fade coupled model.* Journal of Power Sources, 2019. **438**: p. 227015.
146. Guo, Z., et al., *Optimal charging method for lithium ion batteries using a universal voltage protocol accommodating aging.* Journal of Power Sources, 2015. **274**: p. 957-964.
147. Jiang, J., *Charging Optimization Methods for Lithium-Ion Batteries,* in *Behaviour of Lithium-Ion Batteries in Electric Vehicles*. 2018, Springer. p. 225-265.

148. Zhang, C., et al., *Charging optimization in lithium-ion batteries based on temperature rise and charge time.* Applied energy, 2017. **194**: p. 569-577.
149. Feng, F., et al., *A review of equalization strategies for series battery packs: variables, objectives, and algorithms.* Renewable and Sustainable Energy Reviews, 2019. **116**: p. 109464.
150. Cui, X., et al., *A novel active online state of charge based balancing approach for lithium-ion battery packs during fast charging process in electric vehicles.* Energies, 2017. **10**(11): p. 1766.
151. Porpora, F., et al. *Real time balancing for modular passive battery management system*. in *PCIM Europe 2019; International Exhibition and Conference for Power Electronics, Intelligent Motion, Renewable Energy and Energy Management*. 2019. VDE.
152. Diao, W., et al., *Active battery cell equalization based on residual available energy maximization.* Applied energy, 2018. **210**: p. 690-698.
153. Chen, Y., et al., *A multiwinding transformer cell-to-cell active equalization method for lithium-ion batteries with reduced number of driving circuits.* IEEE Transactions on Power Electronics, 2015. **31**(7): p. 4916-4929.
154. Zheng, X., et al., *Active vehicle battery equalization scheme in the condition of constant-voltage/current charging and discharging.* IEEE Transactions on Vehicular Technology, 2016. **66**(5): p. 3714-3723.
155. Gallardo-Lozano, J., et al., *Battery equalization active methods.* Journal of Power Sources, 2014. **246**: p. 934-949.
156. Xia, B., et al. *A Novel Battery Equalization Method Base on Fuzzy Logic Control Considering Thermal Effect*. in *IOP Conference Series: Earth and Environmental Science*. 2019. IOP Publishing.
157. Wang, B., et al., *Equalization of series connected lithium-ion batteries based on back propagation neural network and fuzzy logic control.* International Journal of Energy Research, 2020.
158. Kim, J., et al. *OCV hysteresis effect-based SOC estimation in extended Kalman filter algorithm for a LiFePO 4/C cell*. in *2012 IEEE International Electric Vehicle Conference*. 2012. IEEE.
159. Ng, K.S., et al., *Enhanced coulomb counting method for estimating state-of-charge and state-of-health of lithium-ion batteries.* Applied energy, 2009. **86**(9): p. 1506-1511.
160. Xu, X., et al., *A hybrid observer for SOC estimation of lithium-ion battery based on a coupled electrochemical-thermal model.* International Journal of Green Energy, 2019. **16**(15): p. 1527-1538.
161. Wang, Q., et al., *Correlation between the model accuracy and model-based SOC estimation.* Electrochimica Acta, 2017. **228**: p. 146-159.
162. Codeca, F., S.M. Savaresi, and G. Rizzoni. *On battery state of charge estimation: A new mixed algorithm*. in *2008 IEEE International Conference on Control Applications*. 2008. IEEE.
163. Wang, W. and J. Mu, *State of charge estimation for lithium-ion battery in electric vehicle based on Kalman filter considering model error.* IEEE Access, 2019. **7**: p. 29223-29235.
164. Chen, X., et al., *A novel approach to reconstruct open circuit voltage for state of charge estimation of lithium ion batteries in electric vehicles.* Applied Energy, 2019. **255**: p. 113758.
165. Zhi, L., et al., *State of charge estimation for Li-ion battery based on extended Kalman filter.* Energy Procedia, 2017. **105**: p. 3515-3520.
166. Sassi, H.B., et al., *Comparative study of ANN/KF for on-board SOC estimation for vehicular applications.* Journal of Energy Storage, 2019. **25**: p. 100822.

167. Wang, T., et al., *Model-based unscented Kalman filter observer design for lithium-ion battery state of charge estimation.* International Journal of Energy Research, 2018. **42**(4): p. 1603-1614.
168. Liu, X., et al., *A Dynamic State-of-Charge Estimation Method for Electric Vehicle Lithium-Ion Batteries.* Energies, 2019. **13**(1): p. 1-16.
169. He, H., et al., *Online model-based estimation of state-of-charge and open-circuit voltage of lithium-ion batteries in electric vehicles.* Energy, 2012. **39**(1): p. 310-318.
170. Li, X., Z. Wang, and L. Zhang, *Co-estimation of capacity and state-of-charge for lithium-ion batteries in electric vehicles.* Energy, 2019. **174**: p. 33-44.
171. Shrivastava, P., et al., *Overview of model-based online state-of-charge estimation using Kalman filter family for lithium-ion batteries.* Renewable and Sustainable Energy Reviews, 2019. **113**: p. 109233.
172. Zheng, W., et al., *State of Charge Estimation for Power Lithium-Ion Battery Using a Fuzzy Logic Sliding Mode Observer.* Energies, 2019. **12**(13): p. 2491.
173. Li, I.-H., et al., *A merged fuzzy neural network and its applications in battery state-of-charge estimation.* IEEE Transactions on Energy Conversion, 2007. **22**(3): p. 697-708.
174. Chemali, E., et al., *State-of-charge estimation of Li-ion batteries using deep neural networks: A machine learning approach.* Journal of Power Sources, 2018. **400**: p. 242-255.
175. Liu, D., et al., *Hybrid state of charge estimation for lithium-ion battery under dynamic operating conditions.* International Journal of Electrical Power & Energy Systems, 2019. **110**: p. 48-61.
176. Yang, F., et al., *State-of-charge estimation of lithium-ion batteries based on gated recurrent neural network.* Energy, 2019. **175**: p. 66-75.
177. Li, C., F. Xiao, and Y. Fan, *An approach to state of charge estimation of lithium-ion batteries based on recurrent neural networks with gated recurrent unit.* Energies, 2019. **12**(9): p. 1592.
178. Xiao, B., Y. Liu, and B. Xiao, *Accurate state-of-charge estimation approach for lithium-ion batteries by gated recurrent unit with ensemble optimizer.* IEEE Access, 2019. **7**: p. 54192-54202.
179. Chemali, E., et al., *Long short-term memory networks for accurate state-of-charge estimation of Li-ion batteries.* IEEE Transactions on Industrial Electronics, 2017. **65**(8): p. 6730-6739.
180. Zhao, F., et al. *The Li-ion Battery State of Charge Prediction of Electric Vehicle Using Deep Neural Network*. in *2019 Chinese Control And Decision Conference (CCDC)*. 2019. IEEE.
181. How, D.N., et al. *State-of-Charge Estimation of Li-ion Battery in Electric Vehicles: A Deep Neural Network Approach*. in *2019 IEEE Industry Applications Society Annual Meeting*. IEEE.
182. Song, X., et al., *Combined CNN-LSTM network for state-of-charge estimation of lithium-ion batteries.* IEEE Access, 2019. **7**: p. 88894-88902.
183. Li, Y., et al., *Data-driven health estimation and lifetime prediction of lithium-ion batteries: A review.* Renewable and Sustainable Energy Reviews, 2019. **113**: p. 109254.
184. Wu, W., et al., *Low-temperature reversible capacity loss and aging mechanism in lithium-ion batteries for different discharge profiles.* International Journal of Energy Research, 2019. **43**(1): p. 243-253.
185. Bian, X., et al., *An open circuit voltage-based model for state-of-health estimation of lithium-ion batteries: Model development and validation.* Journal of Power Sources, 2020. **448**: p. 227401.
186. Li, X., et al., *State-of-health estimation for Li-ion batteries by combing the incremental capacity analysis method with grey relational analysis.* Journal of Power Sources, 2019. **410**: p. 106-114.

187. Qu, S., et al., *A Fast Online State of Health Estimation Method for Lithium-Ion Batteries Based on Incremental Capacity Analysis.* Energies, 2019. **12**(17): p. 3333.
188. Li, X., et al., *State of health estimation for Li-Ion battery using incremental capacity analysis and Gaussian process regression.* Energy, 2020. **190**: p. 116467.
189. Wang, L., et al., *State of health estimation of battery modules via differential voltage analysis with local data symmetry method.* Electrochimica Acta, 2017. **256**: p. 81-89.
190. Xiong, R., L. Li, and Q. Yu. *Improved Single Particle Model Based State of Charge and Capacity Monitoring of Lithium-Ion Batteries*. in *2019 IEEE 89th Vehicular Technology Conference (VTC2019-Spring)*. 2019. IEEE.
191. Wang, X., X. Wei, and H. Dai, *Estimation of state of health of lithium-ion batteries based on charge transfer resistance considering different temperature and state of charge.* Journal of Energy Storage, 2019. **21**: p. 618-631.
192. Lyu, Z. and R. Gao, *A model-based and data-driven joint method for state-of-health estimation of lithium-ion battery in electric vehicles.* International Journal of Energy Research, 2019. **43**(14): p. 7956-7969.
193. Shi, E., et al., *State-of-health estimation for lithium battery in electric vehicles based on improved unscented particle filter.* Journal of Renewable and Sustainable Energy, 2019. **11**(2): p. 024101.
194. Ungurean, L., et al., *Battery state of health estimation: a structured review of models, methods and commercial devices.* International Journal of Energy Research, 2017. **41**(2): p. 151-181.
195. Zhang, Y., et al., *Aging characteristics-based health diagnosis and remaining useful life prognostics for lithium-ion batteries.* ETransportation, 2019. **1**: p. 100004.
196. Feng, X., et al., *Online State-of-Health Estimation for Li-Ion Battery Using Partial Charging Segment Based on Support Vector Machine.* IEEE Transactions on Vehicular Technology, 2019. **68**(9): p. 8583-8592.
197. Venugopal, P., *State-of-Health Estimation of Li-ion Batteries in Electric Vehicle Using IndRNN under Variable Load Condition.* Energies, 2019. **12**(22): p. 4338.
198. Stroe, D.I. and E. Schaltz, *Lithium-Ion Battery State-of-Health Estimation Using the Incremental Capacity Analysis Technique.* IEEE Transactions on Industry Applications, 2019.
199. Chaoui, H. and C.C. Ibe-Ekeocha, *State of charge and state of health estimation for lithium batteries using recurrent neural networks.* IEEE Transactions on Vehicular Technology, 2017. **66**(10): p. 8773-8783.
200. Khumprom, P. and N. Yodo, *A data-driven predictive prognostic model for lithium-ion batteries based on a deep learning algorithm.* Energies, 2019. **12**(4): p. 660.
201. Esfandyari, M., et al., *A hybrid model predictive and fuzzy logic based control method for state of power estimation of series-connected Lithium-ion batteries in HEVs.* Journal of Energy Storage, 2019. **24**: p. 100758.
202. Esfandyari, M., et al., *A new approach to consider the influence of aging state on Lithium-ion battery state of power estimation for hybrid electric vehicle.* Energy, 2019. **176**: p. 505-520.
203. Feng, T., et al., *Online identification of lithium-ion battery parameters based on an improved equivalent-circuit model and its implementation on battery state-of-power prediction.* Journal of Power Sources, 2015. **281**: p. 192-203.
204. Zhang, X., et al., *A novel method for lithium-ion battery state of energy and state of power estimation based on multi-time-scale filter.* Applied energy, 2018. **216**: p. 442-451.
205. Nejad, S. and D.T. Gladwin, *Online Battery State of Power Prediction Using PRBS and Extended Kalman Filter.* IEEE Transactions on Industrial Electronics, 2019.

206. Xiang, S., et al., *Lithium-ion battery online rapid state-of-power estimation under multiple constraints.* Energies, 2018. **11**(2): p. 283.
207. Jiang, B., et al., *Online reliable peak charge/discharge power estimation of series-connected lithium-ion battery packs.* Energies, 2017. **10**(3): p. 390.
208. Cabañero, M.A., et al., *Investigation of the temperature dependence of lithium plating onset conditions in commercial Li-ion batteries.* Energy, 2019. **171**: p. 1217-1228.
209. Lu, B., et al., *Stress-limited fast charging methods with time-varying current in lithium-ion batteries.* Electrochimica Acta, 2018. **288**: p. 144-152.
210. An, F., et al., *Multi-stage constant-current charging protocol for a high-energy-density pouch cell based on a 622NCM/graphite system.* RSC advances, 2019. **9**(37): p. 21498-21506.
211. Abdel-Monem, M., et al., *Influence analysis of static and dynamic fast-charging current profiles on ageing performance of commercial lithium-ion batteries.* Energy, 2017. **120**: p. 179-191.
212. Anseán, D., et al., *Fast charging technique for high power LiFePO4 batteries: A mechanistic analysis of aging.* Journal of Power Sources, 2016. **321**: p. 201-209.
213. Yin, Y., et al., *New fast charging method of lithium-ion batteries based on a reduced order electrochemical model considering side reaction.* Journal of Power Sources, 2019. **423**: p. 367-379.
214. Zou, C., C. Manzie, and D. Nešić, *Model predictive control for lithium-ion battery optimal charging.* IEEE/ASME Transactions on Mechatronics, 2018. **23**(2): p. 947-957.
215. Pozzi, A., M. Torchio, and D.M. Raimondo. *Film growth minimization in a Li-ion cell: a Pseudo Two Dimensional model-based optimal charging approach*. in *2018 European Control Conference (ECC)*. 2018. IEEE.
216. Amanor-Boadu, J.M., A. Guiseppi-Elie, and E. Sánchez-Sinencio, *Search for optimal pulse charging parameters for Li-ion polymer batteries using Taguchi orthogonal arrays.* IEEE Transactions on Industrial Electronics, 2018. **65**(11): p. 8982-8992.
217. Lin, X., S. Wang, and Y. Kim, *A framework for charging strategy optimization using a physics-based battery model.* Journal of Applied Electrochemistry, 2019. **49**(8): p. 779-793.
218. Tomaszewska, A., et al., *Lithium-ion battery fast charging: A review.* ETransportation, 2019. **1**: p. 100011.
219. Tanim, T.R., et al., *Fast charge implications: Pack and cell analysis and comparison.* Journal of Power Sources, 2018. **381**: p. 56-65.
220. Severson, K.A., et al., *Data-driven prediction of battery cycle life before capacity degradation.* Nature Energy, 2019. **4**(5): p. 383-391.
221. Hoque, M., et al., *Battery charge equalization controller in electric vehicle applications: A review.* Renewable and Sustainable Energy Reviews, 2017. **75**: p. 1363-1385.
222. Shang, Y., et al., *Analysis and optimization of star-structured switched-capacitor equalizers for series-connected battery strings.* IEEE Transactions on Power Electronics, 2017. **33**(11): p. 9631-9646.
223. Ni, J., S. Wang, and K. Wu, *New Composite Equalization Strategy for Lithium Battery Packs.* Open Journal of Applied Sciences, 2019. **9**(04): p. 172.
224. Song, L., et al., *Lithium-ion battery pack equalization based on charging voltage curves.* International Journal of Electrical Power & Energy Systems, 2020. **115**: p. 105516.
225. Hoque, M., M. Hannan, and A. Mohamed, *Voltage equalization control algorithm for monitoring and balancing of series connected lithium-ion battery.* Journal of Renewable and Sustainable Energy, 2016. **8**(2): p. 025703.
226. Wang, S., et al., *A New Kind of Balancing Circuit with Multiple Equalization Modes for Serially Connected Battery Pack.* IEEE Transactions on Industrial Electronics, 2020.

227. Zhang, S., et al., *A GA optimization for lithium–ion battery equalization based on SOC estimation by NN and FLC.* International Journal of Electrical Power & Energy Systems, 2015. **73**: p. 318-328.
228. Zheng, J., J. Chen, and Q. Ouyang, *Variable universe fuzzy control for battery equalization.* Journal of Systems Science and Complexity, 2018. **31**(1): p. 325-342.

Appendix
Data-Driven methods

In a pack of battery a comprehensive battery management system (BMS) can appraise battery pack states accurately, e.g., state of charge (SOC), state of health (SOH), and state of power (SOP) to enhance the efficiency and safety of the battery pack. However, the non-linear behavior of batteries, caused by complex electrochemical reactions, aging effects, ambient conditions, and variable user habits make the battery state estimation a controversial challenge [133]. Despite the various state estimation methods that have been proposed in recent years [134-137], there is no holistic framework that can be implemented over a wide range of operating conditions.

In recent years, artificial intelligence (AI) has gained significant attention in a wide variety of sectors. It is the fastest-growing branch of the high-tech industry and refers to enabling machines to perform tasks intelligently. AI has tremendous potential in developing the next generation of smart battery management systems for electric vehicles (EVs). Employing the self-learning intrinsic feature of AI methodology can capture the non-linear complex dynamic of batteries; while, with training the AI-based model over a large data set, an accurate on-line battery state estimation can be accomplished.

Moreover, to decrease the charging time of EVs, several solutions have been proposed to tackle this challenge at various levels, e.g., designing novel material durable at high currents using machine learning (ML) [138] or optimizing the charging protocol to decrease the battery internal resistance and minimize the adverse effects of fast charging on cell degradation [139, 140]. The US Department of Energy (DOE) set a goal of 10 miles of driving range per minute of charge which requires fast and efficient charging [141]. However, there is no comprehensive and quantitative charging protocol developed for various batteries and applications to minimize performance attenuation. Solving such a complex problem with many parameters requires a large number of experiments that could take several

months to years. On the other hand, ML methodology can reduce the number and duration of the experiments [139]. For instance, the charging protocol has a direct effect on the batteries' lifetime. Experimenting all combinations would be cumbersome, while the ML approach can predict and optimize the charging protocol rapidly and precisely. Additionally, the charging protocol has a vital role in minimizing the capacity and power fade that generally occurs during fast charging. Although there are some studies on optimizing the charging protocol that include experimental [139, 142], physics-based [143-145], or equivalent circuit models (ECMs) [146, 147], these approaches are either limited to specific operating conditions and chemistries or may not be valid/accurate at high currents. On the other hand, with ML methodology [148] the charging protocol can be modified based on current states of the system and environmental conditions to minimize the charging time and maximize the lifetime.

It is worth noting that the inconsistency among internal parameters as well as the external environment of cells in a pack/system has detrimental effects on the pack's capacity, power capability, and lifetime [149]. Inconsistency of variables such as operating voltage, SOC, and capacity may cause deep charge/discharge of some cells, which leads to consequences such as mechanical degradation and thermal runaway. Current equalization methods to mitigate this, including passive circuits [150, 151], using resistors to remove extra energy, and active circuits [152-154] that transfer excess energy among cells, are still immature and require further investigation. The passive method is only applicable during the charging phase and it requires lengthy equalization times [155]. Although the active method is relatively reliable, it still faces issues such as low accuracy and complex implementation. However, integrating passive/active methods with ML approaches such as fuzzy logic [156] and neural network [157] can lead to invaluable insights about equalization strategies and predicting the required equalization patterns with an accurate estimation of the selected equalization variables and finding the optimal tradeoff of equalization time and energy efficiency.

Regarding the aforementioned critical challenges in this area, it is crucial to develop a holistic multi-scale framework to address BMS challenges, including accurate cell state estimation, cell equalization, and charging protocol optimization, see Figure A-1. The framework will be based on big-data analysis over different chemistries, operating conditions, and environmental conditions to ensure the adaptability of the framework using reduced-order physics-based models and ML methods.

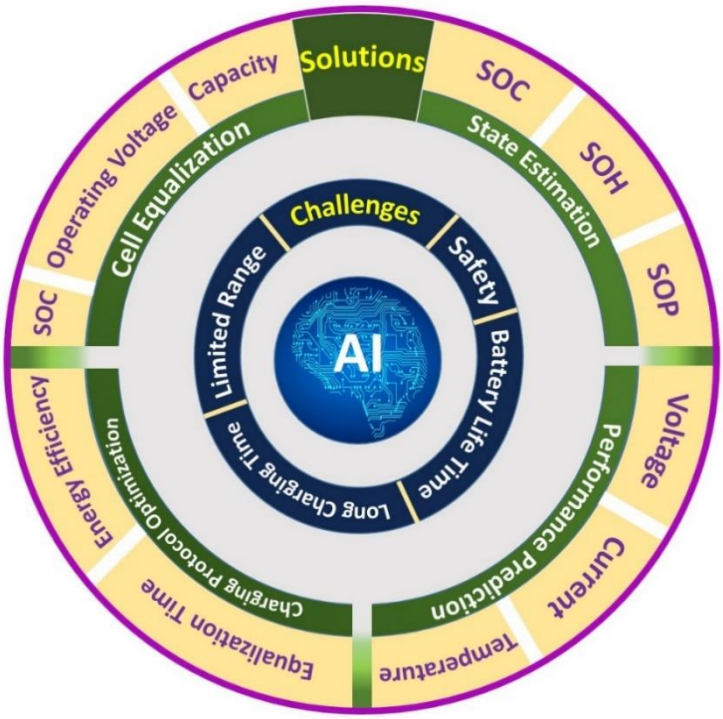

Figure A-1 Artificial intelligence perspective in electric vehicles, challenges and solutions

Battery State Estimation

State of Charge (SOC)- A ratio of the available battery charge to the maximum capacity, which is simple to define although challenging to estimate. SOC estimation has a vital role in BMS operation since it has a direct effect on measuring SOH, address the inconsistency among batteries, and optimizing the charging protocol. An accurate SOC estimation leads to a safe and reliable system operation [134]. SOC estimation methods are generally organized into four categories: 1) straightforward approach: either correlating SOC with an external parameter (e.g., open-circuit voltage [158] (OCV) or AC impedance) or coulomb counting [159] with the integration of discharge current over the time, 2) Model-based approach: using chemical and/or electrical models to simulate the complex reactions of batteries, which is known as the electrochemical model [160] [71] (EM) and equivalent circuit model [161, 162] (ECM), 3) Adaptive filter algorithm: sets of mathematical equations to predict the dynamic state of a battery by filtering uncertainties and inaccurate observations, including the Kalman filter [163] (KF), extended Kalman filter (EKF) [164, 165], unscented Kalman filter (UKF) [166, 167], particle filter [168] (PF), recursive least square [169] (RLS), or a combination of these methods[168, 170]. Generally, filter algorithms are integrated with model-based methods to obtain the battery SOC. KF is a linear prediction algorithm of the current state of measurement based on an earlier state. Therefore, KF is not suitable for battery applications due to the nonlinear nature of reactions in batteries [171], whereas EKF and UKF are more applicable to estimate the SOC because of their relatively higher accuracy in non-linear problems, 4) Data-driven approach: accurate SOC estimation by implementing self learning algorithms with battery parameters such as voltage, current, temperature, ambient temperature and humidity, and storage conditions. Data-driven approaches are mainly focused on using neural network (NN) [133], fuzzy logic (FL) [172, 173], support vector machine (SVM) [137], or a combination of these methods.

Recently, there have been some efforts to employ deep learning (DL) methods such as a deep neural network (DNN)[174], deep belief network (DBN) [175], and recursive neural network with a gated recurrent unit (RNN-GRU) [176-178] or using a long short-term memory (RNN-LSTM) [179] to enhance the accuracy of the predicted SOC. The main advantage of employing DL is its hierarchical structure with a more hidden layer compared to NN, which enhances its ability to precisely predict the battery states and consider the role of complex electrochemical reactions in battery aging [180], see Figure A-2. DNN can predict the SOC based on measured battery signals, such as the voltage, current, and temperature with mean absolute errors (MAEs) below 1% [174]. The depth of DNN (number of computational layers) has a vital role in the accuracy of the model. Generally, increasing the number of computational layers enhances the model performance, although an increase beyond a specific point causes overfitting and a larger mean squared error (MSE) [181]. As illustrated in theFigure A-2c, DBN is a deep learning algorithm suitable for modeling non-linear systems comprised of stacks of restricted Boltzmann machine (RBM) and a regression layer as the output layer [175]. RBM is a generative stochastic network that represents the dependency structure among random variables. Combining the DBN approach to simulate the non-linear behavior of batteries with EKF to filter the noise at various operating conditions can generate an accurate robust SOC estimation model with the MAE < 0.57% [175].

Two major architectures in DL are the recursive neural network (RNN) and the feedforward neural network (FNN). In the FNN design the information flow over the neurons is unidirectional; while in RNN, neurons can have a cyclic interconnection [181]. RNN is more robust in evaluating the battery's dynamic, aging, and hysteresis effects as it can use historical information, see Figure A-2. However, RNN is unable to capture long-term dependencies because of the gradient vanishing phenomenon [176]. In fact, RNN parameter update using gradient while over the time gradient becomes smaller and RNN can not effectively update its parameters. To address this issue, several modified RNNs have been

proposed to control the gradients' information propagation. Among these methods, long short-term memory (LSTM) and gated recurrent unit (GRU) can effectively capture long-term sequential dependencies [177]. GRU has a relatively simpler structure and requires less memory. In this method, there is a reset gate and an update gate to drop unwanted information and propagate useful information, respectively [176]. Therefore, GRU can address long-term dependencies, which is an essential requirement for battery modeling. On the other hand, LSTM employs a relatively complex methodology with three gates: input, output, and forgot gates. These gates control the influence of memory on the output and forgot rate [182]. RNN-LSTM can model the battery SOC with MAE less than 0.6% [179]. As presented in the

Table A- 1, the DL methods can estimate SOC more accuretly over a wide range of operating condition compared to conventional data-driven methods such as NN or FL.

	Method	Error	Temperature	Test Case
Deep Learning	DNN [174]	0.61% MAE 0.78% RMSE 2.38% MAX (25 °C)	−20 to 25 °C	Dynamic drive cycles, ±18A, Range of ambient temperatures
	DNN[181]	20.4% MAE,6.3% RMSE (25 °C)	0, 25, and 45 °C	FUDS
	DBN+KF[175]	0.57% MAE, 0.7% RMSE, 2.5% MAX,		Dynamic stress test (DST)
	RNN-LSTM[179]	0.6% MAE, 0.7% RMSE, 2.6% MAX, (25 °C)	0, 10, and 25 °C	Dynamic drive cycles, ±18A, Range of ambient temperatures
	RNN-LSTM[178]	0.66% MAE, 0.5% RMSE (30 °C)	0, 30, and 50 °C	federal urban driving schedule (FUDS)
	RNN-GRU[178]	0.49% MAE, 0.64% RMSE (30 °C)	0, 30, and 50 °C	FUDS
	RNN-GRU [177]	0.32% MAE, 2.0% MAX (25 °C)	0, 10, and 25 °C	UDDS
	RNN-GRU [176]	1.65% MAE, 2.15% RMSE (27 °C)	0,10,20,27,30, 40, and 50 °C	dynamic stress test (DST) and (FUDS)
Data-driven	NN[133]	1.17% RMSE	35, and 60 °C	Calendared aged cell, CCCV cycling.
	NN[166]	1.91% RMSE	10, 20, and 40 °C	2.6 Ah Lithium-ion battery cycling
	FL[172]	0.82% MAE 0.97% RMSE 2.45% MAX (25 °C)	0, 25, and 45 °C	FUDS and WUBSUB

Table A- 1 Data-driven methods used for SOC estimation

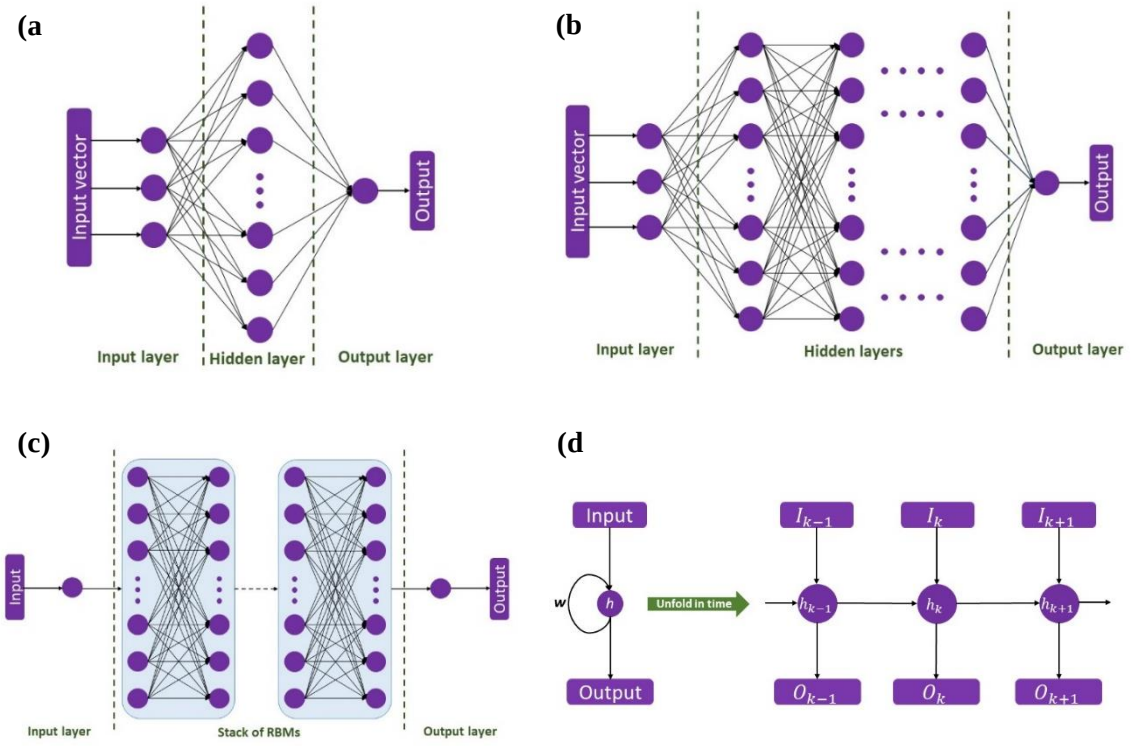

Figure A-2 Structure of a (a) Neural Network (NN) with one hidden layer, (b) Forward Neural Network (FNN) with n hidden layers, (c) Deep Belief Network (DBN) with a stack of restricted Boltzmann machine, and (d) Recursive Neural Network (RNN)

State of Health (SOH)- In addition to SOC, the state of health (SOH) of batteries is one of the critical parameters in BMS. SOH elucidates the battery energy delivery capability compared to its original condition (fresh battery). SOH is a suitable gauge to determine the end of life of a battery based on the application; for instance, EVs preferably require a SOH > 80% [133]. SOH estimation is a challenging task with no direct solution due to the large number of factors that affect battery aging, such as ambient conditions, storage temperature, and cycling specifications. Additionally, the estimation method should be scalable to the battery pack and precisely estimate the battery state at various operating conditions.

Therefore, a clear understanding of aging mechanisms is a crucial pre-requisite for developing a precise SOH estimation model. Aging mechanisms in lithium-ion batteries mainly consist of a loss of lithium-ions due to consumption in side reactions, loss of active material from mechanical degradation during cycling, and internal resistance increases due to solid electrolyte interphase (SEI) formation and losses of electrical contact in the electrode [183, 184].

SOH estimation methods are generally organized in three categories: 1) Experimental approaches: physical analysis (including destructive methods) or electrochemical analysis, such as OCV monitoring [185], incremental capacity analysis (ICA) [186-188], and differential voltage analysis (DVA) [189], 2) Model-based methods such as EM [190] and ECM [191], integrating with filter algorithms like KF [192] and PF [193] to enhance the fidelity [194], 3) Data-driven methods such as NN [133, 195], SVM [137, 196], and RNN [197]. Although physical analysis can precisely determine battery ageing mechanisms, it is not applicable for EVs since it requires a large number of experiments, is mostly destructive, and is limited to the laboratory environment. For instance, using a scanning electron microscope (SEM) or X-ray diffraction (XRD) can elucidate the aging mechanism and is beneficial for battery research and development, whereas BMS ideally requires an online and robust SOH estimation model based on the battery pack electrochemistry and ambient conditions. Among the experimental approaches, ICA has garnered much attention since it can be an *in-situ* battery health measurement tool that correlates the incremental capacity (IC) curve peaks during constant current charging to the battery age [186, 198]. However, locating IC peaks is challenging due to noises in voltage measurements. Therefore, either a filter algorithm such as a Gaussian filter [186] (GS) can be employed or voltage intervals can be chosen in an almost constant voltage region to relatively minimize the voltage measurement noise [187]. Although using the ICA method can lead to a relatively precise SOH estimation model with 1.08% MAE, it still suffers from a lack of adaptability to different battery chemistries and operating conditions. Among all the aforementioned methods, a data-driven approach

is a promising tool specifically for on-line applications such as EVs. Measuring the battery parameters, such as the voltage, current, and temperature throughout the whole battery life leads to a robust estimation model that considers the non-linear relation of parameters and the complex aging mechanisms. For instance, SVM can be trained off-line with a large volume of collected data under various aging conditions, then used to predict the SOH at various on-line environments and load conditions with RMSE < 4% [137]. Moreover, when trained over a large data set of batteries in various age conditions, NN can map battery parameters to the SOH with RMSE < 2% [133]. Although these data-driven methods can capture the non-linearity of the system, they need a large volume of data and cannot effectively predict the time-series related systems, where time-series data can capture the battery ageing process and increase the model fidelity [199]. Therefore, employing RNN can solve the mentioned limitations by considering the effect of time dependency. Additionally, to overcome the long-range dependency issue, modified RNN such as RNN-LSTM or RNN-GRU are the most suitable methods. An enhanced RNN architecture called independently RNN (IndRNN) was proposed recently where each neuron only receives its history instead of full connectivity to all other neurons. The main advantage of IndRNN compared to RNN is that IndRNN can mitigate the long-term gradient vanishing problem and has better perforamnce compared to RNN-LSTM and RNN-GRU SOH prediction models [197], see Table A- 2. As mentioned, the main challenge of employing RNN is incapability of this structure to capture long-term dependecy due to the gradient vanishing or explosion. As illustrated in the Figure A-3a, a LSTM unit has three gates including forget gate f_k , input gate i_k , and output gateo_k. The forget gate determines the effect of cell memory c_{k-1} on the current step input; the input gate limits the effect of the current step input on the cell memory, and the output gate governs the infleunce of the cell memory on the output. These gates are activated with a sigmoid function σ. Therefore, LSTM is able to carry information over the time and mitigate the RNN main deficiency. Moreover, GRU unit has a reset gate r_k, and update gate z_k, to determine the output in each step. GRU

has a relatively easier training process due to a lower number of parameters and simpler structure, see Figure A-3b.

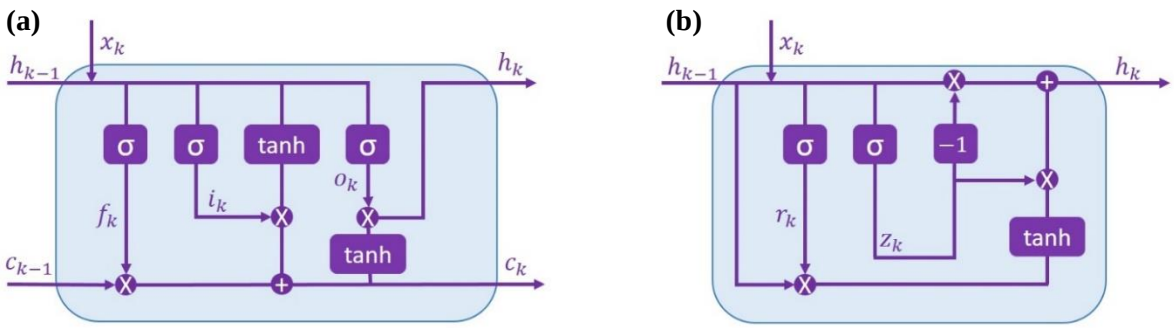

Figure A-3 Structure of a (a) LSTM unit with three gates: forget gate, f_k , input gate, i_k , and output gate, o_k , and (b) a GRU unit with two gates: reset gate, r_k and update gate, z_k.

	Method	Error	Temperature	Test Case
Deep Learning	IndRNN[197]	1.56% MAE 1.87% RMSE 3.57% MAX	25 °C	NASA's Randomized Battery Usage Dataset
	RNN-GRU[197]	2.29% MAE 2.66% RMSE 4.89% MAX	25 °C	NASA's Randomized Battery Usage Dataset
	RNN-LSTM[197]	2.67% MAE 3.13% RMSE 5.86% MAX	25 °C	NASA's Randomized Battery Usage Dataset
	DNN[200]	3.42% RMSE	25 °C	NASA Data repository CCCV cycling
Data-driven	NN[133]	1.67% RMSE	35, and 60 °C	Calendared aged cell, CCCV cycling.
	SVM[196]	3% MAX for 95% of all cases	25, and 55 °C	20 Ah and 24 Ah Lithium-ion battery cycling
	SVM+PF[137]	4% RMSE	25 °C	2.2 Ah Lithium-ion battery DST test

Table A- 2 Data-driven methods used for SOH estimation

State of Power (SOP)- state of power (SOP) represents the maximum available power of batteries, i.e., the maximum power that batteries can supply or receive over a short period with safe operation [201]. In a pack of cells connected in series, the cell with the lowest SOP limits the power capability of the pack; therefore, the inter-cell inconsistencies have a vital role in the deliverable power of the battery pack. Moreover, developing an accurate SOP estimation model is more challenging compared to SOC

and SOH. The main reason is that SOP estimation relies on the SOC and SOH of batteries, where a minor estimation error of them can exacerbate the SOP prediction inaccuracy [202]. There are quite a few studies regarding the on-line estimation of the SOP available in the literature, which are mostly based on employing ECM methods to simulate the battery dynamic [203, 204]. An algorithm such as recursive least squares (RLS) [203], particle swarm optimization (PSO) [204], or KF [205, 206] will then be employed to identify the ECM parameters; while the effect of inter-cell inconsistencies rarely considered in SOP estimation. For instance, identifying the ECM by considering the inter-cell inconsistencies in a battery pack enhances the accuracy of SOP estimation by diagnosing the weakest cell [207]. However, the main drawback of ECM-based approaches is that they cannot consider the electrochemical dynamic of the cell [135]. Therefore, incorporating a reduced-order EM can be the future trend of SOP estimation methods. Additionally, SOC and SOH estimation data-based platforms can be extended to obtain the battery SOP as well. It is worth noting that most of the available models in the literature are developed for single state estimation or joint estimation of two states; however, there is a knowledge gap in developing a comprehensive framework that can accurately estimate all battery states simultaneously, e.g., SOC, SOH, and SOP.

Charging Protocol

Battery charging patterns directly affect battery lifetime and safety. The ultimate goal is a fast and efficient charging pattern with minimum performance attenuation. The first step of charging pattern optimization is to recognize the critical parameters. For instance, low ambient temperatures decrease the charge rate and there is a higher chance of lithium plating, which leads to battery degradation [208]. Charging strategies are mainly defined as the variation of current density during the charging process and generally divided into three categories: 1) Pre-defined methods, including constant current (CC), constant current constant voltage [142] (CC-CV), multistage constant current [209, 210] (MCC), and

pulse charging [211, 212] techniques, 2) Model-based methods, including optimization based on ECM [146] and EM [213-215], and 3) Data-driven methods, using ML methodologies such as a NN or early-prediction method [139].

CC-CV is the most common charging pattern consist of a constant current charging interval up to reaching a cut-off voltage, followed by applying a constant voltage until the current reaches a preset minimum value. The main challenges of CC-CV are the relatively long charging time and low efficiency at high currents. There are some modified charging protocols that help overcome the CC-CV drawbacks. For instance, employing two or more CC stages, followed by a CV interval mainly to limit the heat generation and reduce the charging time. Moreover, the pulse charging technique is widely used to decrease the concentration polarization and decelerate the mechanical degradation [216]. In this method, the charging current is periodically interrupted by a short rest period. Overall, pre-defined methods are widely adopted due to the simplicity and ease of operation; however, they do not account for battery dynamics that lead to capacity loss and safety concerns, especially at high currents. It has been experimentally demonstrated that batteries with different chemistries under the same CC-CV charging pattern have much different cycle life and a wide range of responses at different ambient temperatures [142]. Therefore, the charging protocol should be updated based on the on-line battery states and ambient conditions to maximize the battery cycle life.

Model-based charging pattern optimization is commonly used in a closed-loop control structure to accurately adjust the current based on real-time battery parameters such as voltage, resistance, and temperature. The key performance indicators are the battery temperature, capacity retention, and charging time. Therefore, in model-based approaches either EM [217] or ECM [146] is integrated with an optimization algorithm such as genetic algorithm (GA) [148], dynamic programming [145, 217] (DP), or biography-based optimization [144] (BBO) to search for the optimal current pattern; i.e., looking for the successful tradeoff of the aforementioned indicators. For instance, employing an

electrochemical-thermal coupled model can monitor the battery internal dynamic behavior including SEI formation and lithium plating during cycling, where a DP optimization can then be employed to find the optimal charging pattern. The optimized multi-stage charging protocol can reduce the capacity fade by 4.6% after 3300 cycles [145]. The main challenge of EM is the complexity of the battery dynamic, including the electrochemical, electrical, thermal, and aging phenomena which require solving a set of coupled non-linear partial differential equations (PDEs) [218]. Thus, EM is a computationally expensive method and is not a suitable approach for on-line applications such as EVs. There are some efforts to develop reduced-order models such as ECM [148] or reduced-order physics-based models [213, 214], which are commonly adopted in BMS due to their relatively acceptable computational cost. ECMs are developed based on the electrical-thermal dynamic of batteries and have a relatively simple structure and ease of implementation; however, they have lower fidelity compared to EM because they ignore the electrochemical phenomena. Employing a reduced-order physics-based model integrated with a model predictive control (MPC) leads to an optimal charging pattern that can reduce charging time while also increasing the battery lifetime [214]. In other words, battery SOC and SOH are estimated based on reduced-order physics-based models and a MPC can find an optimum tradeoff between the charging time and SOH. Although this method is relatively suitable for on-line application, its accuracy for battery state estimation is generally less than the aforementioned data-driven methods due to simplification assumptions that cannot completely capture the non-linear battery dynamic. Moreover, most studies in the literature optimized the charging pattern for a single cell; however, pack-level aging can not necessarily be extrapolated from single-cell evaluation. IC analysis of a pack voltage response and a single cell illustrates that non-uniform temperature distribution in the pack exacerbates aging effects [219]. Therefore, further investigation of pack-level aging mechanisms is critical to optimize the charging pattern for EVs. Data-driven methods, specifically RNN, can effectively derive the optimal charging pattern while considering the dynamic states of battery and

ambient conditions, although, to the best of knowledge, there is no extensive study of battery charging pattern optimization using the DL approach.

Another aspect of employing a machine learning approach in optimal charging pattern recognition is to quantitatively predict cycle life using early cycles to significantly reduce the time necessary for experiments [220]. Integrating this early-prediction method with an optimization algorithm such as the Bayesian method can reduce the total number of experiments and also lead to the optimal charging pattern based on predefined criteria [139]. Overall, charging pattern optimization still has significant room for improvement before a general platform can be developed that is scalable to implement in practical applications.

Battery Equalization

Battery cells in a pack are not identical, since the manufacturing process, packing assembly, or environmental factors could cause minor differences in the cell aging [221]. Inter-cell inconsistencies can accelerate pack degradation and limit the total capacity; i.e., in a module of cells connected in series, the charging/discharging process should stop when the first cell reaches the cut-off voltage even while other cells are not completely charged/discharged. Therefore, employing an equalization management system is crucial in EVs. Equalization implementation usually is based on considering one or more variables, such as the SOC [156, 157], operating voltage [222-225], and capacity [152], in which the main goal is to reach consistency in these variables. Among these indicators, the operating voltage equalization is easily implemented and avoids complex variables estimation; however, the operating voltage does not accurately reflect the internal state of the batteries. In this method, cells with a higher terminal voltage in a pack are discharged while the lower-voltage cells are charged until reaching equal operating voltages [149]. Capacity-based equalization can maximize the pack capacity but is limited to static load conditions, and employing this method in EVs requires extensive complex

adjustments[152]. Therefore, the SOC-based equalization approach is the most suitable methodology for EV application because of their relatively higher equalization effectiveness. However, the outcome tremendously depends on the SOC estimation method, i.e., an accurate SOC estimation method can greatly help the equalization management system.

The equalization control method can be divided into two categories: 1) Active equalization (non-dissipative) – transferring energy from one cell to another to equalize the variables, 2) Passive equalization (dissipative) – employing resistors on each cell to reach equalized variables. The passive method has a relatively simple circuit and easier implementation; however, it causes excessive power loss and has a low equalization speed due to safety considerations [156]. Active equalization is generally based on employing a Buck-Boost circuit, using inductance to equalize adjacent cells [157]. In the literature, the mean difference algorithm is mainly used in the Buck-Boost circuit to discharge the higher energy battery and charge the lower energy battery [226]. On the other hand, by employing fuzzy logic control (FLC), the equalization current can be dynamically adjusted according to desired variables. Comparing FLC to the mean difference algorithm, it can reduce the equalization time by 49% and improve energy efficiency by 4.88% [157]. As mentioned, the main advantages of the AI-based approach are the self-learning intrinsic feature and adaptability to highly non-linear dynamics. Employing AI has been demonstrated as a successful tool to equalize the desired variables of the battery pack. In the literature, genetic algorithm (GA) [227] and FLC [156, 157, 228] have been utilized to obtain cell equalization and have demonstrated better performance compared to common equalization algorithms. Overall, the challenge of equalization is the accurate measurement of battery internal parameters and consequently the robust estimation of SOC. Therefore, employing the aforementioned SOC methods based on DL can have a great impact on the total pack capacity and equalization time. The available methods, benefits, drawbacks, and future trends of state estimation, charging protocol optimization, and inter-cell equalization are presented in the Table A- 3.

Table A- 3 methods, benefits, drawbacks, and future trend of state estimation, charging protocol optimization, and inter-cell equalization

	Method	Benefits	Drawbacks	Future Trend
State Estimation	EM	Considering electrochemical dynamic	High computational cost	RNN-based methods are able to accurately consider the complex dynamics of cells and incorporate the effect of long-term sequential dependencies which is necessary for battery state estimation
	ECM	Low computational cost, considering the electrical-thermal dynamic	Cannot incorporate the effects of electrochemical reactions	
	KF	Filtering the uncertainties to find optimal variables	Low accuracy and robustness	
	NN	Good accuracy and computational cost in non-linear dynamic modeling	Unable to capture time-series related system such as battery aging mechanisms	
	FL	Non-linear dynamic simulation with employing partial truth concept	Large computational cost	
	SVM	Employing a regression algorithm to convert the non-linear model to a linear model	Requires large data-set and potential of overfitting	
	DNN	Precise prediction of battery states with considering complex electrochemical reactions	Unable to capture time-series related system such as battery aging mechanisms	
	DBN	strong feature extraction ability and lower number of parameters compared to DNN	Overfitting potential	
	RNN-GRU	Precisely incorporate the aging effect with capture long-term sequential dependencies	Complex structure and large computational cost	
Charging Protocol	CC-CV	Easy implementation	Long charging time and low efficiency at high current rates	Optimal tradeoff between the charging time and battery cycle life can be achieved by employing a data-driven method to adjust the charging rate based on SOC and SOH
	MCC	Lower heat generation and charging time compared to CC-CV	Long charging time of CV step to prevent overcharging/discharging	
	Pulse charge	Decrease the concentration polarization and decelerate the mechanical degradation	Lack of research in optimizing pulse amplitude and width	
	EM	Adjust the current rate based on real-time battery parameters	High computational cost	
	ECM	Rapidly adjust the current rate based on real-time battery parameters	Neglecting the model complex dynamic due to employing simplified circuits	
	Data-driven	Incorporate the cell history to find optimal charging pattern on-line	Requires large data set and high computational cost	
Inter-cell Inconsistencies	Active	High energy efficiency and equalization speed	Low accuracy and complex implementation	Employing an active equalization circuit integrated with a FLC/GA to adjust the equalization current based on an accurate SOC estimation
	Passive	Relatively simple circuit and easier implementation	Excessive power loss and low equalization speed	
	Mean algorithm	Easy implementation	Lower energy efficiency and equalization speed compared to FLC and GA	
	FLC	Dynamically adjusting the equalization current based on the desired variables	Scalability difficulties due to complex FLC design based on the dynamic of batteries	
	GA	Effective optimization tool for complex non-linear problems	Relatively large computational cost	

Challenges and future direction

Despite great efforts in addressing BMS challenges, there are still several critical issues that require further investigation. Most of the state estimation research in the literature is focused on cell behavior; however, the scalability of these methods to battery module and pack is a challenging task. Although EM and ECM can provide useful insights into complex battery dynamics, they are not a promising solution for on-line state estimation in EVs. For instance, EM either is too complex, computationally expensive, and specifically developed for pre-set conditions, or cannot simulate the highly non-linear complex dynamic of batteries due to simplification assumptions in reduced-order physics-based models. Moreover, ECM has been employed to some extent for battery state estimation; however, they are developed based on the electrical-thermal response of batteries, neglecting the effects of electrochemical reactions. There have been some efforts to employ data-driven approaches in battery state estimation including SOC and SOH, which are mostly limited to specific operating conditions. Developing a robust state estimation model has an invaluable effect on addressing other BMS challenges as well. The accuracy of data-driven methods highly depends on the data-set size; therefore, training of data-driven models should be performed with a large data-set and/or by integrating with ECM and reduced-order physics-based models to accelerate the training process.

Moreover, the developed data-driven model should be able to incorporate the aging mechanisms at a wide range of operating conditions. In fact, the scalability and adaptability of the state estimation approach are crucial. To achieve this goal, off-line training is critical, but not sufficient, and on-line model enhancement can be beneficial to increase the model fidelity. It is worth noting that employing the DL approach can accelerate the universal state estimation model development due to its remarkable potential to capture the non-linearity of complex systems.

On the other hand, charging protocol optimization is an ongoing challenge in the EVs industry, which aims to find an optimal tradeoff between the charging time and battery cycle life. Since the

charging pattern can tremendously affect the battery aging, common pre-determined charging patterns such as CC-CV should not be a prominent option as they neglect the dynamic behavior of batteries, whereas on-line adjustment of the charging rate according to SOC and SOH can be highly beneficial to achieve this goal. Although there is some effort in the literature to optimize the charging pattern based on SOC and SOH measurement using a reduced-order physics-based model integrated with optimization algorithms, they are mainly restricted to single-cell consideration. It is worth noting that pack-level aging can not necessarily be extrapolated from cell evaluation. Therefore, investigating the charging pattern in the battery pack based on on-line SOC and SOH estimation integrated with optimization algorithms can be a future direction to find optimal charging patterns. The critical aspects involve employing DL methodology to enhance the state estimation robustness and find the link between cell-level and pack-level aging to successfully balance the charging time and cycle life. Special attention should be paid to the effects of low temperatures on the optimal charging pattern recognition. Another crucial aspect that should be considered in the charging pattern optimization of a battery pack is that the internal parameters and ambient conditions can cause inter-cell inconsistency. This inconsistency enhances the pack degradation and could cause over-charging/discharging of cells. Therefore, an equalization management system should be considered as well, to equalize the desired cell variables. Among the aforementioned equalization variables, the SOC is suitable since it can appropriately represent the condition of cells and be estimated rapidly and accurately on-line. From the software aspect of the equalization management system, the first step is an accurate on-line quantitative estimation of inter-cell inconsistencies which is related to the battery state estimation model. Then, an optimized algorithm considering the operating conditions should be utilized to minimize the equalization time and energy loss.

Overall, AI methodology can be a promising solution to optimize the BMS in EVs. The ultimate goal is to develop a universal framework based on employing the DL approach, specifically the RNN-

GRU method trained with a large data-set at various operating conditions. Despite the complex structure of RNN-GRU, this method can effectively capture long-term sequential dependencies, which are highly critical during the battery lifetime. The developed framework should be compatible with a wide range of ambient conditions and be able to estimate the battery states robustly. Additionally, an optimization method (e.g., GA) should be integrated to determine the optimal charging pattern and minimize the inter-cell inconsistencies. These implementations will increase the reliability and cycle life of battery packs with a reasonable charging time, allowing EVs to compete with combustion engine vehicles.

Conclusion

The applications of AI in EVs are critically reviewed in this paper with a focus on addressing key challenges for the BMS, including an accurate state estimation, optimized charging protocol, and inter-cell inconsistency equalization. Various state estimation methods are systematically evaluated, highlighting their fundamentals, benefits, and drawbacks. The significance of optimizing the charging pattern is elaborated, as common pre-defined methods have long charging times and are not able to modify the charging pattern based on the battery dynamic and environmental conditions. It is worth noting that inter-cell inconsistencies of variables such as operating voltage or SOC can exacerbate the battery pack aging, limit the total capacity, and have adverse effects on the state estimation model accuracy. This review sheds light on the prospects of employing AI to develop a universal framework to address the aforementioned challenges. In contrast, the currently available methodology is mostly limited to specific cell chemistry, pre-defined operating conditions, or cannot capture the multi-scale highly non-linear dynamic of the battery pack.

In summary, there is a knowledge gap in addressing these BMS challenges. Developing a holistic multi-scale framework to address these challenges, e.g., accurate state estimation, cell equalization, and charging protocol optimization, is highly critical for developing the next generation of EVs. The framework can be based on acquiring large data-sets over a wide range of cell chemistries, operating conditions, and environmental conditions to ensure the scalability of the framework. Integrating reduced-order physics-based models and DL methodology can lead to a comprehensive framework that accurately equalizes the cells and adjusts the charging pattern based on robust state estimation.